7-3-2012

Predicting failure behavior of polymeric and asphalt composites using damage models

Meghan Vallejo

Meghan J. Vallejo
Candidate

Civil Engineering
Department

This thesis is approved, and it is acceptable in quality and form for publication:

Approved by the Thesis Committee:

Dr. Rafiqul A. Tarefder , Chairperson

Dr. Tang-Tat Ng

Dr. Arup K. Maji

PREDICTING FAILURE BEHAVIOR OF POLYMERIC AND ASPHALT COMPOSITES USING DAMAGE MODELS

by

MEGHAN J. VALLEJO

B.S., MINERAL ENGINEERING, 2004
M.S., MINERAL ENGINEERING, 2006
NEW MEXICO INSTITITE OF MINING AND TECHNOLOGY

THESIS

Submitted in Partial Fulfillment of the
Requirements for the Degree of

Master of Science
Civil Engineering

The University of New Mexico
Albuquerque, New Mexico

May 2012

DEDICATION

For Omri

ACKNOWLEDGMENTS

I would like to thank my advisor Dr. Rafiqul Tarefder for the opportunity to perform this research at the University of New Mexico. It has been a wonderful learning opportunity and one that I am grateful for. I would also like to thank my committee members Dr. Tang-Tat Ng and Dr. Arup Maji for their comments and recommendations for this study. I would also like to the NASA EPSCoR program for funding my research on polymeric composites described in this study.

I would like to extend a special thanks to my sister, Courtney Vallejo, for her support throughout my graduate program and for her assistance with editing this manuscript and for always cheering me on. Thank you also to Daniel McDonald for his love and support over the past several years and for encouraging me in the completion of this program. And last but not least, to my mother Nancy Laura Vallejo for giving me a life-long love of learning and for always supporting me throughout my academic career.

PREDICTING FAILURE BEHAVIOR OF POLYMERIC AND ASPHALT COMPOSITES USING DAMAGE MODELS

by

Meghan J. Vallejo

B.S., Mineral Engineering, New Mexico Institute of Mining and Technology, 2004

M.S., Mineral Engineering, New Mexico Institute of Mining and Technology, 2006

M.S., Civil Engineering, University of New Mexico, 2012

ABSTRACT

This study investigates the failure behavior of two types of composite materials using damage models within the framework of ABAQUS finite element software. The failure behavior of an IM7/977-2 carbon epoxy composite material subjected to a Mode I delamination is predicted using traction-separation and bulk material damage models that are based on disturbed state concept (DSC) principles. The models were validated by comparing the results to referenced laboratory testing performed on IM7/977-2 carbon epoxy composite. The damaged states associated with various stages of loading are presented in this study.

This study also predicts the failure behavior of asphalt materials through the use of damage models using the principles of the DSC. Traction-separation crack response, damage initiation and damage evolution behavior are investigated by modeling pavement systems consisting of a hot mix asphalt (HMA) overlay above an existing HMA layer and subjected to an applied static wheel loading. Preexisting cracks located within the existing asphalt material are also considered. The extended finite element method (XFEM) was employed to model mesh-independent cracking. The finite element model was validated by comparing the results to indirect tensile laboratory testing and referenced direct tensile laboratory data-based results performed on asphalt samples. The validated model was then used to examine damage in a pavement system with and without preexisting cracks.

TABLE OF CONTENTS

LIST OF FIGURES

LIST OF TABLES

1 INTRODUCTION

A composite material is defined as a material which is made of two or more material constituents. This definition covers a broad range of materials, including fiber-reinforced materials composed of fibers within a matrix, to construction materials, such as asphalt, which is composed of aggregate within a mastic matrix.

An accurate prediction of the composite's failure behavior is required to assess the performance of the material for engineering applications. The macroscale failure of composite materials has been described through classical damage mechanics as well as fracture mechanics. Classical damage models describe the plastic deformation of the composite material by defining a damaged zone and an undamaged zone within the material. The damaged zone represents small-scale damage, such as microcracking. However, the number and size of cracks are not taken into account but are instead described by an area which is unable to support a load.

Fracture mechanics assumes that material damage is large enough to be described through a discrete fracture with a macroscale geometry that affects the behavior of the material. Failure as described by fracture mechanics requires either discrete cracks or failure zones to be defined at a specific location within the material. This limits the failure analysis of the material since the failure zones must be predefined.

The disturbed state concept (DSC) developed by Desai (2001) is a damage model which allows failure behavior to be predicted by simultaneously using both classical damage and fracture failure principles. The DSC approach accounts for the material's stress state, the deformation stress path, and the volume change the material may experience through microcracking and fracturing.

This study explores damage models within the framework of ABAQUS finite element software in order to describe damage within polymeric and asphalt composite materials. Discrete fractures within a polymeric composite material were developed without having to define damaged and undamaged zones by combining bulk (continuum) damage and delamination. This allowed for damage to occur in any part of the system. Thus, the essence of the DSC was used in this study to combine material damage models and accurately predict failure behavior.

1.1 OBJECTIVES

The objective of this study is to predict the failure behavior of polymeric and asphalt pavement composite materials using damage modeling implemented through the ABAQUS finite element software (version 6.9). This modeling approach was inspired by the disturbed state concept (Desai, 2001) and allows for both continuum (bulk) damage as well as the development of discrete fractures within the material without having to define a damaged and undamaged zone. Any part of the composite material was allowed to fail based on the current stress state in the material.

The failure behavior of a polymeric composite material was evaluated by modeling two carbon-epoxy composite panels in a double cantilever beam configuration under an applied displacement. The failure stages within the material, including damage according to the DSC and damage at the interface between the composite panels, was described to predict failure behavior of the material.

The DSC principles were used in a finite element framework to evaluate the failure and fracture behavior in an asphalt pavement by using the extended finite element method (XFEM) in ABAQUS. The XFEM method does not require damaged or undamaged zones to be defined but allows any part of the material to fail based on its stress state. In addition, the method allows the finite element model to be mesh-independent and does not require mesh refinement to predict accurate cracking behavior.

2 BACKGROUND

The disturbed state concept (DSC) as described by Desai (2001) describes material deformation behavior in terms of an undamaged, or relatively intact (RI) part and a cracked, or fully adjusted (FA) part. The RI and FA conditions are graphically shown in Figure 2.1. Under an applied load, the material is continuously transformed from the RI state to the FA state. This transformation is caused by microstructural changes within the material such as particle motion (translation, rotation, and microcracking).

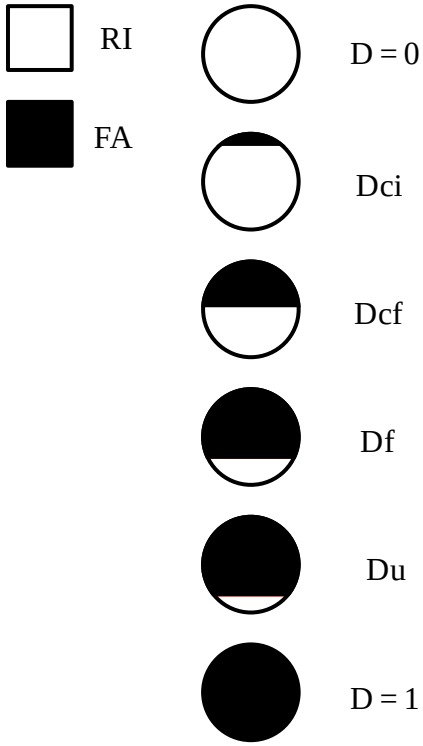

Figure 2.1. Symbolic Representation of the Disturbed State Concept (Desai, 2001)

The RI state represents undamaged material and can be described through elastic, elastoplastic, or other models (Desai, 1996). The RI part of the material is assumed to behave as a continuum. The FA state is associated with microcracking which eventually leads to complete failure. When the FA state is reached, the properties of the material are different that the material in the RI state. The FA state can be described through

continuum damage models where the material is described as a void possessing no strength; by models which allow the material to support a hydrostatic stress but not a shear stress; or through critical state models.

The disturbance function, D, is a parameter which couples the RI and FA behavior and describes microstructural changes within the material. This function allows the material behavior to be described in terms of both the RI and FA states. The disturbance function concept is illustrated in Figure 2.2, which shows the stress-strain response of a material subjected to damage-inducing stress conditions. In the figure, line *i* represents a perfectly elastic material that does not experience damage under loading. Line *a* represents the stress-strain response of a material that is initially elastic but is eventually damaged. Line c represents a completely damaged material that can sustain no stress. When D is equal to zero, the entire material is in the RI state, and no part of the material has experienced damage. As D increases, a portion of the material transforms to the FA state. This includes damage associated with the initiation of microcracking (D_{ci}), the formation of a finite crack (D_{cf}), fracture growth (D_f), and ultimate disturbance at which the material can no longer sustain a load (D_u). When D is equal to 1, the entire material has reached the FA state, and the material is considered to be completely damaged.

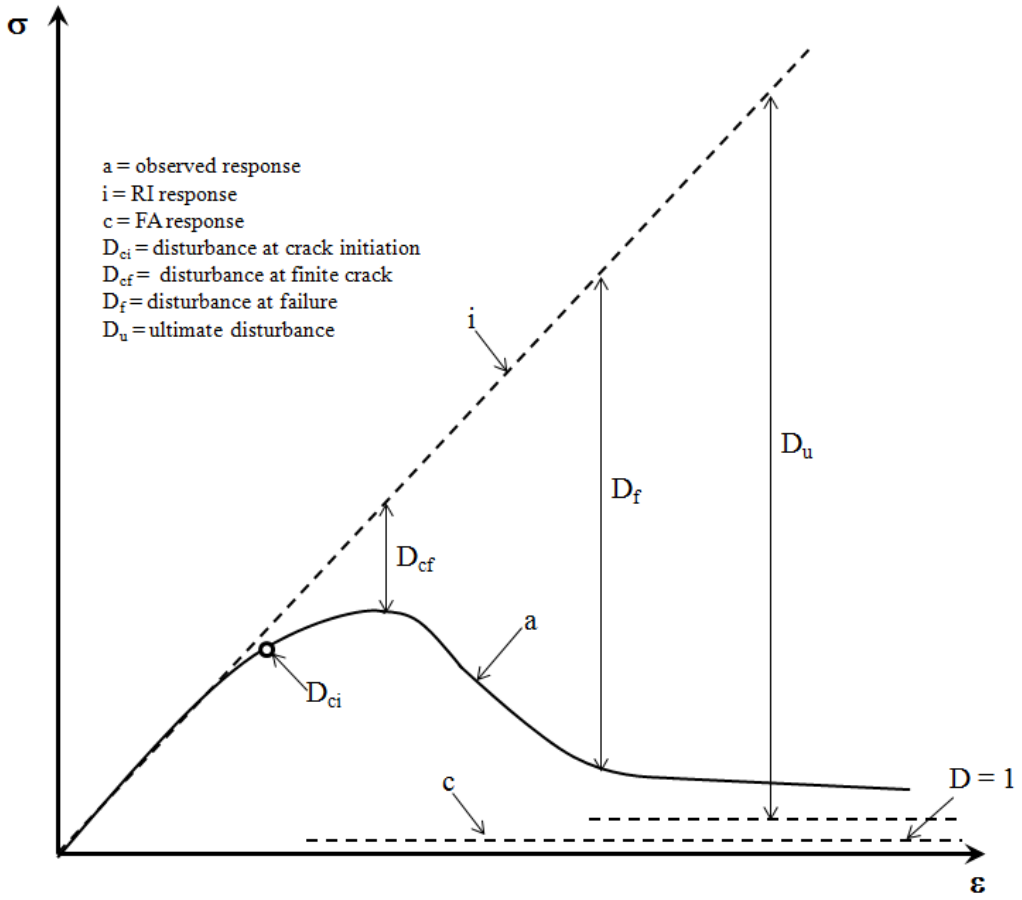

Figure 2.2. Schematic of DSC Stress-Strain Behavior (Desai, 2001)

2.1 DISTURBED STATE CONCEPT CONSTITUTIVE EQUATIONS

The DSC constitutive equations can be described as follows according to Desai (2001). If a material is composed of both relatively intact (RI) and fully adjusted (FA) parts, then the observed force acting on the material can be described through Equation 2.1:

$$F^a = F^i + F^c$$

Equation 2.1

where F^a is equal to the observed force on the material, F^c is equal to the force in the FA part, and F^i is equal to the force in the RI part. Equation 2.1 is expressed in terms of

stress by dividing the force components by the total area of the material (assuming a unit thickness) as shown in Equation 2.2:

$$\frac{F^a}{A} = \frac{F^i}{A^i} \cdot \frac{A^i}{A} + \frac{F^c}{A^c}\frac{A^c}{A}$$

Equation 2.2

where A is the total area, A^i is equal to the area of the RI part of the material, and A^c is equal to the area of the FA part of the material. This equation can then be rewritten in terms of stress:

$$\sigma^a = \sigma^i \cdot \frac{A^i}{A} + \sigma^c \frac{A^c}{A}$$

Equation 2.3

Where σ^a is the observed stress, σ^i is the stress in the RI part of the material, and σ^c is the stress in the FA part of the material. Equation 2.3 can also be written in a three-dimensional form as Equation 2.4:

$$\sigma_{ij}^a = \sigma_{ij}^i \cdot \frac{A^i}{A} + \sigma_{ij}^c \frac{A^c}{A}$$

Equation 2.4

From this point, the disturbance function D can then be introduced. Rewriting Equation 2.4 in terms of the disturbance function leads to Equation 2.5:

$$\sigma_{ij}^a = (1-D)\sigma_{ij}^i + D\sigma_{ij}^c$$

Equation 2.5

In Equation 2.5, the disturbance function D is equal to A^c/A, and $(1\text{-}D)$ is equal to A^i/A. In this equation, the disturbance function is expressed as a scalar value, which is

sufficient for practical analysis purposes and is a form which is used extensively by Desai (2001). Equation 2.5 can also be written in incremental form, as shown in Equation 2.6:

$$d\sigma_{ij}^{a} = (1-D)d\sigma_{ij}^{i} + Dd\sigma_{ij}^{c} + dD\left(\sigma_{ij}^{c} - \sigma_{ij}^{i}\right)$$

Equation 2.6

Where dD is the increment or rate of D and σ_{ij} is the stress tensor. The DSC stress equation can then be expressed in terms of constitutive tensors and strain, as follows:

$$d\sigma_{ij}^{a} = (1-D)C_{ijkl}^{i}d\varepsilon_{kl}^{i} + DC_{ijkl}^{c}d\varepsilon_{kl}^{c} + dD\left(\sigma_{ij}^{c} - \sigma_{ij}^{i}\right)$$

Equation 2.7

In Equation 2.7, C^{i}_{ijkl} is the constitutive tensor for the RI part of the material, C^{c}_{ijkl} is the constitutive tensor for the FA part of the material, and ε_{ij} is the strain tensor.

2.2 RELATIVELY INTACT STATE

The RI part of the material, which represents the part of the material which is essentially undamaged, can be described through a continuum model (elasticity, plasticity, etc.) (Desai, 2001). The RI model represents the initial conditions of the material before damage has initiated. The RI constitutive equation for an isotropic linear elastic material, which has been used in this study to describe the RI state of the material, is given by Equation 2.8:

$$\sigma_{ij}^{i} = C_{ijkl}^{i(e)}\varepsilon_{kl}^{i}$$

Equation 2.8

In this equation, σ^{i}_{ij} is the stress tensor (Equation 2.9), ε^{i}_{kl} is the strain tensor (Equation 2.10), and $C^{i(e)}_{ikjl}$ is the constitutive tensor for linear elastic isotropic material (Equation 2.11):

$$\sigma_{ij}^{i} = \begin{pmatrix} \sigma_{11} & \sigma_{12} & \sigma_{13} \\ \sigma_{21} & \sigma_{22} & \sigma_{23} \\ \sigma_{31} & \sigma_{32} & \sigma_{33} \end{pmatrix}^{i}$$

Equation 2.9

$$\varepsilon_{ij}^{i} = \begin{pmatrix} \varepsilon_{11} & \varepsilon_{12} & \varepsilon_{13} \\ \varepsilon_{21} & \varepsilon_{22} & \varepsilon_{23} \\ \varepsilon_{31} & \varepsilon_{32} & \varepsilon_{33} \end{pmatrix}^{i}$$

Equation 2.10

$$C_{ijkl}^{i(e)} = \frac{E}{(1+\nu)(1-2\nu)} \begin{bmatrix} 1-\nu & \nu & \nu & 0 & 0 & 0 \\ & 1-\nu & \nu & 0 & 0 & 0 \\ & & 1-\nu & 0 & 0 & 0 \\ & & & 1-2\nu & 0 & 0 \\ \textit{symmetrical} & & & & 1-2\nu & 0 \\ & & & & & 1-2\nu \end{bmatrix}^{i}$$

Equation 2.11

Elasto-plastic models were also used in this study. For these models, a yield stress was used to define the limit of elastic behavior of the material. The plastic strains were then expressed for each subsequent stress increment.

2.3 FULLY ADJUSTED STATE

As loading on a material increases, part of the material transforms from the RI state to the FA state. The transformation to the FA state is caused by self adjustment of the material's microstructure, which can be caused by translation and rotation of particles (Desai, 2001). Both FA and RI states exist within the material and the two states are connected in much the same way as water bubbles enclosed within a solid matrix (Desai, 2001). The overall behavior of the material is therefore dependent on both the RI and FA

parts, which can both support a load. When the final FA state is reached, the FA portion of the material is totally damaged and can support no load; this type of damage presents itself as finite cracks within the material.

One method of describing the FA state of a material is through a constrained liquid-solid in which shear strains are developed under an applied shear stress. An FA material can also be described as a constrained liquid in which the FA part of the material can carry a hydrostatic stress or mean pressure. As soon as the FA state is reached however, the material can no longer support a shear stress. The FA material can also be described as a finite crack or a finite void within the material that can support no stress.

2.4 EXPRESSIONS OF THE DISTURBANCE FUNCTION

The disturbance function D is described through the DSC concept in terms of area as shown in Equation 2.12:

$$D = \frac{A^c}{A}$$

Equation 2.12

where A is the total material area and A^c is equal to the area of the FA part of the material. The above equation is a simplified characterization of the disturbance function and applies to a material which has a unit thickness. The disturbance function can also be expressed in terms of stress as shown in Equation 2.13 (Desai, 2011):

$$D_\sigma = \frac{\sigma^i - \sigma^a}{\sigma^i - \sigma^c}$$

Equation 2.13

where σ is equal to a measure of stress (axial, shear, etc.), σ^a is equal to the observed stress response of the material, σ^i is equal to the stress in the RI portion of the material, and σ^c is equal to the stress in the FA portion of the material. Disturbance can also be expressed in terms of volume through void ratio as shown in Equation 2.14:

$$D_\sigma = \frac{e^i - e^a}{e^i - e^c}$$

Equation 2.14

where e is equal to void ratio, e^a is equal to the observed void ratio of the material, e^i is equal to the void ratio of the RI portion of the material, and σ^c is equal to the void ratio of the FA portion of the material. The disturbance function can be expressed in many other ways, including through hydrostatic or mean stress, ultrasonic velocity, and accumulated plastic strains (Desai, 2007). Stress-based disturbance within a material was investigated in this study.

2.5 DISTURBED STATE CONCEPT IN ABAQUS

Disturbed state concept principles are integrated in the ABAQUS finite element software through constitutive models which use a damage variable to describe various stress states within a material under an applied load. Material failure is defined in ABAQUS as the complete loss of load-carrying capacity that results from progressive degradation of the material stiffness (Dassault Systemes, 2009). Material failure is described through two steps: damage initiation, which is a criterion at which damage within the material begins, and through damage evolution, which is described through a decrease in the elastic modulus of the material. The evolution of damage within a material can then be described through the stress-strain curve of the material as shown in Figure 2.3.

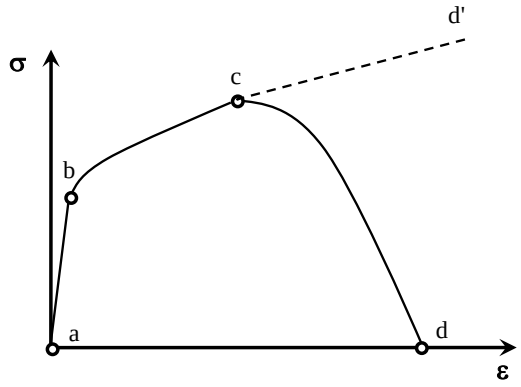

Figure 2.3. Stress-Strain Curve for a Damaged Material (Dassault Systemes, 2009)

The undamaged response of the material is shown through line *abcd'* in Figure 2.3, where line *ab* represents the linear elastic behavior of the material, and line *bc* represents plastic yielding with strain hardening. Line *cd'* represents the state of the material without damage. If the material is damaged however, a different stress-strain path is created. Point *c* defines the state of the material at which damage begins. The damage then evolves along line *cd*, which is described through a damage evolution law whereby the material stiffness degrades under the applied stress. Point *d* is the point at which the stiffness of the material has fully degraded.

The damage evolution of a material describes how the material degrades after a damage initiation criterion is met. Damage evolution can be described as total displacement for elastic materials or plastic displacement for bulk elastic-plastic materials and is referred to as displacement damage evolution. Damage evolution can also be described as the amount of energy required for a material to fail (fracture energy) after damage is initiated and is referred to as energy damage evolution. The overall damage of a material can be described through a generalized damage equation shown in Equation 2.15.

$$\sigma = (1 - D_e) \cdot \bar{\sigma}$$

Equation 2.15

where σ = stress during loading, D_e = the damage evolution variable, and $\bar{\sigma}$ is the stress within the undamaged material.

The damage variable approach is the cornerstone of Desai's disturbed state concept and captures the overall failure behavior of the material at various stress states. The difference between Desai's DSC and damage models in ABAQUS can be seen by comparing Equation 2.5 and Equation 2.15:

$$\sigma_{ij}^{a} = (1 - D)\sigma_{ij}^{i} + D\sigma_{ij}^{c} \quad \text{(DSC damage equation)}$$

$$\sigma_{ij}^{a} = (1 - D) \cdot \bar{\sigma}_{ij} \quad \text{(ABAQUS damage equation)}$$

Equation 2.16

The term $D\sigma_{ij}^{c}$ in the DSC damage equation allows the damaged portion of the material to be able to support a stress. This term is not included in the ABAQUS damage equation because a discrete fracture is created within the material when the damage variable D_e is equal to one. Once the discrete fracture is formed, the fracture cannot sustain a stress. Desai offers this scenario as one of the fully adjusted (FA) states of the DSC as described in Section 2.3, although he states that this scenario is unrealistic (Desai, 2001) because the stress-strain response of the material is no longer affected by microcracking if a finite macrocrack is formed.

The author believes that it is advantageous to model the FA state as a discrete fracture after damage evolution because discrete fracturing is a realistic failure behavior for both asphalt and polymeric composite materials. Desai (2007) has modeled the discrete fracturing scenario in asphalt. However, in Desai's study the formation of a physical fracture forming within the asphalt was not modeled. Instead, the asphalt was considered to be fractured when the damage variable was equal to unity. In the present study, fractures were physically formed within the material when the damage variable reaches a value equal to unity.

2.6 ABAQUS TRACTION SEPARATION RESPONSE

Traction-separation response is an ABAQUS model that describes damage initiation and evolution. The term traction-separation refers to the stress on the plane of a crack and the relative separation between the surfaces on either side of the crack as shown in Figure 2.4.

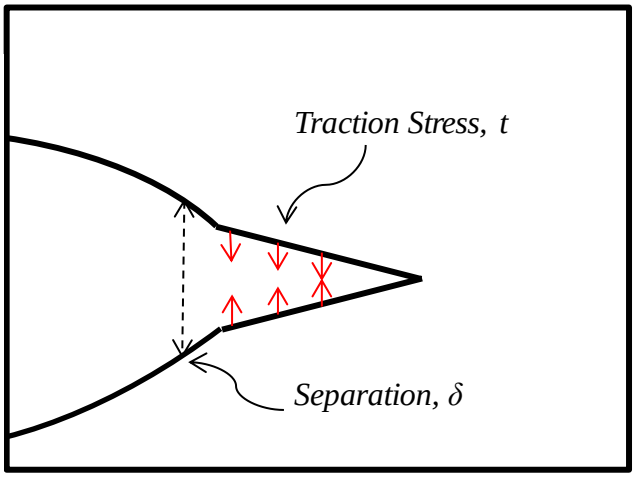

Figure 2.4. Traction-Separation of a Crack Surface

The traction-separation principal can be applied to both the interface between composite panels and to discrete cracks within an asphalt pavement. Both material interfaces and

discrete cracks affect the mechanical behavior of materials under loading and can be an initial weak zone from which further damage initiates. Traction-separation provides a way to model the progression of separation between the composite panels or to model the propagation of cracks through an asphalt material. With this modeling methodology, the interface or crack is very thin and has a geometric thickness that may be considered as zero (Dassault Systemes, 2009).

In the case of linear elastic traction-separation response, the material follows a linear elastic behavior when loaded until a critical traction stress is reached. Damage is initiated when the critical traction stress is reached. The traction stress at the crack or interface is linearly related to the traction strain. The elastic response of the material can be described as shown in Equation 2.17:

$$t = K\varepsilon = \begin{Bmatrix} t_1 \\ t_2 \\ t_3 \end{Bmatrix} = \begin{bmatrix} K_{11} & K_{12} & K_{13} \\ K_{21} & K_{22} & K_{23} \\ K_{31} & K_{32} & K_{33} \end{bmatrix} \begin{Bmatrix} \varepsilon_1 \\ \varepsilon_2 \\ \varepsilon_3 \end{Bmatrix}$$

Equation 2.17

In Equation 2.17, t is the nominal traction stress vector where t_1, t_2, and t_3 = traction stress at the crack interface during loading in the 1, 2, and 3 principal coordinate (normal, shear, and transverse) directions. The normal, shear, and transverse shear strains within the material are represented by ε_1, ε_2, and ε_3, respectively. K represents the elasticity matrix of the material and relates the traction stress vector to the strain vector. As the loading

sequence continues, damage evolves, and the capacity of the material to sustain a traction load is reduced until the material has been completely damaged.

3 PREDICTING FAILURE BEHAVIOR OF POLYMERIC COMPOSITES USING DAMAGE MODELS

3.1 INTRODUCTION

Composite materials are widely used in the space industry today. Composites are used extensively in the construction of space equipment such as spacecraft, missiles, satellites, and launch components. In particular, polymeric composites are extensively used due to the composite's light weight and performance under adverse environmental conditions. In order to determine the design life of the composite material used in such applications, an accurate prediction of the failure behavior of the material is required.

3.2 CHAPTER OBJECTIVES

The objective of this chapter was to simulate and predict the failure behavior of carbon-epoxy composite panels by allowing any part of the material to fail based on its current stress state without having to define damaged or undamaged zones. This behavior was modeled using the disturbed state concept models available in ABAQUS finite element modeling software. The failure behavior predicted through finite element modeling was validated by comparing the results to laboratory test results performed by others (Johnson et al., 2005).

3.3 MATERIAL DAMAGE AND FAILURE

The general damage behavior of the polymeric composite material was simulated by using the damage models available in ABAQUS finite element modeling software as described in Section 2.5. Material damage was specifically described through two steps:

damage initiation, which is a criterion at which damage within the material begins, and damage evolution, which was described through a decrease in the elastic modulus of the material.

3.4 DAMAGE INITIATION

Damage initiation in the bulk of the composite material occurs through the growth and joining of voids within the material. Damage initiation can also mark the starting point of the degradation of the material at the lamina interface.

3.4.1 Damage Initiation for Composite Panels

The failure behavior of the composite panels examined in this study was modeled according to the disturbed state concept (DSC), which describes the change in a material subjected to a load as it progresses to the failed state. This was primarily expressed as a decrease in the stiffness and a corresponding decrease in the load-carrying capacity of the material, which was caused by the growth and coalescence of voids within the material. This principle is similar to the definition of ductile damage as described by ABAQUS (Dassault Systemes, 2007), where the stress within the material is decreased by a disturbance factor.

The constitutive model which described damage initiation according to ductile fracturing and the DSC assumed that the equivalent plastic strain at the onset of damage, $\bar{\varepsilon}_D^{pl}$, was related to the strain rate and the stress triaxiality, which is the ratio of the mean stress to

the Mises equivalent stress. Damage was then initiated when the ductile criterion shown in Equation 3.1 was met (Dassault Systemes, 2007):

$$\omega_D = \int \frac{d\bar{\varepsilon}^{pl}}{\bar{\varepsilon}_D^{pl}\left(\eta, \bar{\varepsilon}^{pl}\right)} = 1$$

$$or: D_i = 1$$

Equation 3.1

Where ω_D = a state variable which describes plastic deformation, $\bar{\varepsilon}^{pl}$ = the plastic strain, $\bar{\varepsilon}_D^{pl}$ = the equivalent plastic strain at the onset of damage, and η = stress triaxiality = $-p/q$ = ratio of the mean stress to the Mises equivalent stress, where $p = -1/3\ \sigma_{ii}$ and $q = \sqrt{3/2\, S_{ij} S_{ij}}$. D_i is the damage initiation variable; when D_i = 1, damage within the material is initiated.

3.4.2 Damage Initiation at Interface between Composite Panels

When failure of a composite material occurred at the interface between panels through traction-separation, it was necessary to define the point at which damage initiated. The stress and strain required for failure at the lamina interface was determined through the concept of traction and separation as described in Section 2.6. With this concept, the geometric thickness of the interface was assumed to be zero, and the thickness of elements at the interface was assumed to be equal to one. This allowed for the assumption that the strains at the interface were equal to the relative separation displacements between lamina. This concept is described below (Diehl, 2008).

Nominal stress within the laminate interface was defined as the force component divided by the original area of an interface element. Nominal strain was defined as the separation between lamina at the interface divided by the original thickness of the interface. In order to model the stress-strain response of the composite panels specifically at the interface, the thickness of the interface material, h_{eff}, was assumed to be equal to one. This ensured that the strain calculated at the interface was equal to the displacement on either side of the interface. The strain at the interface was then written as shown in Equation 3.2:

$$\varepsilon = \frac{\delta}{h_{eff}}$$

Equation 3.2

where ε = strain at the interface of the composite, δ = displacement between the laminates on either side of the interface, and h_{eff} = initial thickness of the interface material. The strain can also be expressed through the three components of composite strain: ε_1, ε_2, and ε_3 with corresponding directional displacements δ_1, δ_2, and δ_3. Using this concept, the traction-separation response was described as shown in Figure 3.1:

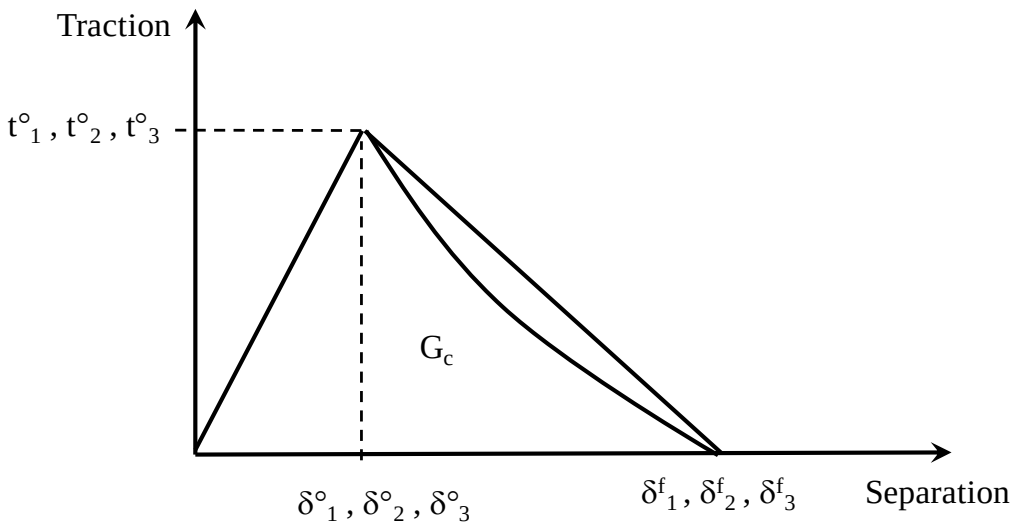

Figure 3.1. Traction-Separation Response of a Composite Material

In Figure 3.1, $t°$ represents the peak traction stress within the composite and the point at which damage was initiated. This peak traction stress was specified for the local 1, 2, or 3 directions of the composite material ($t°_1$, $t°_2$, *or* $t°_3$). The symbol $\delta°$ represents the displacement associated with the peak traction stress in the local 1, 2, or 3 directions of the composite ($\delta°_1$, $\delta°_2$, and $\delta°_3$). Because the initial interface material thickness, h_{eff}, was equal to unity, the displacements represented the strain at the interface in the respective principal material coordinate directions. As the material was loaded, there was a stress increase and a corresponding increase in displacement between the laminates at the interface boundary until a critical value (δ^f) was reached and the material was considered to be completely failed.

3.4.3 Maximum Nominal Stress Damage Initiation at Interfaces

Damage initiation at the composite panel interface was described through the use of maximum traction stress criterion to define the stress at which damage begins. In this

damage initiation method, damage will initiate when the nominal traction stress ratio reaches a value of 1 as shown in Equation 3.3 (Dassault Systemes, 2007):

$$\max\left\{\frac{\langle t_1 \rangle}{t_1^\circ}, \frac{t_2}{t_2^\circ}, \frac{t_3}{t_3^\circ}\right\} = 1$$

$$or: \ D_i = 1$$

Equation 3.3

where t_1, t_2, and t_3 = traction stress at the composite interface during loading in the 1, 2, and 3 principal coordinate directions; and $t°$ = peak stress at which damage will initiate. The Macaulay brackets ⟨ ⟩ in Equation 3.3 signify that a purely compressional deformation in the fiber direction of the composite will not initiate damage. D_i is the damage initiation variable; when $D_i = 1$, damage within the material will initiate.

The initiation of damage was specifically described through a quadratic combination of the traction stresses in the principal material directions as shown in Equation 3.4 (Dassault Systemes, 2007):

$$\left\{\frac{\langle t_1 \rangle}{t_1^\circ}\right\}^2 + \left\{\frac{t_2}{t_2^\circ}\right\}^2 + \left\{\frac{t_3}{t_3^\circ}\right\}^2 = 1$$

$$or: \ D_i = 1$$

Equation 3.4

3.4.4 Maximum Nominal Strain Damage Initiation at Interfaces

Damage initiation may also be modeled through a maximum nominal strain criterion by specifying a strain value at which damage will initiate. A normal, shear, or transverse

shear maximum strain value can be utilized as initiation criteria, and damage will initiate when the nominal traction strain value reaches unity, as shown in Equation 3.5 (Dassault Systemes, 2007):

$$\max\left\{\frac{\langle\varepsilon_1\rangle}{\varepsilon_1^\circ}, \frac{\varepsilon_2}{\varepsilon_2^\circ}, \frac{\varepsilon_3}{\varepsilon_3^\circ}\right\} = 1$$

$$or: \ D_i = 1$$

Equation 3.5

where ε_1, ε_2, and ε_3 = strain at the composite interface during loading in the 1, 2, and 3 principal coordinate directions; and ε° = peak strain value at which damage will initiate.

The initiation of damage can also be described through a quadratic combination of the strains in the principal material directions as shown in Equation 3.6 (Dassault Systemes, 2007):

$$\left\{\frac{\langle\varepsilon_1\rangle}{\varepsilon_1^\circ}\right\}^2 + \left\{\frac{\varepsilon_2}{\varepsilon_2^\circ}\right\}^2 + \left\{\frac{\varepsilon_3}{\varepsilon_3^\circ}\right\}^2 = 1$$

$$or: \ D_i = 1$$

Equation 3.6

3.5 DAMAGE EVOLUTION

After damage in a composite material has initiated, a damage evolution path was specified to describe how damage proceeded and the point where ultimate failure was reached.

3.5.1 Damage Evolution for Composite Panels

Damage evolution according to the DSC is similar to ductile damage, where damage is described through yield stress softening and elasticity degradation of the material (Dassault Systemes, 2007). Damage evolution is shown in Figure 3.2.

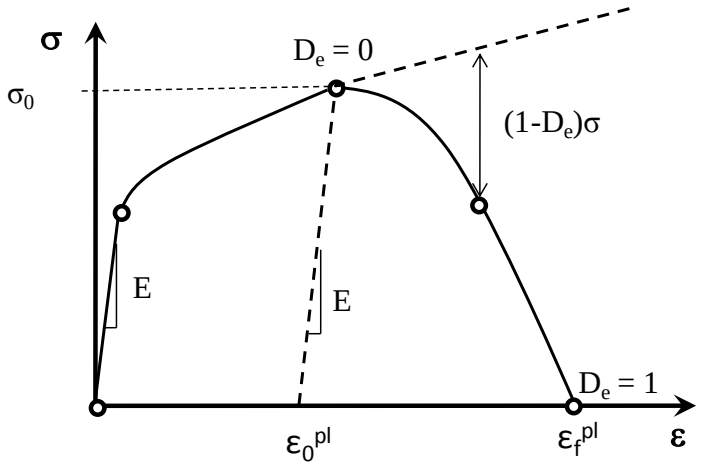

Figure 3.2. Parameters for the Stress-Strain Curve of a Damaged Material

In this figure, E = elastic modulus of the material, D_e = damage evolution variable, σ_0 = yield stress at the onset of damage, ε_0^{pl} = equivalent plastic strain at the onset of damage, and ε_f^{pl} = equivalent plastic strain at failure. In Figure 3.2, the solid portion of the curve represents the damaged material stress-strain response, while the dashed line represents the undamaged material response. The damage evolution variable D_e describes the effect of the damage mechanisms acting on the material. Damage evolution is complete when D_e reaches a value of 1 and the material can no longer sustain any stress.

Because finite element methods were used to model damage evolution, the equivalent plastic strain at failure, ε_f^{pl}, was a function of the finite element length and thus could not

be used as a material parameter to describe damage evolution. Damage evolution was then described through fracture energy dissipation, G_f, which is defined as the energy required to open a unit area of crack within the composite panel (Dassault Systemes, 2007). The response of the material after damage initiated was described through a stress-displacement response which was determined from a stress-strain response as shown in Equation 3.7:

$$G_f = \int_{\bar{\varepsilon}_o^{pl}}^{\bar{\varepsilon}_f^{pl}} L * \sigma_y * d\bar{\varepsilon}^{pl} = \int_0^{\bar{u}_f^{pl}} \sigma_y * d\bar{u}^{pl}$$

Equation 3.7

Where G_f = fracture energy dissipation, $\bar{\varepsilon}_0^{pl}$ = equivalent plastic strain at the onset of damage, and $\bar{\varepsilon}_f^{pl}$ = equivalent plastic strain at failure, L = characteristic length of the finite element, σ_y = yield stress, $d\bar{\varepsilon}^{pl}$ = the plastic strain rate, $\bar{u}^{pl}$ = equivalent plastic displacement, and $\bar{u}_f^{pl}$ = equivalent plastic displacement at failure. The characteristic length L in Equation 3.7 was based on the geometry of the finite element. For solid elements, L is the cube root of the integration point for volume; for shells and planar elements, L is the square root of the integration point area.

3.5.2 Damage Evolution at Interface between Composite Panels

Damage evolution for traction-separation behavior was more specifically described through the traction stresses and the separations experienced at the laminate interface as shown in Figure 3.1. In Figure 3.1, $t°$ represents the peak traction stress in the local 1, 2, or 3 directions within the composite and the critical value at which damage is initiated. Beyond this value, the traction stress and separation (displacement) increases until a

failed separation value, δ^f, is reached. This traction separation path, or damage evolution curve can be described as linear or exponential. The damage variable describes the damage evolution of the material and reduces the amount of traction stress that the material can bear as described in Equation 3.8:

$$t_1 = (1 - D_e)\,\bar{t}_1$$

$$t_2 = (1 - D_e)\,\bar{t}_2$$

$$t_3 = (1 - D_e)\,\bar{t}_3$$

Equation 3.8

Where t_1, t_2, and t_3 = current traction stress within a composite during loading in the 1, 2, and 3 principal coordinate directions, $\bar{t}_1$, $\bar{t}_2$, and $\bar{t}_3$ are the traction stresses predicted by the linear elastic traction-separation behavior without damage, and D_e is the damage evolution variable.

The failed separation value, δ^f, defines the point at which damage evolution is complete and the damage evolution variable, D_e, as described by Desai (2001) is equal to one. The point at which damage evolution is complete is specified by the fracture energy, G_C, which is the energy required to open a unit area of crack within the interlaminar material and is equivalent to the area under the traction separation curve shown in Figure 3.1. If the area under the curve, G_C, is specified and the traction stress at damage initiation is known, then the point at which damage evolution is complete (D_e = 1) is known.

The damage evolution variable is related to the fracture energy through Equation 3.9 (Dassault Systemes, 2007):

$$D_e = \frac{\delta_m^f \left(\delta^f - \delta^o\right)}{\delta^f \left(\delta_m^f - \delta^o\right)}$$

Equation 3.9

Were D_e = damage evolution variable, $\delta°$ = displacement associated with the peak traction stress, δ^f = maximum displacement attained during the loading of the interlaminar material, and $\delta_m^f = 2*G_C/t°$, where G_C = fracture energy and $t°$ = the peak traction at which damage was initiated.

3.6 METHODOLOGY

Traction-separation response and damage initiation and evolution were studied in a composite material composed of IM7 carbon graphite fibers in a 977-2 epoxy matrix. The IM7/977-2 composite was modeled in ABAQUS finite element software using two laminate panels subjected to double cantilever beam loading. Finite element input parameters were based on an inter-laminar toughness study of an IM7/977-2 composite beam by Johnson et al. (2005). In the study by Johnson, the Mode I interlaminar fracture toughness ("peeling" toughness) of an 8-ply, $[0_3/\pm3/0_3]$ layup composite panel and 16-ply, $[0_7/\pm3/0_7]$ composite panel subjected to double cantilever beam loading were determined through laboratory testing at various temperatures (Johnson et al. 2005). The experimental temperatures ranged from -196°C (-320°F) to 160°C (-20°F). The laboratory tests performed by Johnson et al. (2005) were conducted according to ASTM D 5528-01, "Standard Test Method for Mode I Interlaminar Fracture Toughness of

Unidirectional Fiber-Reinforced Polymer Matrix Composites". The finite element modeling input parameters used in this study were based on the laboratory test results of the 8-ply panel at room temperature from the Johnson et al. (2005) study.

As specified in the Johnson study, each panel was 150 mm long, 26 mm wide and was 4 plies thick. Each ply was 0.150 mm thick for a total panel thickness of 0.6 mm. The composite geometry is shown in Figure 3.3.

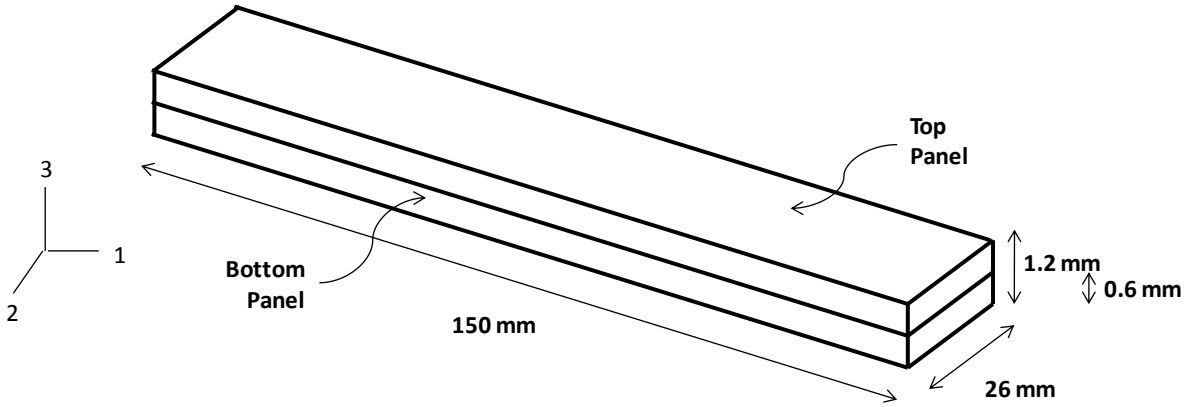

Figure 3.3. Geometry of Composite for Finite Element Analysis

The composite panels were manufactured with a Teflon strip inserted between the ±3 layers in the delamination laboratory experiment. The Teflon strip provided an initial delamination within the composite where equipment was used to peel the panels apart. This delamination was reproduced in the present finite element study in order to directly compare the laboratory test results with finite element analysis results. A 38 mm wide delamination was used in the ABAQUS composite model as shown in Figure 3.4. A total displacement of 110 mm was applied in the 3-principal direction of the composite layup. In order to simulate a double cantilever beam, the left edge of the composite was

constrained from translation in the 1, 2, and 3 principal directions. The delamination and boundary conditions of the composite beam are shown in Figure 3.4.

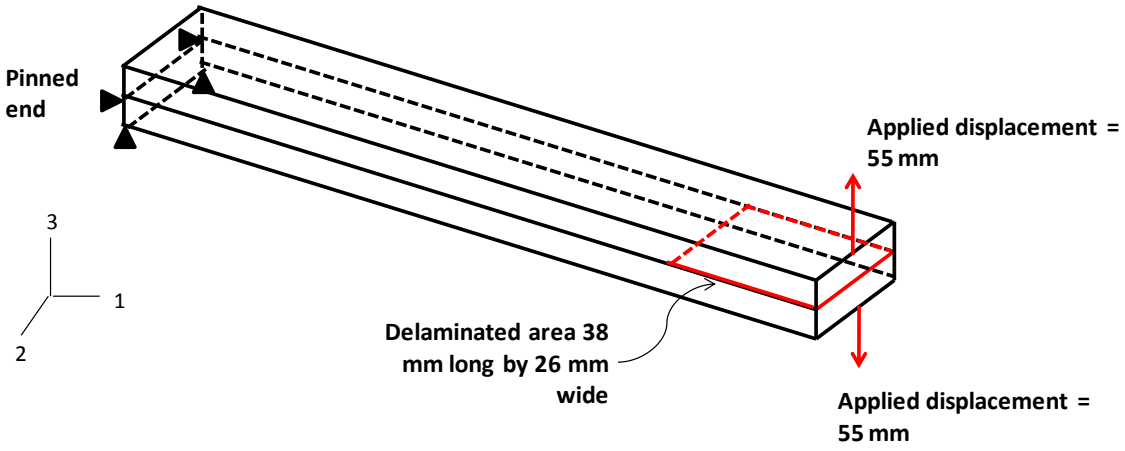

Figure 3.4. Boundary and Loading Conditions for Finite Element Analysis

3.7 MATERIAL PROPERTIES

Two sets of material properties were used in the finite element analysis performed in this study. The first set consisted of the composite panel material properties; the second set consisted of the interface material properties. These properties are described in detail in the following sections.

3.7.1 Composite Panels: Elastic Material Properties

The properties of the IM7 carbon fibers and the 977-2 epoxy matrix used in the finite element analysis were obtained from the Hexcel® IM7 data sheet and the Cycom® 977-2 data sheet, respectively (Cycom, 2010 and Hexcel, 2010). The properties of the composite panels as a whole were determined using micromechanics principles with an

assumed fiber-volume fraction of 60%. The elastic properties of the IM7/977-2 composite panels are summarized in Table 3.1.

Table 3.1. Material Properties of IM7/977-2 Composite Beam

Fiber Volume Fraction	60%
Tensile Modulus, E_1	167 GPa
Transverse Modulus, E_2	7.39 GPa
Transverse Modulus, E_3	7.39 GPa
Poisson's Ratio, v_{12}	0.34
Poisson's Ratio, v_{13}	0.34
Shear Modulus, G_{12}	2.96 GPa
Shear Modulus, G_{13}	2.96 GPa

3.7.2 Composite Panels: Plastic Material Properties

The plastic behavior of the composite panels was based on a study by Parry and Al-Hazmi (2003). In this study, cylinders of composite material composed of IM7 carbon fibers and 977-2 epoxy matrix were loaded dynamically in compression at a high strain rate of 850 s^{-1}. A stress-strain curve showing the elastic and plastic behavior of the composite material was developed with the test data and is shown in Table 3.2:

Table 3.2. Compressive Stress-Strain Properties of IM7/977-2 Composite Beam

Stress, MPa	Total Strain, %	Elastic Strain, %	Plastic Strain, %
0	0	0	0
857	1.01	1.01	0
904	1.135	1.006	0.129
943	1.265	1.059	0.206
991	1.419	1.032	0.387

3.7.3 Composite Panels: Damage Initiation and Evolution

The initiation and evolution of damage in the composite panels was modeled using the DSC/ductile criterion shown in Equation 3.1. The DSC/ductile damage was described through a decrease in stress triaxiality and fracture strain. The strain at which fracture was initiated was determined from the study by Parry and Al-Hazmi (2003). The strain rate of $850s^{-1}$ obtained from the same study was used in the ductile damage initiation parameters. The damage initiation parameters for the composite panels are summarized in Table 3.3.

Table 3.3. Damage Initiation Parameters for Composite Panels

Stress Triaxiality, η	Damage Initiation Strain	Strain Rate, s^{-1}
0	0.01451	850
0.1	0.008	850
0.2	0.004	850
0.3	0.002	850
0.4	0.001	850
0.5	0.0008	850

Once damage within the composite panels was initiated, damage evolution was described through the fracture energy required to open a unit area of crack within a composite panel, G_f. The damage evolution portion of the composite panels' stress-strain curve was assumed to be linear. A critical fracture energy of 0.478 mJ/mm^2 was used in the analysis based on the fracture energy provided in the Cycom® 977-2 Toughened Epoxy Resin data sheet (Cycom, 2010).

3.7.4 Interlaminar Material

The undamaged interlaminar material properties were based on the critical fracture energy of the composite material as described by Diehl (2008). A Mode I "peeling" critical fracture energy of 0.2973 mJ/mm^2 was used based on the findings by Johnson et. al. (2005) for an 8-ply double cantilever beam tested at room temperature. The interface strength of the composite was then determined using the critical fracture energy as shown in Equation 3.10:

$$t^{\circ} = \frac{2G_C}{\delta^f}$$

Equation 3.10

where $t°$ = interface strength of the composite material in a given principal direction, G_c = interlaminar critical fracture energy, and δ^f = cohesive ductility value as described by Diehl (2008). According to Diehl, the cohesive ductility value, δ^f, is a function of the cohesive finite element length, L_c, and a fraction, f, of the cohesive element size. A cohesive element length of 0.2 mm and a fraction of the cohesive element size of 0.5 were used in this analysis. The cohesive ductility value, δ^f, was calculated using Equation 3.11:

$$\delta^f = fL_C$$

Equation 3.11

where δ^f = cohesive ductility value, L_c = cohesive element size, and f = fraction of the cohesive element size.

The initial elastic behavior of the interface was expressed as a material stiffness per unit area as described by Diehl (2008) for a material which obeys a traction-separation constitutive model. The initial elastic behavior was calculated as shown in Equation 3.12:

$$K_{eff} = \frac{2G_C}{\delta_{ratio}\left(\delta^f\right)^2}$$

Equation 3.12

where K_{eff} = initial material stiffness per unit area, G_c = interlaminar critical fracture energy, δ^f = cohesive ductility value, and δ_{ratio} = damage initiation ratio = $\delta°/\delta^f$. The value $\delta°$ is the separation distance at which damage is initiated. Diehl (2008) recommended a damage initiation ratio of 0.5 for finite element analysis. The effective elastic modulus of the interlaminar, cohesive material was calculated using Equation 3.13:

$$E_{eff} = K_{eff} * h_{eff}$$

Equation 3.13

where E_{ff} is the effective elastic modulus of the cohesive interlaminar material, K_{eff} is the initial material stiffness per unit area, and h_{eff} is the initial thickness of the cohesive

element as described by Diehl (2008). An initial effective thickness value, h_{eff}, of one was specified in the ABAQUS finite element model used in this study. The full interlaminar properties used in this analysis are summarized in Table 3.4.

Table 3.4. Composite Inter-laminar Material Properties

Interlaminar critical fracture energy, G_c	0.2973 mJ/mm^2
Cohesive element size, L_c	0.2 mm
Fraction of the cohesive element size, f	0.5
Cohesive ductility value, δ^f	0.1
Damage initiation ratio, δ_{ratio}	0.5
Interface strength, $t^\circ = t_1^\circ, t_2^\circ, t_3^\circ$:	5.95 MPa
Interface stiffness, K_{eff}	118.9 MPa
Effective elastic modulus, E_{eff}	118.9 MPa

3.8 ELEMENT TYPE AND TIME STEP

Quadrilateral continuum shell elements were used to model the IM7/977-2 composite panels in the ABAQUS finite element modeling software. The interface of the composite was modeled using eight-noded, three dimensional cohesive elements. A single time step (time period equal to one) was used in the analysis with the time step increments (fractions of a step) shown in Table 3.5. The step time incrementation was also adjusted to account for non-linear effects ("Nlgeom" setting on). An automatic stabilization damping factor of 1 x 10^{-5} was also used. The time incrementation was adjusted for a discontinuous analysis (I_0 = 8, I_R = 10). A maximum number of iterations (I_A) value of 15 was used in this analysis.

Table 3.5. Time Step Increments Used in ABAQUS Finite Element Model

Maximum Number of Increments	2500
Initial Increment Size	1×10^{-4}
Minimum Increment Size	1×10^{-15}
Maximum Increment Size	0.1

3.9 RESULTS AND DISCUSSION

The results obtained from the finite element analysis performed on a double cantilever IM7/977-2 beam using the ABAQUS software are presented in the following figures. A contour plot of the displacement in the 3-principal direction during delamination is shown in Figure 3.5, while a contour plot of the stress (σ_{33}) within the composite is shown in Figure 3.6. The displacements in the following figures have been exaggerated for ease of visibility.

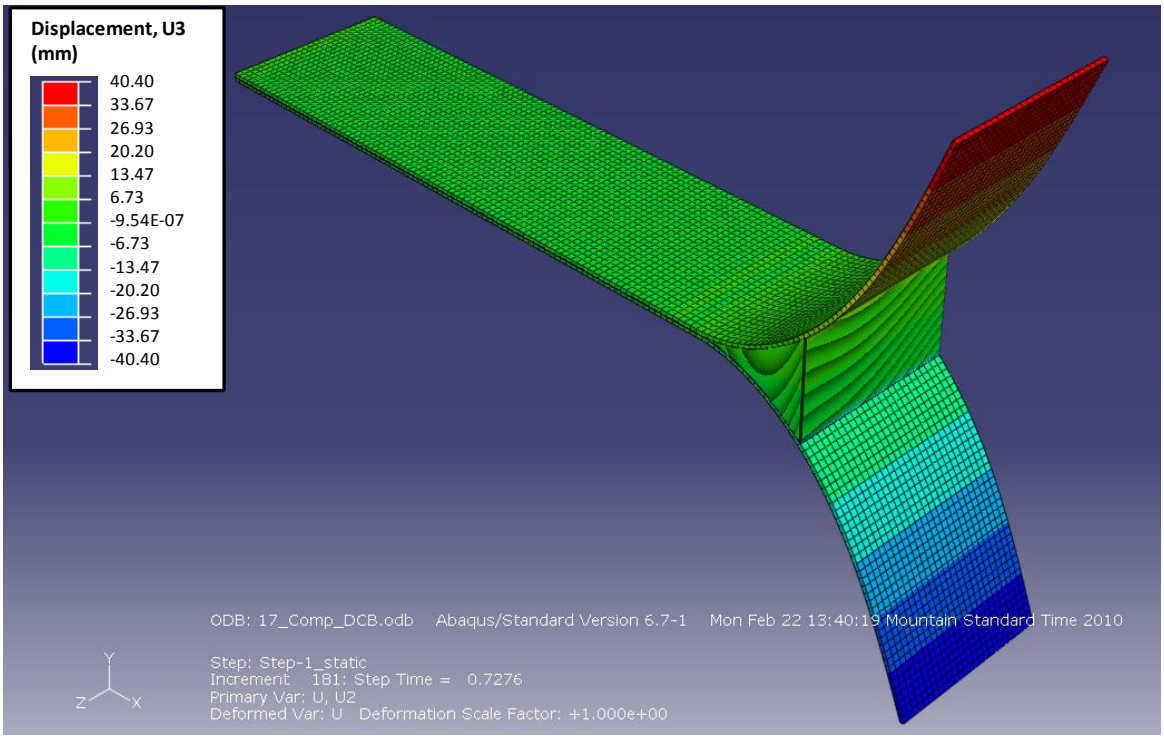

Figure 3.5. Contour Plot of Displacement of a Composite Double Cantilever Beam

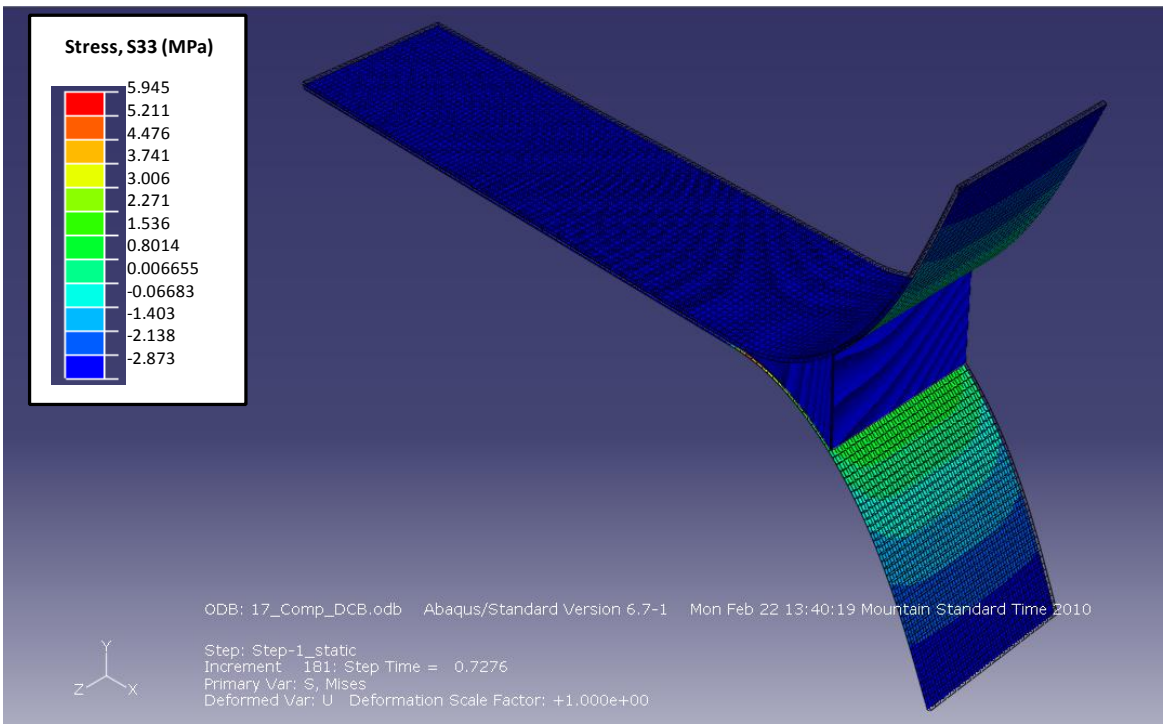

Figure 3.6. Contour Plot of Stress (σ_{33}) in a Composite Double Cantilever Beam

In order to compare the results from this study to the laboratory experiments performed by Johnson et. al (2005), a force versus displacement curve at a specific reference point was generated for the composite assembly. The reference point used in the finite element analysis is at the same location where results were measured in the Johnson study and is located where the 55 mm displacement was applied to the top composite panel. The reference point is shown in Figure 3.7. The results of the normal force versus displacement are shown in Figure 3.8.

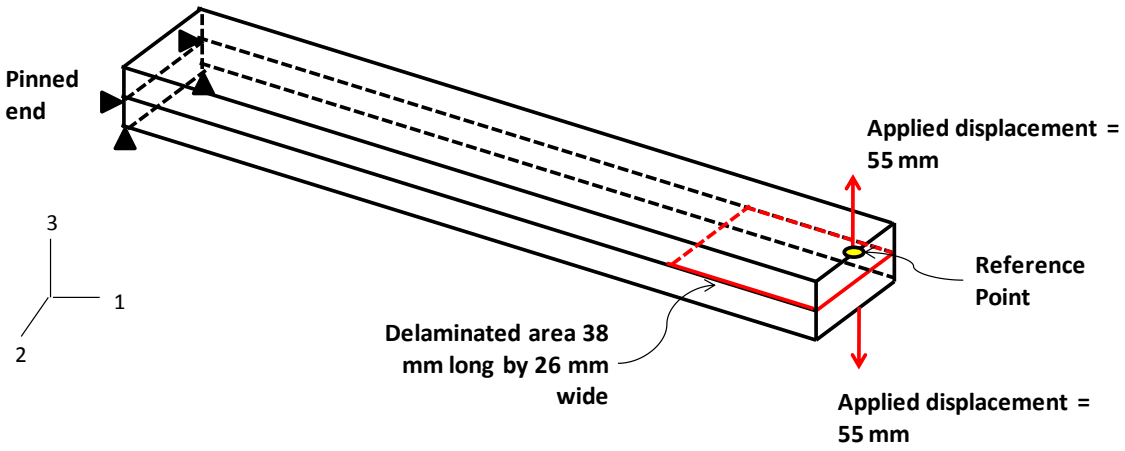

Figure 3.7. Reference Point for Force and Displacement Shown in Figure 3.8

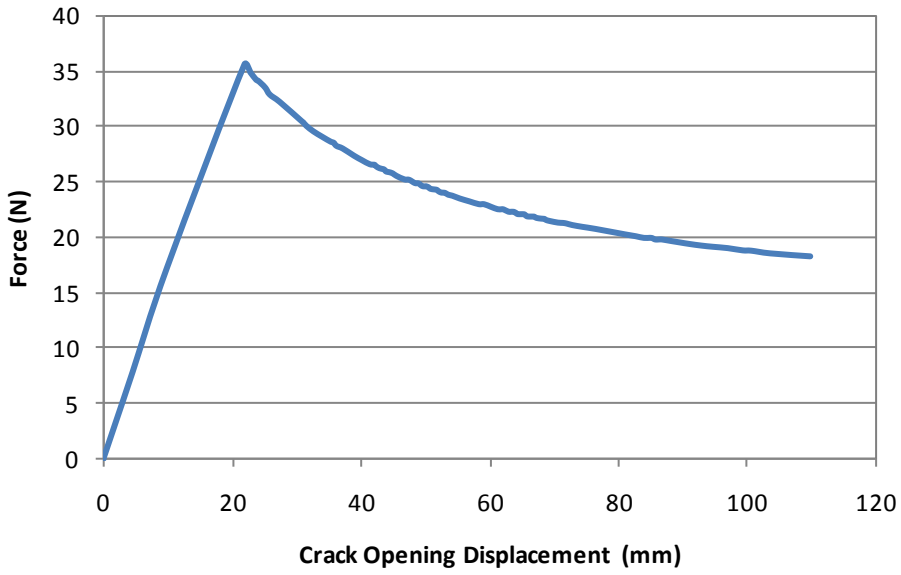

Figure 3.8. Force vs. Displacement Curve for Reference Point on IM7/977-2 Beam

The normal force increased linearly with displacement until a maximum force of 35.5 N was reached at the reference point and the quadratic combination of traction stresses within the interface material reached a value of one as described in Equation 3.4. Damage was initiated in the interface material after the maximum force was achieved,

which also marked the starting point at which damage evolution began and the force decreased as displacement increased.

A contour of the damage initiation criteria described in Equation 3.4 is shown in Figure 3.9. The red contours indicate that the damage initiation criteria reached a value of unity, which indicates that the element reached the maximum traction stress value.

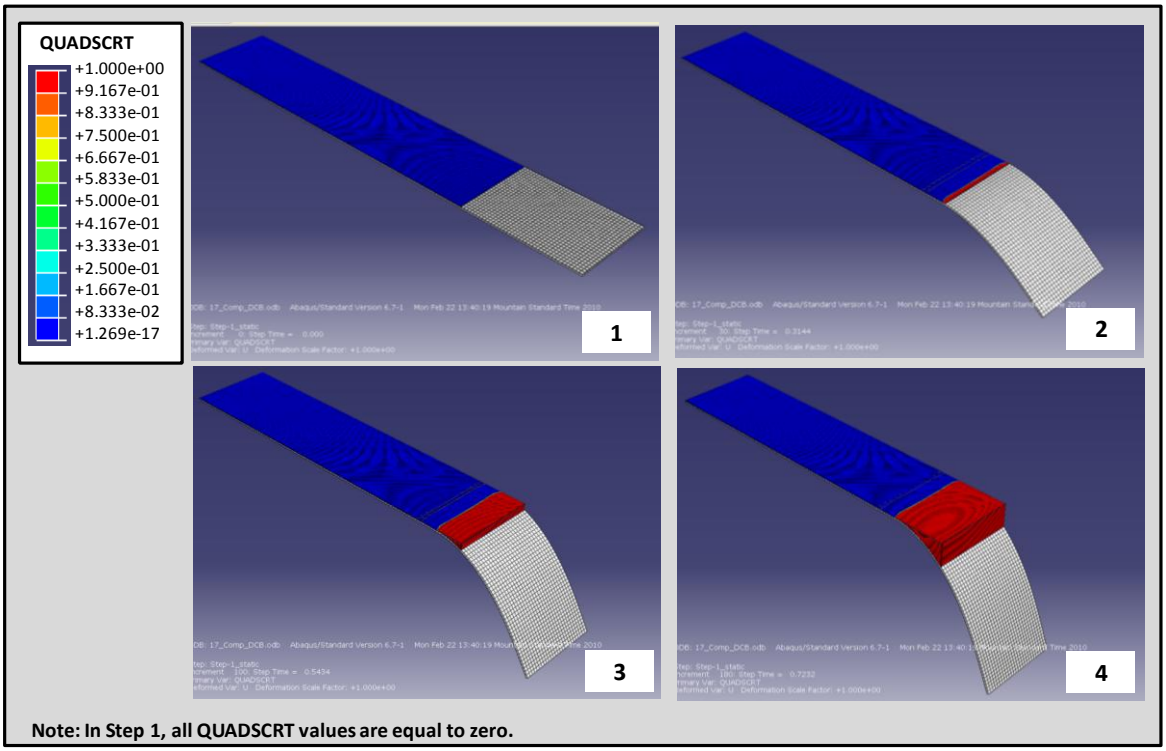

Figure 3.9. Damage Initiation Variable Contour Plots for Various Time-Steps in the Loading Sequence of the Double Cantilever Beam

A plot of the damage initiation variable D_i versus force applied to the beam ends for a specific reference element was created in order to determine the maximum allowable force before damage initiation. The reference location is an inter-laminar cohesive element and is presented in Figure 3.10. The damage initiation variable plots for the four nodes of the reference element are shown in Figure 3.11. Damage was initiated in

interfacial elements when the applied force at the reference element reached a value of 17.2 N which caused the quadratic combination of traction stresses as described in Equation 3.4 to reach a value of one (D_i =1) . The damage evolution variable D_e versus the force applied to the beam ends is shown in Figure 3.12.

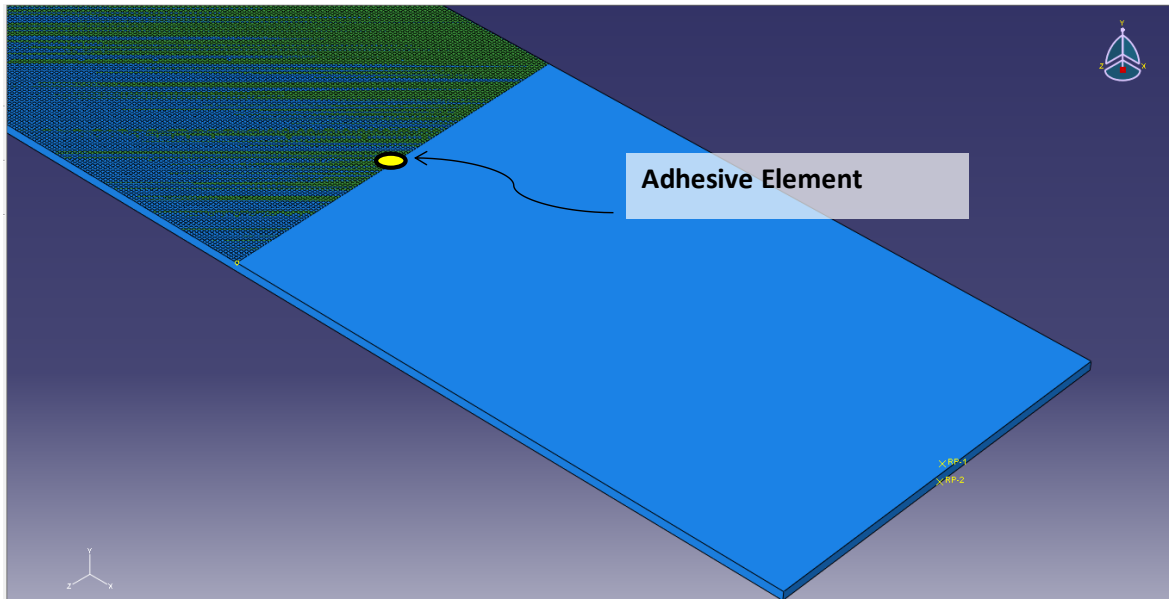

Figure 3.10. Reference Element for Results Shown in Figure 3.11

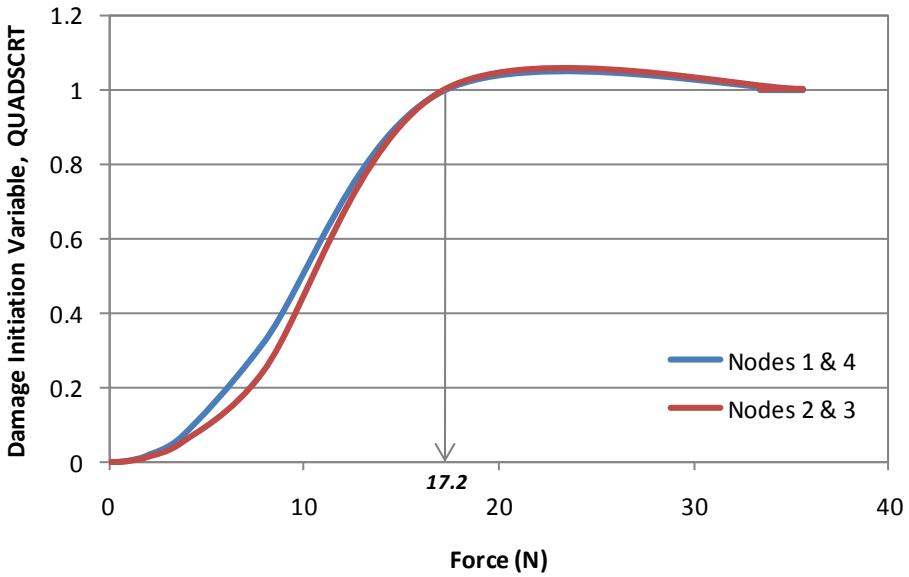

Figure 3.11. Damage Initiation Variable versus Applied Force for the Nodes of an Interface Element

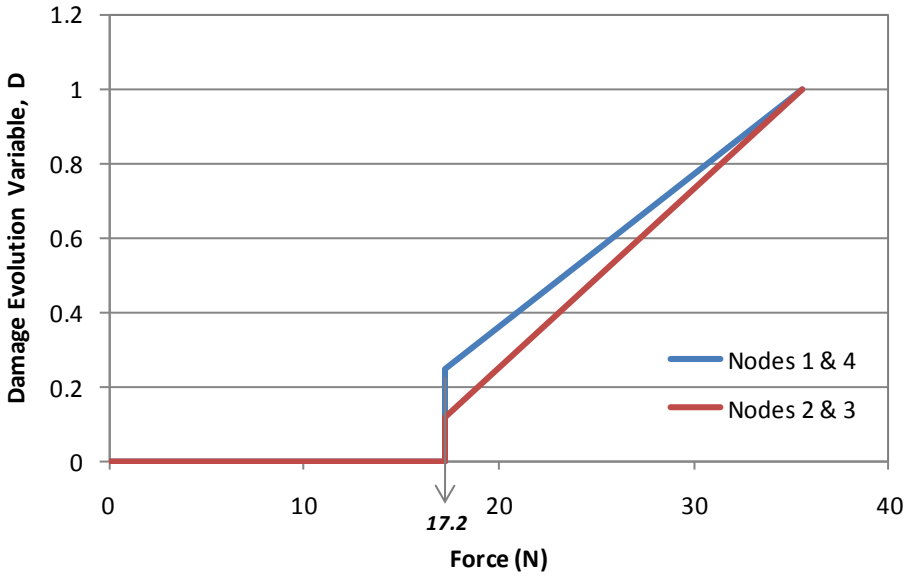

Figure 3.12. Damage Evolution Variable versus Applied Force for the Nodes of an Interface Element

When the applied force reached 17.2 N and damage was initiated, the traction stress that the interlaminar elements were able to sustain was reduced according to the damage evolution law described in Equation 3.8. The disturbed state damage variable D_e was linearly reduced by equating the area under the traction-separation curve to the fracture energy required to open a unit area of interlaminar crack, G_C as shown in Table 3.4. The damage variable was increased until it reached a value equal to one and the interlaminar elements could no longer sustain a traction force, causing complete failure of the elements. This process continued until the entire composite beam was delaminated.

The damage initiation versus force curve shown in Figure 3.11 may be used to predict the force at which damage will occur in the interface of an IM7/977-2 composite panel subjected to peeling (Mode I loading). The damage evolution variable, D_e, versus force data shown in Figure 3.12 may be used to predict the force at which damage has completely evolved and the interface of the composite material can no longer sustain a force.

The damage evolution of the interface material reference element in terms of stress versus logarithmic strain is shown in Figure 3.13. Figure 3.13 shows the maximum quadratic stress of 5.7 MPa reached within the interface material and the resulting linear damage evolution behavior. The stresses that the interlaminar elements were able to maintain were systematically reduced until the elements could no longer sustain stress.

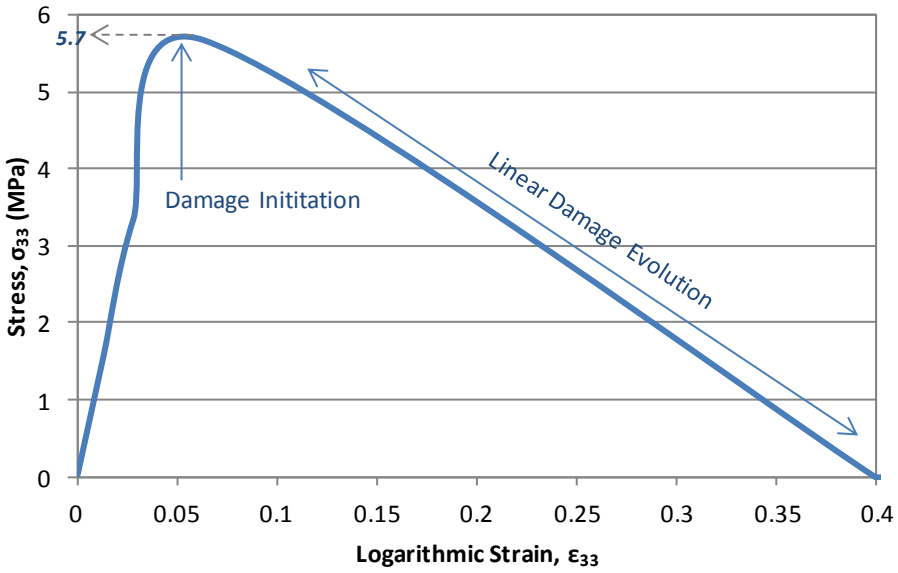

Figure 3.13. Stress σ_{33} versus Strain ε_{33} in Interface Material

The results obtained in the finite element modeling performed in this study were compared to the interlaminar toughness laboratory test results study of an IM7/977-2 composite beam (Johnson et. al. 2005). The force versus displacement curve obtained during laboratory testing for an 8-ply, $[0_3/\pm3/0_3]$ layup composite panel at room temperature is shown in Figure 3.14.

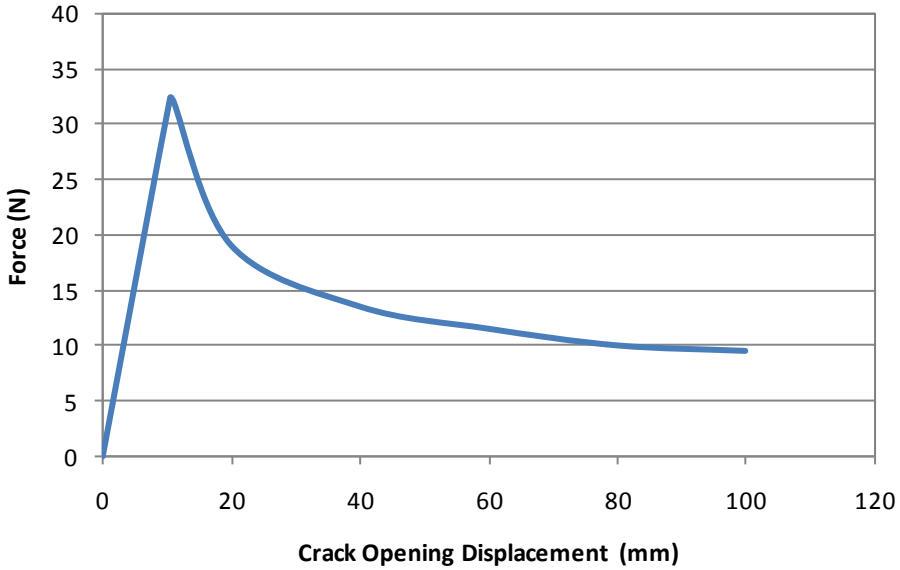

Figure 3.14. Force vs. Displacement Curve for IM7/977-2 Double Cantilever Beam according to Johnson et. al. (2005)

The finite element model developed in this study correlates well with the laboratory test results obtained during the Johnson experiment. In the current study, a maximum force of 35.5 N with an associated displacement of 21.9 mm was obtained from the ABAQUS finite element model. This result is in agreement with the maximum force of 32.3 N obtained from the laboratory testing of an 8-ply, $[0_3/\pm3/0_3]$ layup IM7/977-2 composite panel performed by Johnson et al. (2005). The associated displacement obtained in the Johnson et al. (2005) laboratory testing was 10.5 mm for a single composite panel with a total displacement of 21 mm for both panels, which is in agreement with the results obtained in the present study.

3.9.1 Damage to Composite Panels

A contour plot of the DSC/ductile damage initiation variable for a cantilever beam subjected to an applied displacement is shown in Figure 3.15. As shown in this figure, damage was not initiated in the top or bottom composite panels under the applied displacement. This result was expected, as the strength of the composite panels was much larger than that of the interface material.

The stress-strain curve for the composite panel is shown in Figure 3.16. As shown in Figure 3.16, the stress state of the bottom surface of the upper composite panel reached a maximum tensile stress of 833 MPa with an associated strain of 4.95×10^{-3}. The top surface of the upper panel reached a compressive stress of 833 MPa. This stress state indicates that the composite panels did not reach the failure stress specified in Table 3.3 and damage was not initiated in the composite panels.

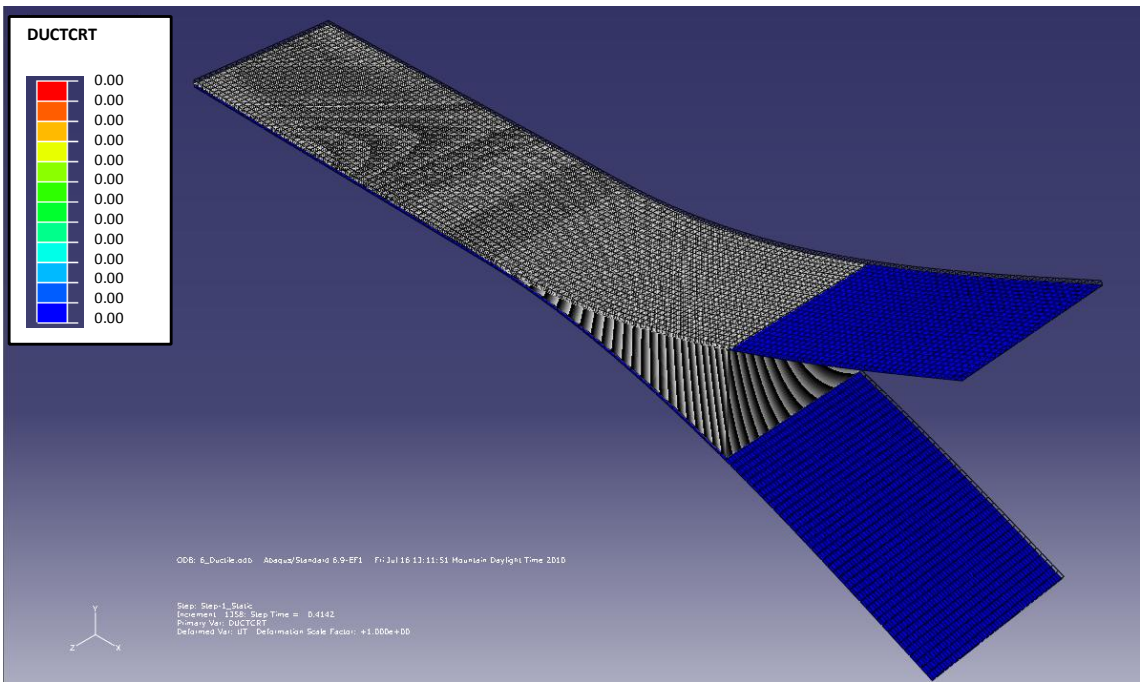

Figure 3.15. Ductile Damage Initiation Variable Contour Plot for Double Cantilever Beam

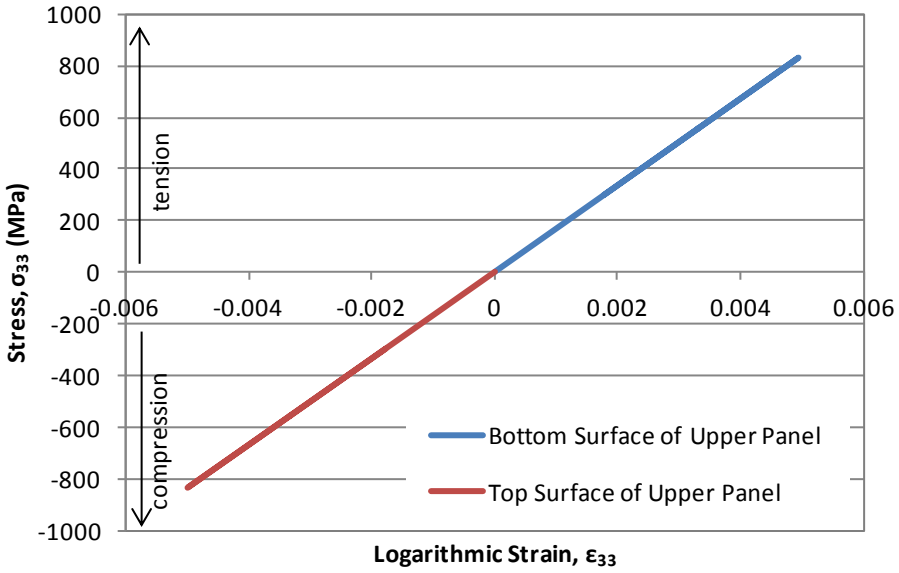

Figure 3.16. Stress σ_{33} versus Strain ε_{33} in Upper Panel

3.10 CHAPTER CONCLUSIONS

A double cantilever beam composed of IM7/977-2 composite material subjected to Mode I loading was successfully modeled in ABAQUS as described in this chapter. Chapter conclusions include:

- Bulk and interlaminar damage models were successfully combined in ABAQUS to model the IM7/977-2 composite double cantilever beam subjected to Mode I loading.
- The finite element model predicted the interlaminar behavior of the material with reasonable accuracy compared to laboratory data.
- Damage within the interlaminar material of an 8-ply, IM7/977-2 composite panel at room temperature will occur at an applied Mode I "peeling" force of 35.5 N with an associated displacement of 21.9 mm.
- This corresponds to an interface traction strength ($t°$) value of 5.95 MPa with an associated interlaminar critical fracture energy (G_C) value of 0.2973 mJ/mm^2.
- All input parameters required for modeling material damage for a double cantilever beam composed of IM7/977-2 composite material subjected to Mode I loading within ABAQUS were defined in this study.

The damage modeling experience gained through modeling a polymeric composite material in ABAQUS finite element modeling software was used to explore damage with asphalt composite materials, as shown in Chapter 4.

4 EXTENDED FINITE ELEMENT FRACTURE MODELING OF ASPHALT PAVEMENT

4.1 INTRODUCTION

Asphalt pavements deteriorate over time due to repetitive loading from traffic, water infiltration, and weather conditions. Asphalt pavement deterioration can take many forms, such as cracks, ruts, potholes, and other depressions. As deterioration progresses, pavement rehabilitation is required to repair distresses and bring the pavement back to a serviceable condition. A common rehabilitation method for older pavements is to overlay the existing asphalt with a layer of hot mix asphalt (HMA). Cracks within the existing asphalt are usually filled with crack sealant before the HMA overlay is placed. However, it is common for cracks to be overlooked during the rehabilitation and not be sealed before placement of the overlay. These unsealed cracks can negatively impact the performance of the HMA overlay by causing stress concentrations and possible failure in the HMA overlay above the cracks.

The methods used in this study utilized the principals of the disturbed state concept (DSC) as described by Desai (2007) through the use of the extended finite element method (XFEM) within ABAQUS finite element modeling software. The models used in this study also offered a unique advantage from the traditional DSC method because they allowed discrete fractures to form in the material without having to define a geometric fracture in the finite element geometry of the material before loading occurs. Rather, a discrete crack formed through element splitting when a critical damage value was reached without the need for a preexisting crack to be present. The XFEM method is

mesh independent, so mesh refinement was not necessary to predict accurate cracking behavior.

The XFEM method was introduced by Belytschko and Black (1999), who created a technique that would minimize the amount of remeshing required to model crack growth in a finite element framework. The method utilized enrichment functions to represent the crack Thus, the crack geometry itself does not require meshing, does not need to be aligned with the mesh, and can be placed at any location within the material. The method introduced by Belytschko and Black (1999) utilized the partition of unity concept introduced by Melenk and Babuska (1996), in which enrichment functions are incorporated into a finite element framework. The enrichment functions are near-tip asymptotic fields and discontinuous functions that represent the jump in displacement at the crack interface (Moes et al., 1999). The functions allow the crack to have additional degrees of freedom from the surrounding material.

The XFEM method has been used to model the failure behavior of construction materials. The method was used to model cohesive crack growth in concrete through traction-separation relationships by Moes and Belytschko (2002) and was specifically utilized to predict cracking in asphalt under low temperatures by Zhao and Wang (2002). However, the Zhao and Wang (2002) study modeled preexisting asphalt cracks as a discrete geometry within the asphalt material. The XFEM method was also used to model longitudinal cracking in asphalt by Feng et al. (2011).

The XFEM method has been implemented through ABAQUS finite element software by several researchers. Song et al. (2006) used the XFEM phantom node approach available in ABAQUS to model crack growth through the use of traction-separation laws. Giner et al. (2009) and Shi et al. (2010) also performed XFEM modeling in ABAQUS but developed a user subroutine to implement a specific XFEM modeling method that described crack growth by through nodal degree of freedom enrichment and discontinuous functions.

4.2 CHAPTER OBJECTIVES

The objective of this chapter was to implement a damage model that allows prediction of failure and fracture behavior in an asphalt pavement without having to define a damaged and undamaged zone. Any part of the asphalt was allowed to fracture based on the current stress state in the material. The models developed in this study implemented the XFEM method in ABAQUS to model failure of asphalt through cohesive zone traction-separation. The failure behavior of an HMA overlay above an existing asphalt pavement under an applied displacement was modeled. Two scenarios were studied: a pavement with pre-existing cracks in the existing asphalt layer and a pavement without pre-existing cracks.

4.3 DAMAGE BEHAVIOR OF ASPHALT

Damage initiation marks the starting point of the degradation of material at the crack surface interface within the asphalt material. Damage initiation for asphalt materials was defined according to the traction-separation modeling concept described in Section 3.4.2.

A stress-based stress damage initiation criterion as described in Section 3.4.3 was used to define the stress state at which the asphalt material first experienced damage. A maximum principal stress criterion was established instead of defining damage initiation in the three principal coordinate directions. Damage initiated when the stress ratio within the asphalt material reached a value of 1 as shown in Equation 4.1 (Dassault Systemes, 2009):

$$f = \frac{\langle t_{\max} \rangle}{t^0_{\max}} = 1$$

Equation 4.1

where f = damage initiation variable, t_{max} = principal stress within the element under loading, and t^0_{max} = principal stress at which damage is initiated. The Macaulay brackets ⟨ ⟩ in Equation 4.1 signify that a purely compressional stress within the material will not initiate damage. Damage within the material initiated when the damage initiation variable f was equal to 1.

Damage evolution was defined according to a traction-separation law as described in Section 3.5.2. Damage was described through Equation 4.2:

$$t_{\max} = (1 - D_{XFEM}) \cdot \bar{t}$$

Equation 4.2

Where t_{max} = current maximum principal traction stress at the crack interface during loading, $\bar{t}$ = the traction stress predicted by the linear elastic traction-separation behavior

without damage, and D_{XFEM} is the extended finite element analysis damage evolution variable. Damage initiated when D_{XFEM} was greater than zero and completely evolved when D_{XFEM} was equal to one. The complete damage behavior of asphalt material was defined by specifying the traction-separation curve shown in Figure 3.1. Input parameters included the maximum principal stress at which damage initiates and the cohesive zone fracture energy G_C.

4.4 CRACK LOCATION AND PROPAGATION

Cracks within the asphalt were modeled using the ABAQUS XFEM method where cracks can initiate in any location within the material and crack propagation is not confined to element boundaries within the finite element mesh. This degree of separation across a crack was determined through the phantom node approach available in the ABAQUS XFEM model. The phantom node approach is shown graphically in Figure 4.1. Phantom nodes were superimposed on the element nodes before displacement was applied to the asphalt. Element stress increased with applied displacement until the damage initiation criterion was satisfied. A crack formed within the element at this point and the phantom and real nodes began to move apart. The phantom nodes and real nodes moved independently of one another when the damage evolution criterion was satisfied and the traction strength of the cracked element was equal to zero. The element then physically split apart and formed a discrete crack; the crack formation and propagation was not dependent on the finite element mesh. With the phantom node approach, the crack near-tip stress singularity was not determined; rather, only the displacement jump across a cracked element was utilized. Because of this, the crack propagated across an

entire element at a time to avoid the crack near-tip singularity calculation. The crack geometry was described within the ABAQUS XFEM method using the level set method (Dassault Systemes, 2009). The geometry of the crack was defined by two near-orthogonal distance functions which described the crack surface and an intersecting orthogonal surface that represented the crack front.

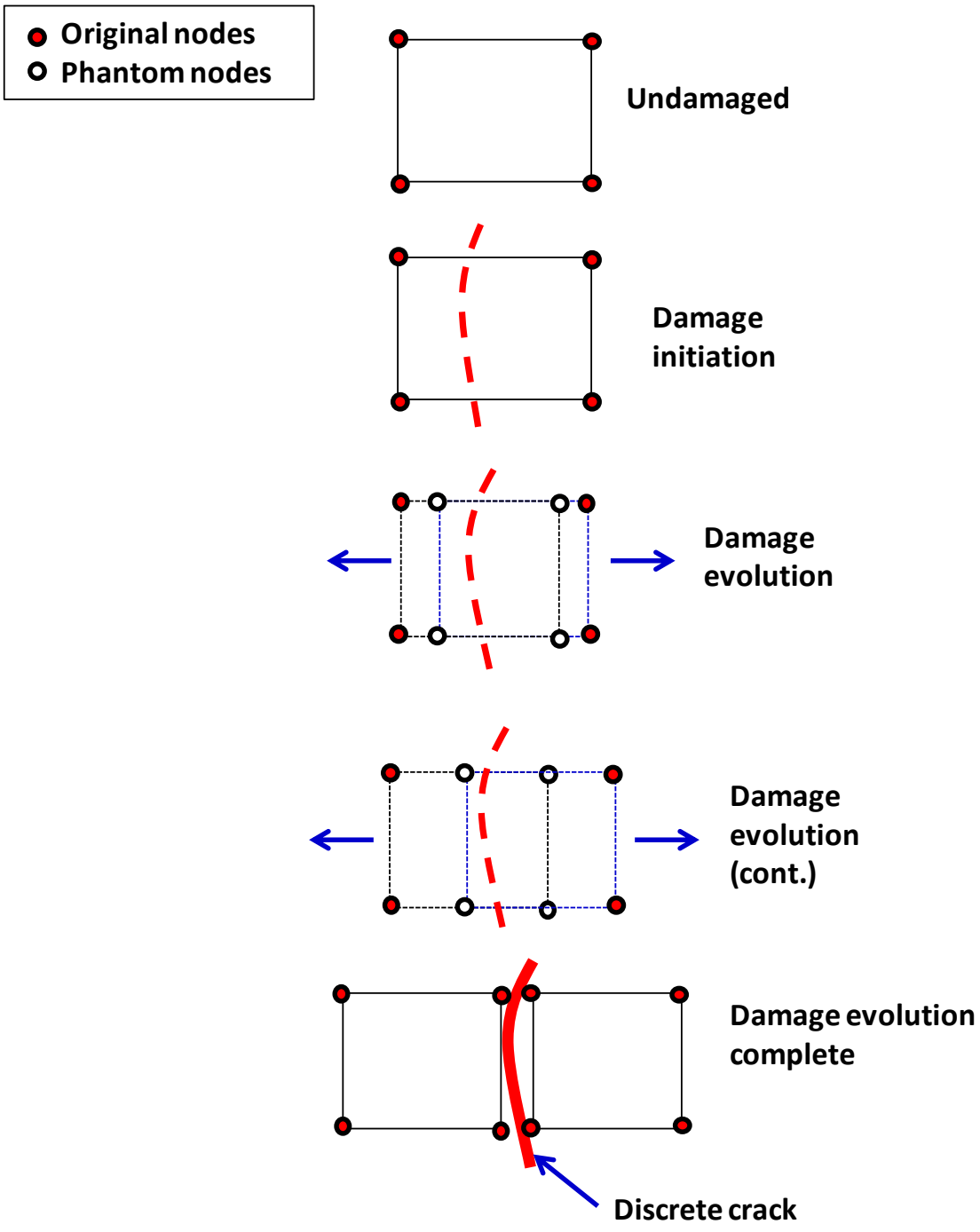

Figure 4.1. ABAQUS Phantom Node Approach

4.5 METHODOLOGY

Traction-separation response, damage initiation and damage evolution were studied in an asphalt pavement with an HMA overlay modeled in ABAQUS. Material properties were

based on damage studies by Desai (2007), Chen (2010), and Tarefder et al. (2010). Damage initiation material properties were based on indirect tensile testing (IDT) of asphalt specimens performed by the author at the University of New Mexico asphalt laboratory. Asphalt evolution material properties were based on a fracture damage study by Aragão et al. (2011).

4.5.1 Asphalt Indirect Tensile Laboratory Testing

In order to determine the cohesive zone strength (t^0_{max}) of asphalt, indirect tensile (IDT) strength tests were performed on two asphalt cylinders composed of Superpave SP-III mixture prepared from a New Mexico local supplier in cooperation with the New Mexico Department of Transportation. The SP-III mixture was composed of sand, aggregate, crushed recycled asphalt pavement from a local interstate source, and asphalt binder. The composition of the SP-III mix is shown in Table 4.1 and the gradation of the granular portion is shown in Table 4.3. Two asphalt specimens used in IDT testing were prepared using the SP-III mixture at the University of New Mexico asphalt laboratory. Each specimen was compacted to 6% air voids, had a diameter of 4 in (100 mm), and was approximately 1.8 in (45 mm) thick.

Table 4.1. SP-III Asphalt Composition

Granular Portion	95.4%			
Aggregate and Sand	80.1%			
Crushed Recycled Asphalt	14.3%			
Hydrated Lime	1.0%			
Bituminous Portion	4.6%			
PG 70-22 binder				
Granular Gradation	1 in (25 mm)	0.5 in (12.5 mm)	No. 8 (2.36 mm)	No. 200 (0.075 mm)
Passing	100%	80%	25%	3.4%

Table 4.2. SP-III Asphalt Granular Portion Gradation

Sieve Size	Percent Passing
1 in	100
3/4 in	94
1/2 in	80
3/8 in	67
No. 4	34
No. 8	25
No. 16	17
No. 30	12
No. 50	7.7
No. 100	4.7
No. 200	3.4

IDT testing was performed according to ASTM D6931, "Standard Test Method for Indirect Tensile (IDT) Strength of Bituminous Mixtures". A photo of the test set-up is shown in Figure 4.2. A compressive load was applied to a cylindrical asphalt specimen along its short axis with a hydraulic loading device using ½-in wide steel loading strips. The load was applied to the asphalt specimens at a constant displacement rate of 2 in/minute (50 mm/min) until the specimen cracked. Photos of the cracked specimens are shown in Figure 4.3. The test was repeated on the specimen axis perpendicular to the crack in order to obtain the IDT strength of damaged asphalt. Test results are presented in Figure 4.4. The results of the material properties obtained through IDT testing are shown in Table 4.3.

The IDT strength of the specimen, which is the horizontal tensile stress at the center (Zaniewski and Srinivasan, 2004), was calculated using Equation 4.3 (ASTM D6931):

$$S_t = t^0_{\max} = \frac{2 * P}{\pi * t * D}$$

Equation 4.3

where S_t = IDT strength (psi), P = maximum load applied to the specimen (lbf), t = specimen height immediately before the test (in), D = specimen diameter (in), and t^0_{max} = principal stress at which damage is initiated.

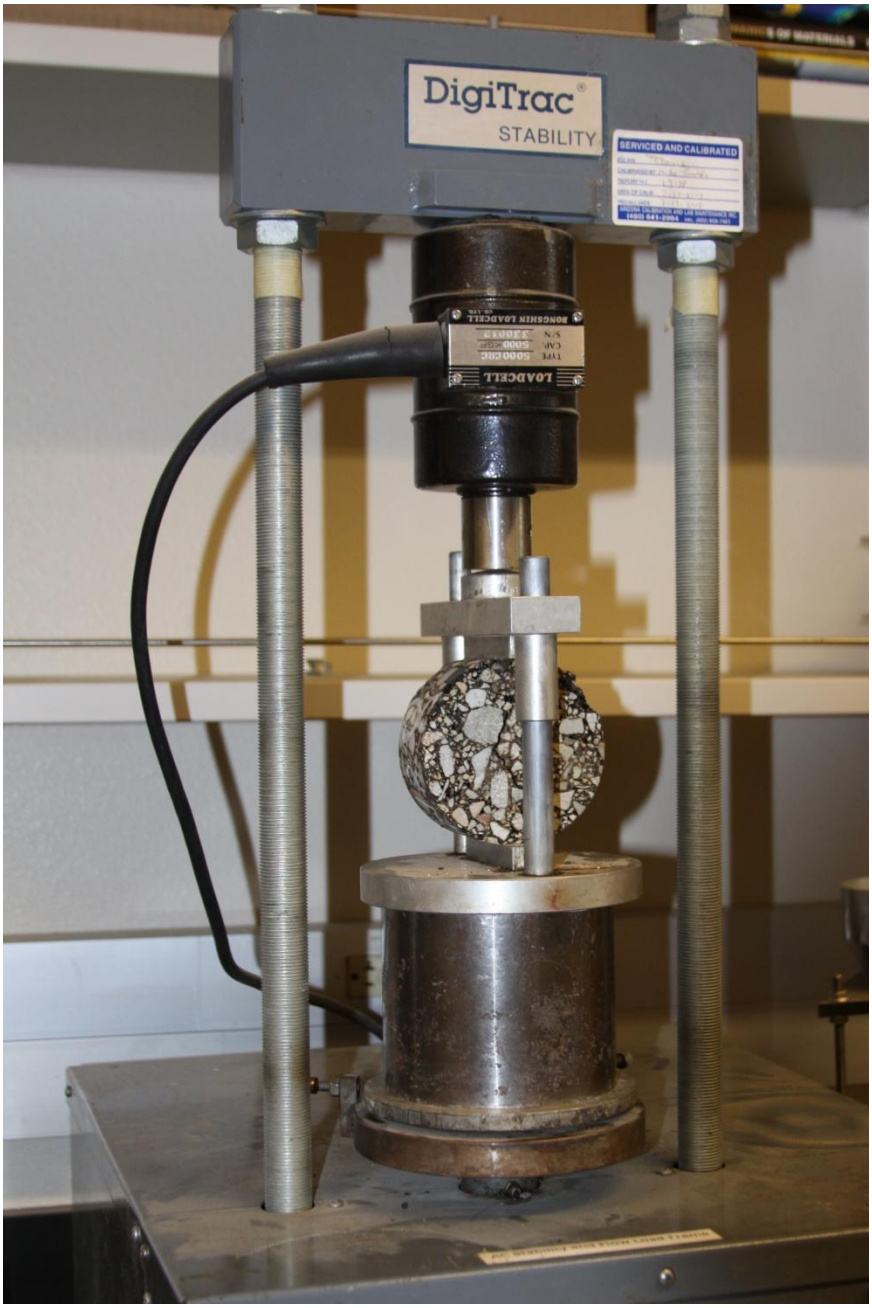

Figure 4.2. IDT Testing Apparatus

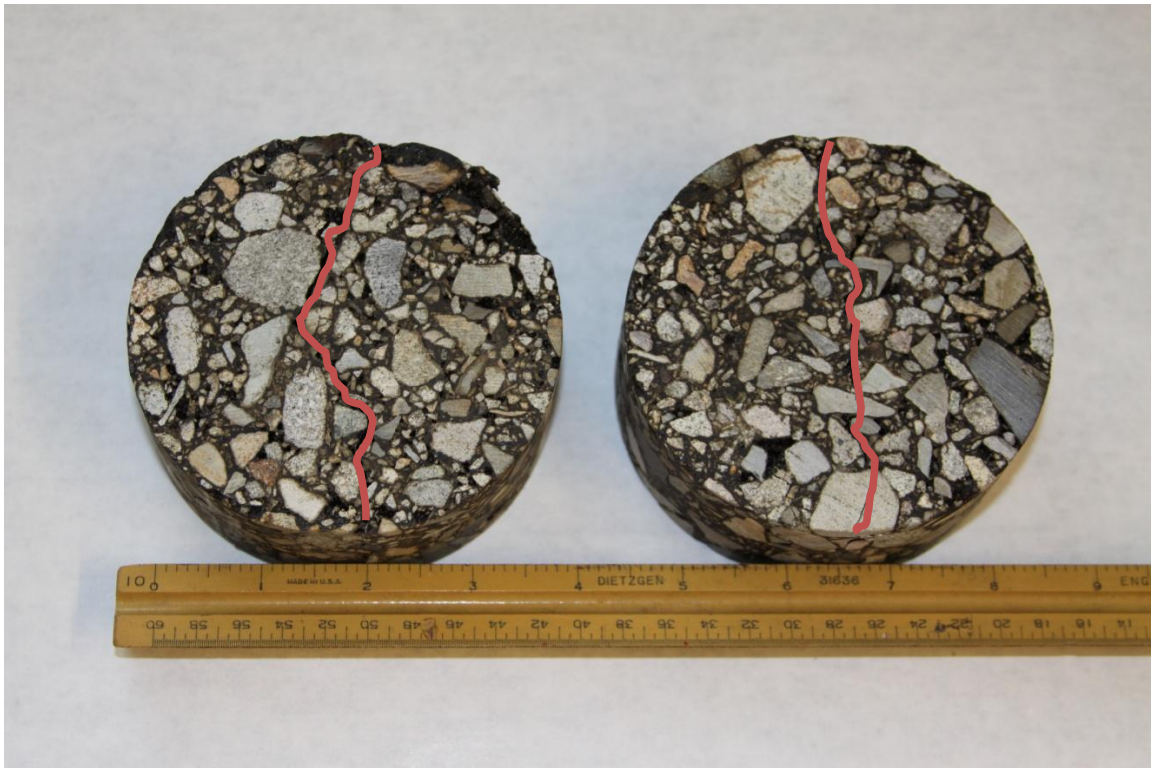

Figure 4.3. Asphalt Cylinder Specimens after Completion of IDT Test

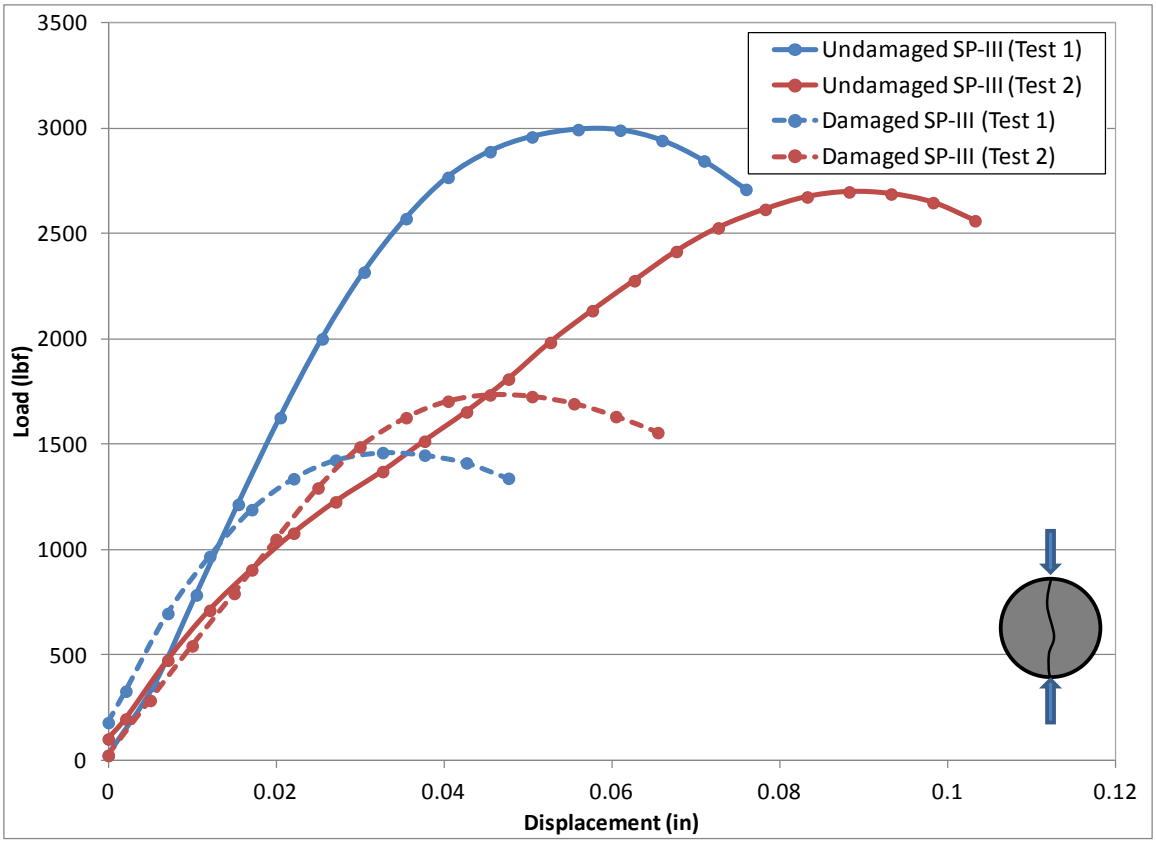

Figure 4.4. IDT Load versus Displacement Test Results

Table 4.3. IDT Strength Test Results

	Undamaged SP-III (Specimen 1)	Undamaged SP-III (Specimen 2)	Damaged SP-III (Specimen 1)	Damaged SP-III (Specimen 2)
Diameter, D (in):	4	4	4	4
Height, t (in):	1.875	1.875	1.875	1.875
Load at Failure, P (lbf):	2994	2698	1460	1734
IDT Strength, S_t (psi):	254.1	229.0	123.9	147.2
Average IDT Strength, S_t	Undamaged SP-III		Damaged SP-III	
(psi):	241.58		135.56	
MPa:	1.67		0.93	

4.5.2 Asphalt Indirect Tensile Test Finite Element Modeling

IDT testing of an asphalt cylinder was modeled two-dimensionally in ABAQUS to validate the laboratory results obtained in this study. The geometry and the boundary conditions for the asphalt core are show in Figure 4.5. The model utilized identical dimensions to the IDT laboratory test specimens and used the elastic material properties (Young's Modulus and Poisson's ratio) for SP-III mixtures as described by Tarefder et al. (2010). The cylinder base had fixed boundary conditions constraining displacement and rotation in the x, y, and z directions. A displacement was applied to the top of the cylinder to simulate the IDT test.

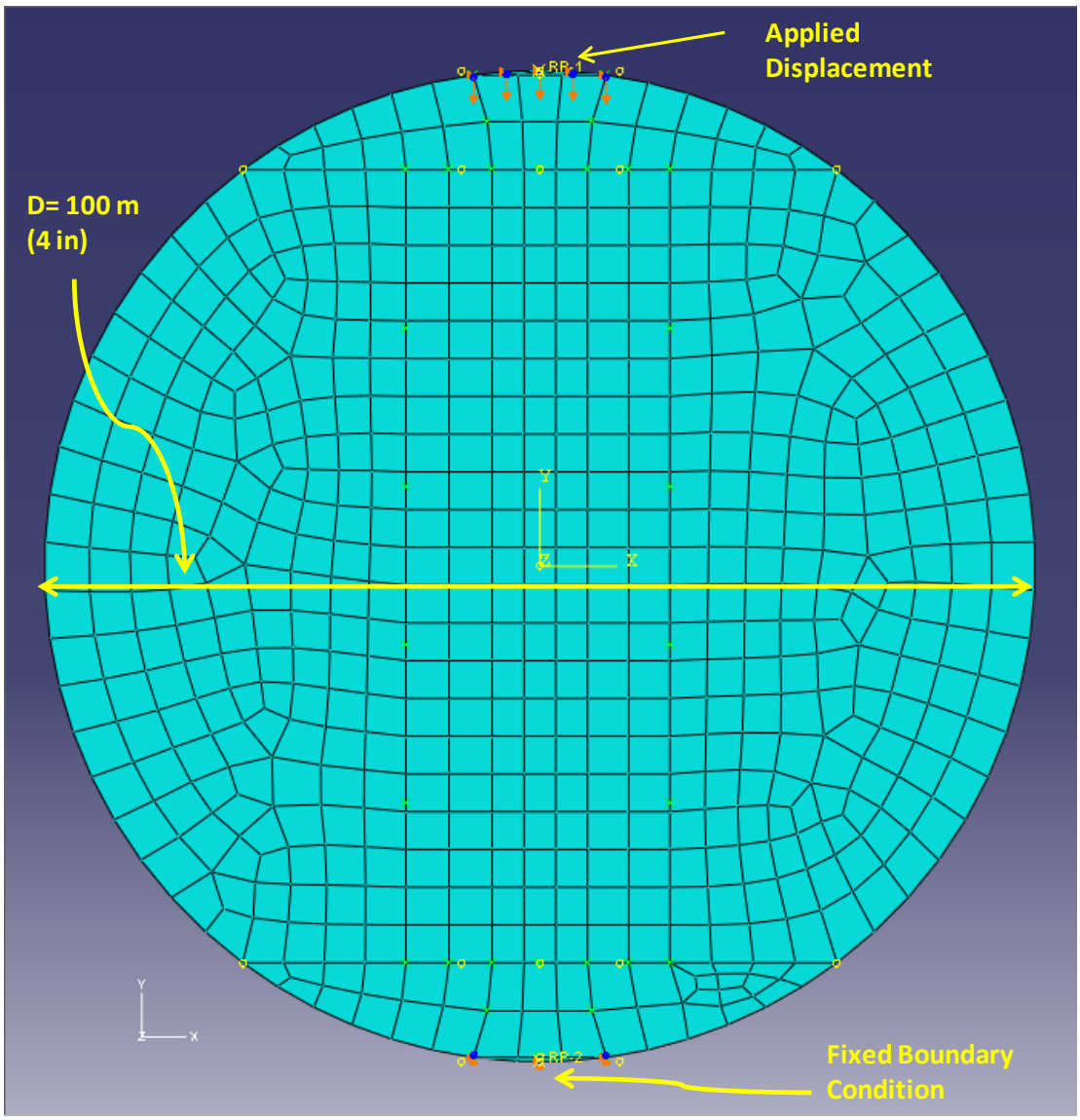

Figure 4.5. Geometry of IDT Test Asphalt Cylinder for Finite Element Analysis

Two finite element models were created to simulate the response of undamaged and damaged asphalt. The first model used the IDT strength for undamaged asphalt (shown in Table 4.4) as the cohesive zone strength (t^0_{max}); the second model utilized the IDT strength of damaged asphalt.

The finite element models exhibited cracking that was very similar to the results obtained in the laboratory testing where cracking occurred under an applied vertical displacement on the cylinder's short axis. The cracked cylinder geometry is shown in Figure 4.6 and the displacement contour plot is shown in Figure 4.7. Tensile stresses developed in the center of the asphalt cylinders under the applied displacement as shown in Figure 4.8. Damage initiated and evolved once the tensile stress reached the IDT strength values shown in Table 4.4. Contour plots of the damage variable D_{XFEM} for asphalt cylinders with damaged and undamaged material properties are shown in Figure 4.9. The red contours indicate that damage has initiated and evolved and that cracking has occurred in the cylinder. These results are in good agreement with the actual crack propagation path observed in the laboratory testing.

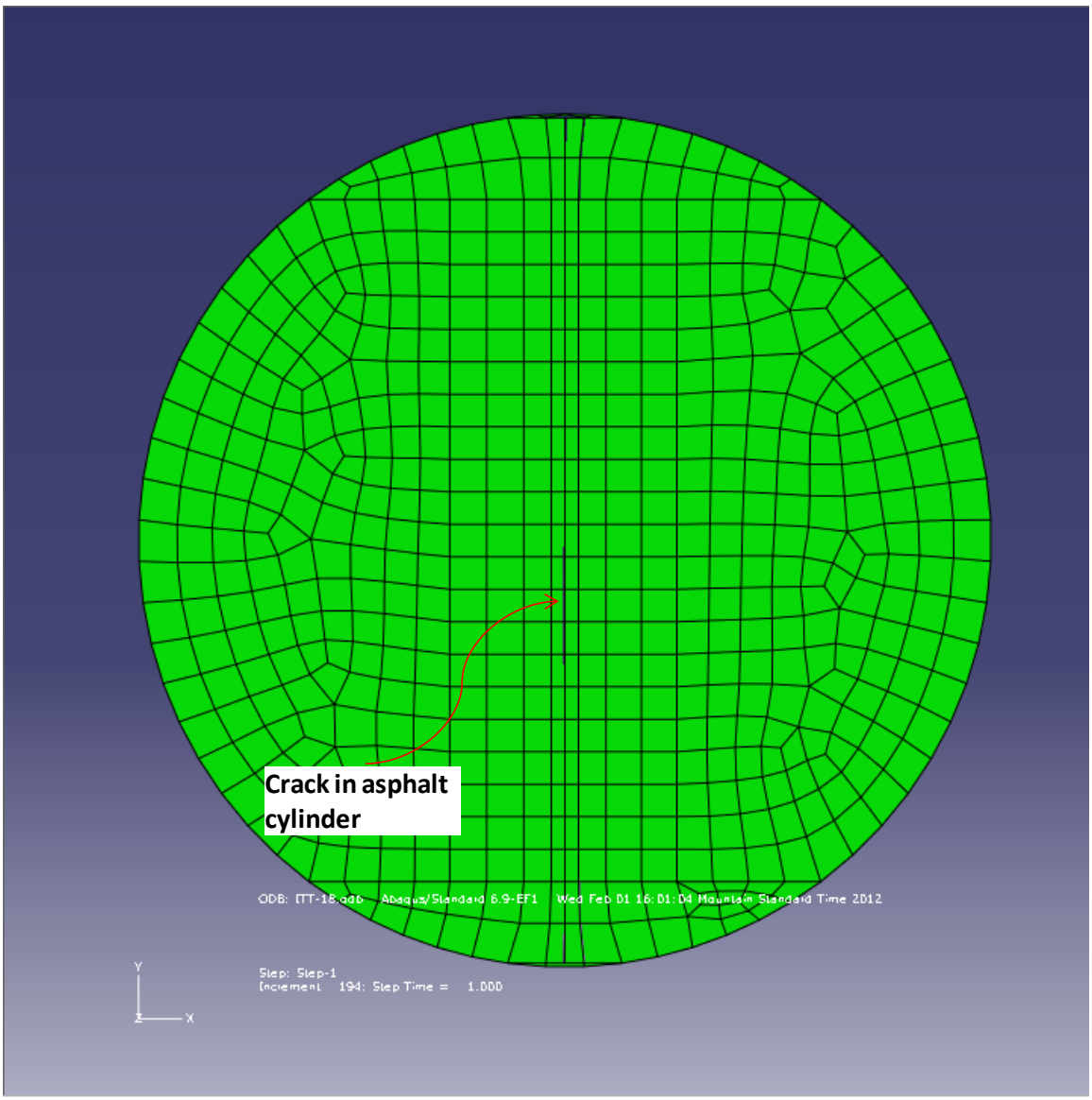

Figure 4.6. Crack Geometry of IDT Asphalt Cylinder

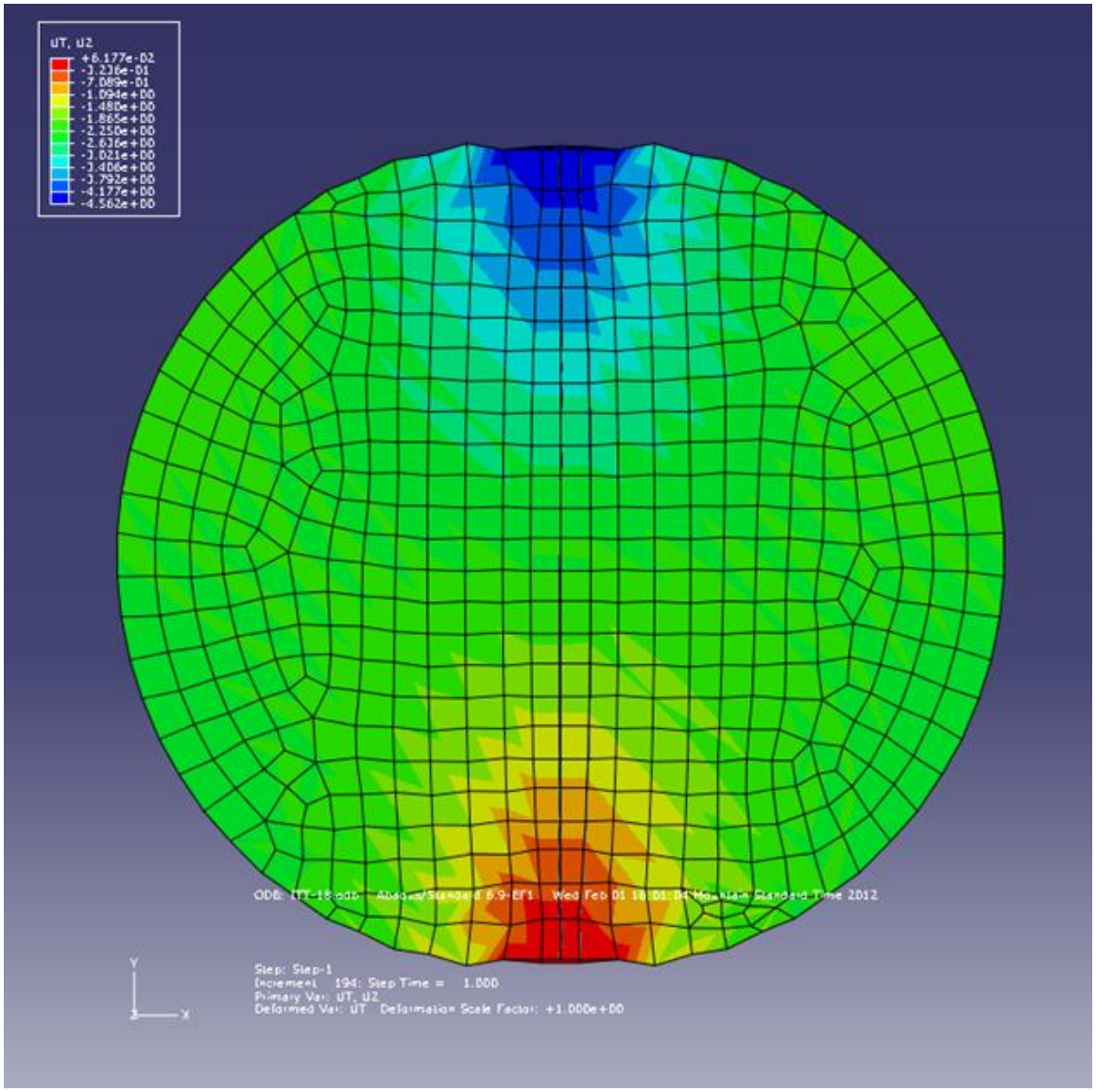

Figure 4.7. Contour Plot of Displacement of the IDT Asphalt Cylinder

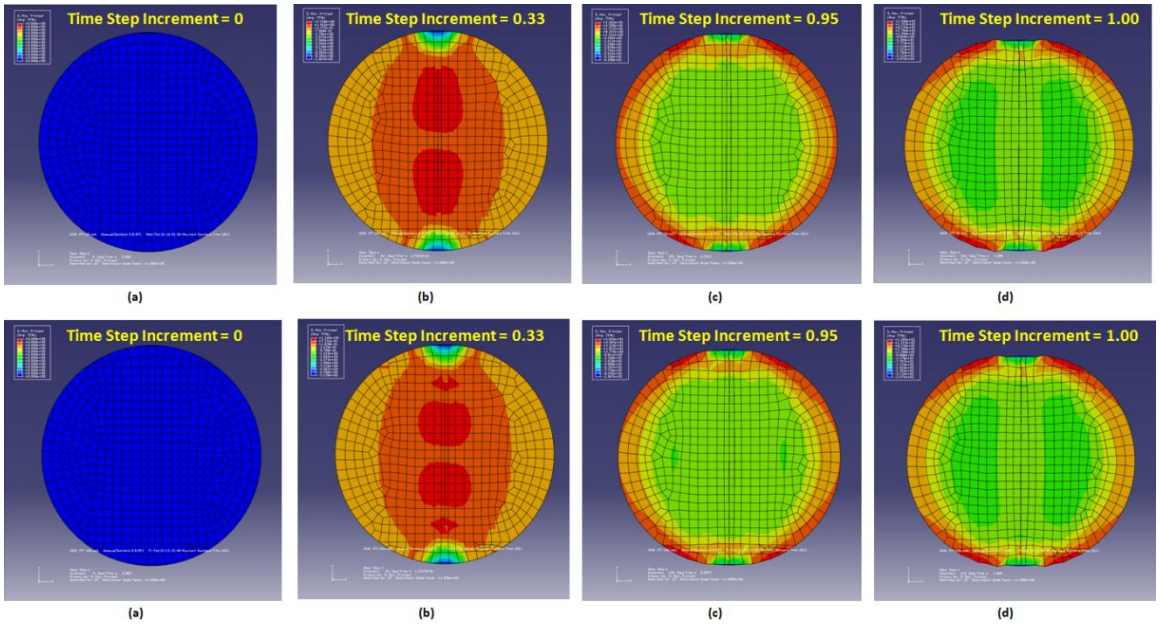

Figure 4.8. Contour Plot of Maximum Principal Stress for Various Time Step Increments for the IDT Asphalt Cylinder with Undamaged Material Properties (top row) and Damaged Material Properties (bottom row)

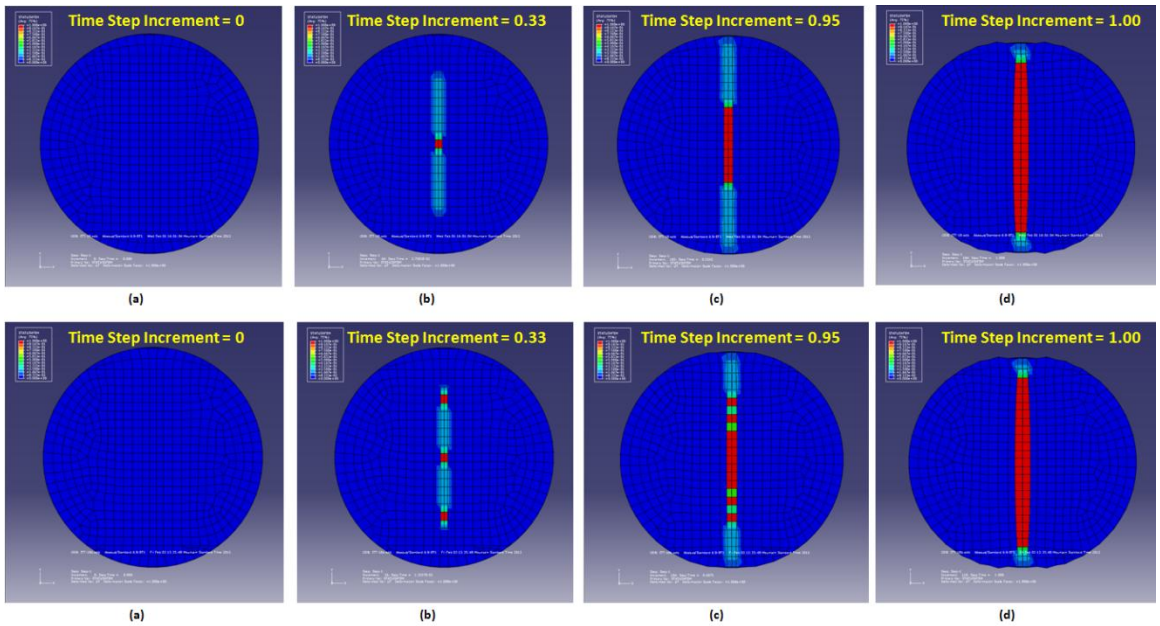

Figure 4.9. Damage Variable D_{XFEM} Contour Plots for Various Time-Steps for the IDT Asphalt Cylinder with Undamaged Material Properties (top row) and Damaged Material Properties (bottom row)

4.5.3 Asphalt Direct Tensile Test Finite Element Modeling

Results of direct tensile laboratory testing by Aragão et al. (2011) were examined to determine the cohesive fracture energy (G_C) for the asphalt material. In the Aragão et al. (2011) study, asphalt cohesive zone fracture properties were determined using uniaxial tensile testing on 75 mm (3 in) diameter, 140 mm (5.5 in) tall asphalt cylinders at room temperature. The tests were performed with a constant displacement rate of 0.28 mm/second. The test results are presented in Figure 4.10 and include an applied force versus displacement curve for the upper cylinder surface. The Aragão et al. (2011) study also included an asphalt cohesive zone strength (t^0_{max}) value of 1.17 MPa (170 psi) and a cohesive fracture energy (G_C) value of 0.339 mJ/mm^2 (1.94 lb-in/in^2).

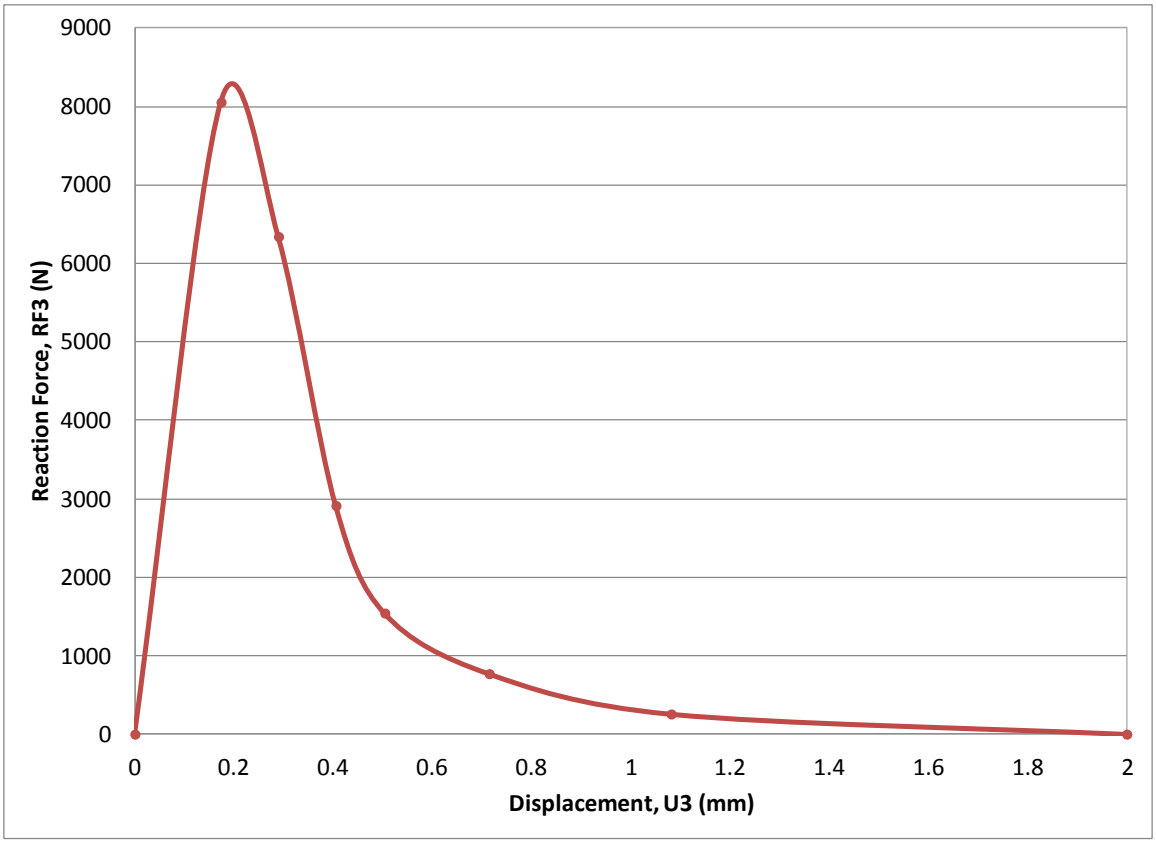

Figure 4.10. Aragão et al. (2011) and Force vs. Displacement Curve for Asphalt Cylinder Loaded in Uniaxial Tension

The average cohesive zone strength (t^0_{max}) of 1.67 MPa (242 psi) for undamaged asphalt determined through the IDT testing performed in this study compares well with the cohesive zone strength of 1.17 MPa (170 psi) determined by Aragão et al. (2011). Based on the close comparison between the cohesive zone strength results, the cohesive fracture energy (G_C) shown in the Aragão et al. (2011) study was used as a starting point to determine the cohesive fracture energy of the SP-III mixture (both undamaged and damaged) tested in the present study. In order to determine the fracture energy of the SP-III mixtures, an asphalt cylinder with the dimensions specified by Aragão et al. (2011) and the asphalt elastic material properties specified by Tarefder et al. (2010) were modeled three-dimensionally in ABAQUS with a displacement applied to the top of the cylinder and a pinned boundary condition constraining displacement and rotation in the x, y, and z directions at the bottom of the cylinder. The geometry and the boundary conditions for the asphalt cylinder are show in Figure 4.11.

Two asphalt cylinder models were created; the first model had a cohesive zone strength (t^0_{max}) of 1.67 MPa (242 psi) of undamaged asphalt shown in Table 4.3 and a cohesive fracture energy (G_C) of 0.65 mJ/mm^2 (3.71 lb-in/in^2). The second model had a cohesive zone strength (t^0_{max}) of 0.93 MPa (135 psi) of undamaged asphalt and a cohesive fracture energy (G_C) of 0.45 mJ/mm^2 (2.57 lb-in/in^2). These cohesive fracture energies were determined by refining the fracture energies and comparing the force versus applied displacement curves for undamaged and damaged SP-III to the Aragão et al. (2011) force versus displacement curve until the tail end of the curves matched as shown in Figure

4.12. In this way, the cohesive fracture energy (G_C) input parameters for undamaged and damaged asphalt were determined.

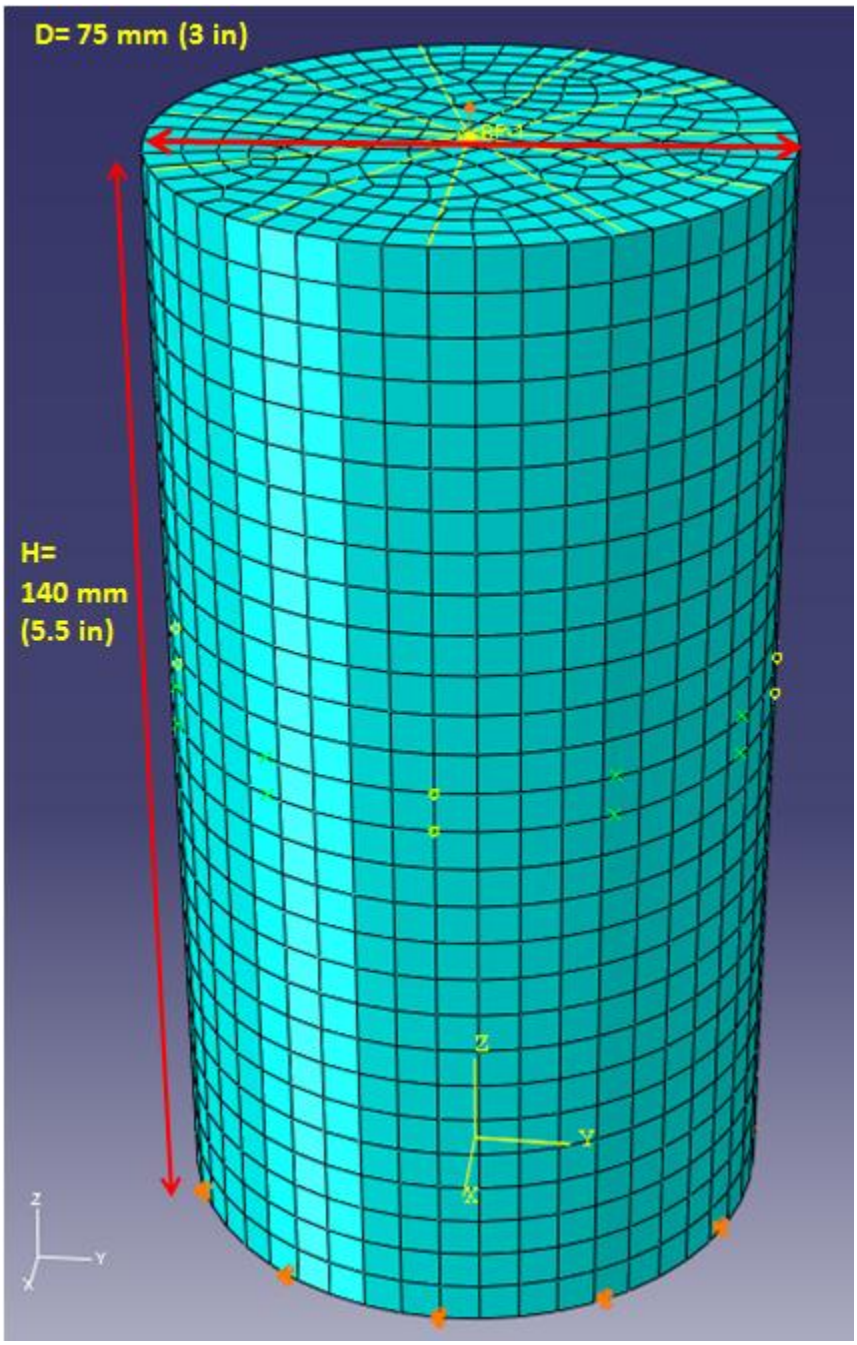

Figure 4.11. Geometry of Asphalt Cylinder for Finite Element Analysis

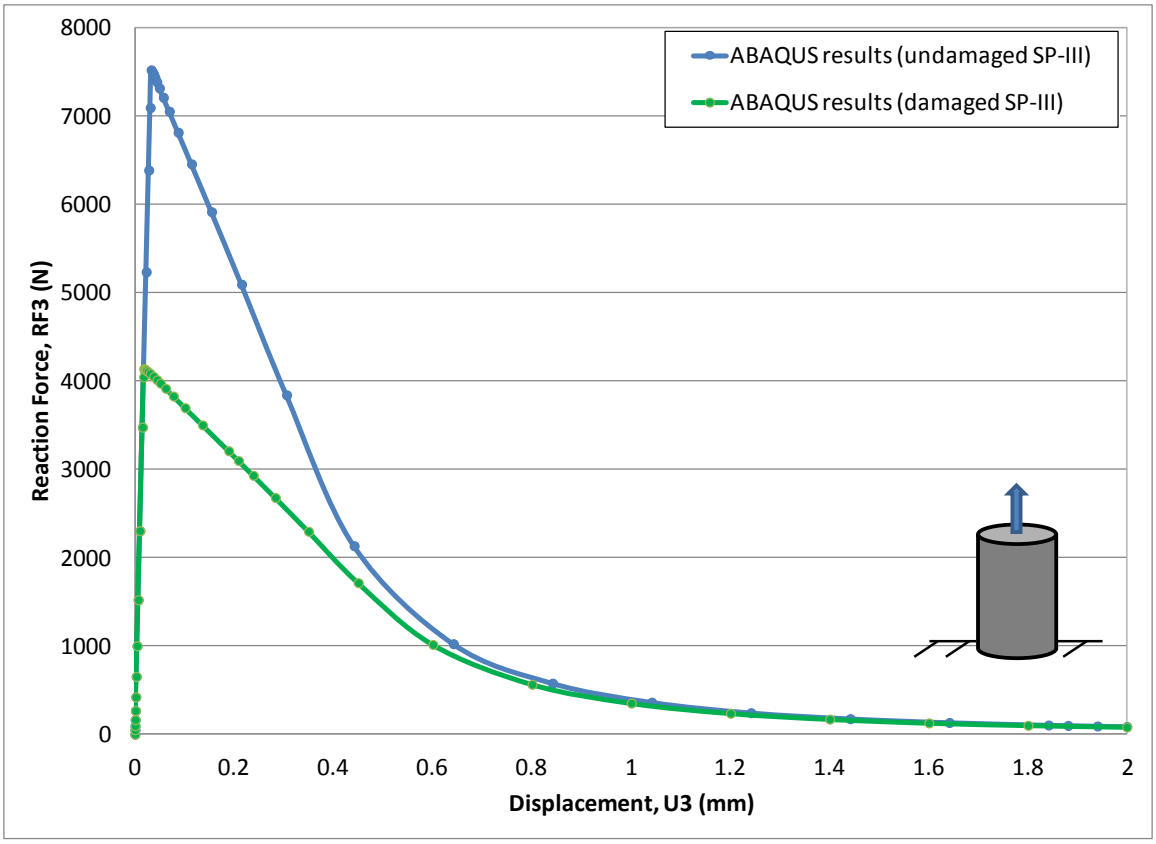

Figure 4.12. IDT Test Finite Element Modeling Force vs. Displacement Curves for Asphalt Cylinders Loaded in Uniaxial Tension

The asphalt cylinders modeled in ABAQUS exhibited cracking in the center under the applied tensile displacement, which is in agreement with the type of failure described in the Aragão et al. (2011) study. A figure of the cracked asphalt cylinder geometry is shown in Figure 4.13. Stress and damage variable contour plots of the asphalt cylinder model with no preexisting cracks are presented in Figure 4.14 and Figure 4.15. The contours in the figures have been exaggerated for ease of visibility.

A contour plot of the maximum principal stress within the cylinder caused by the applied displacement at various time steps is shown in Figure 4.14. This figure shows the principal stress results for the cylinder with the undamaged asphalt material properties as

well as results from the cylinder with damaged material properties. This contour plots are shown on cross sections of the cylinders in order to show the stress concentrations within the interior of the cylinders where cracking occurred. Stress concentrations did occur at the base and top of the asphalt cylinders near the fixed boundary condition and are shown in Figure 4.14. However, the location at which damage was allowed to occur was selected a short distance away from the geometrical boundaries in order to avoid damage from stress concentrations caused by boundary conditions.

A contour plot of the damage variable D_{XFEM} is shown in Figure 4.15. The contours associated with a non-zero value indicate that the maximum principal stress values for damage initiation as shown in Table 4.4 were reached and damage initiated. The contours associated with a D_{XFEM} value of one (red color) indicate that damage within the element completely evolved and cracking occurred. Several screen captures are presented which show the damage variable as time progressed.

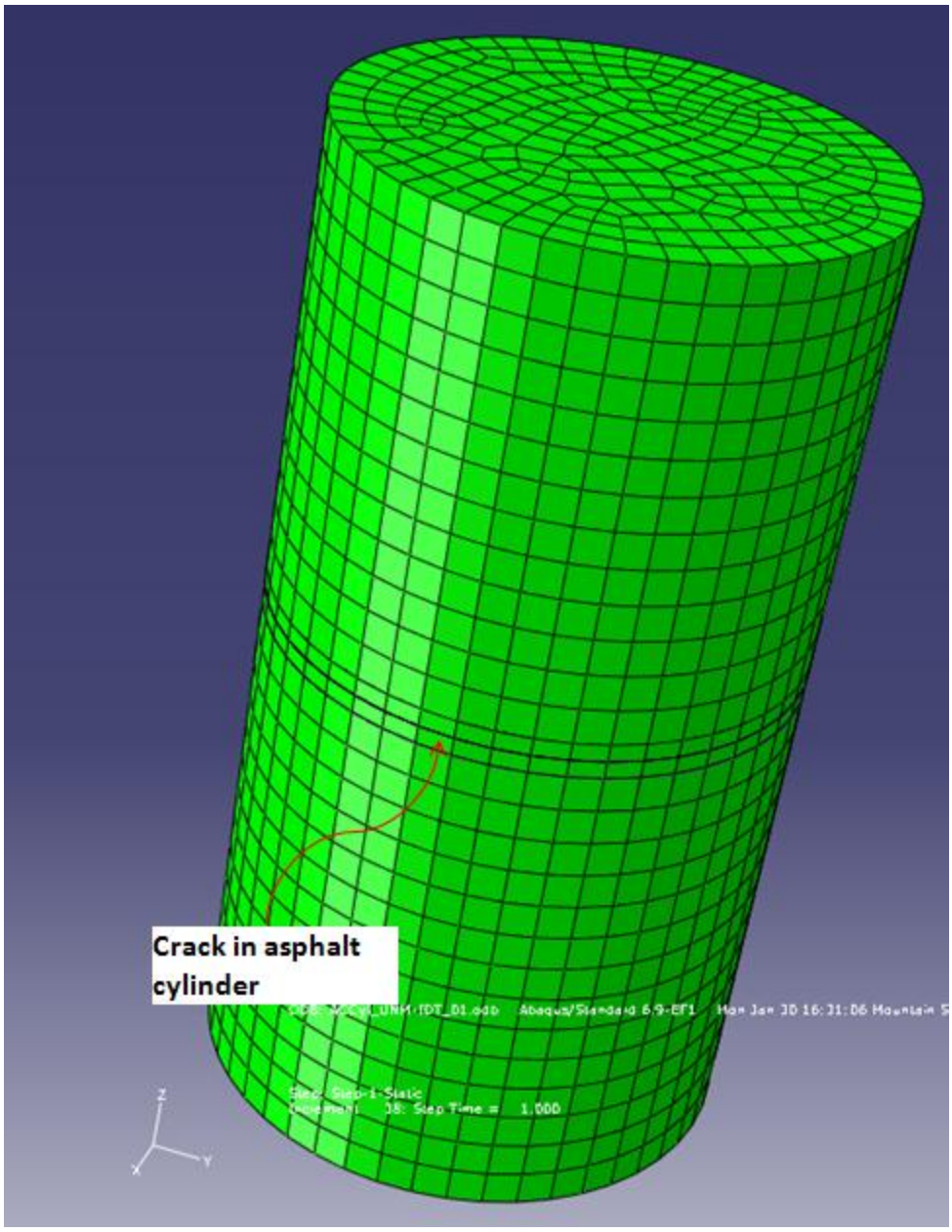

Figure 4.13. Crack Geometry of the Asphalt Cylinder

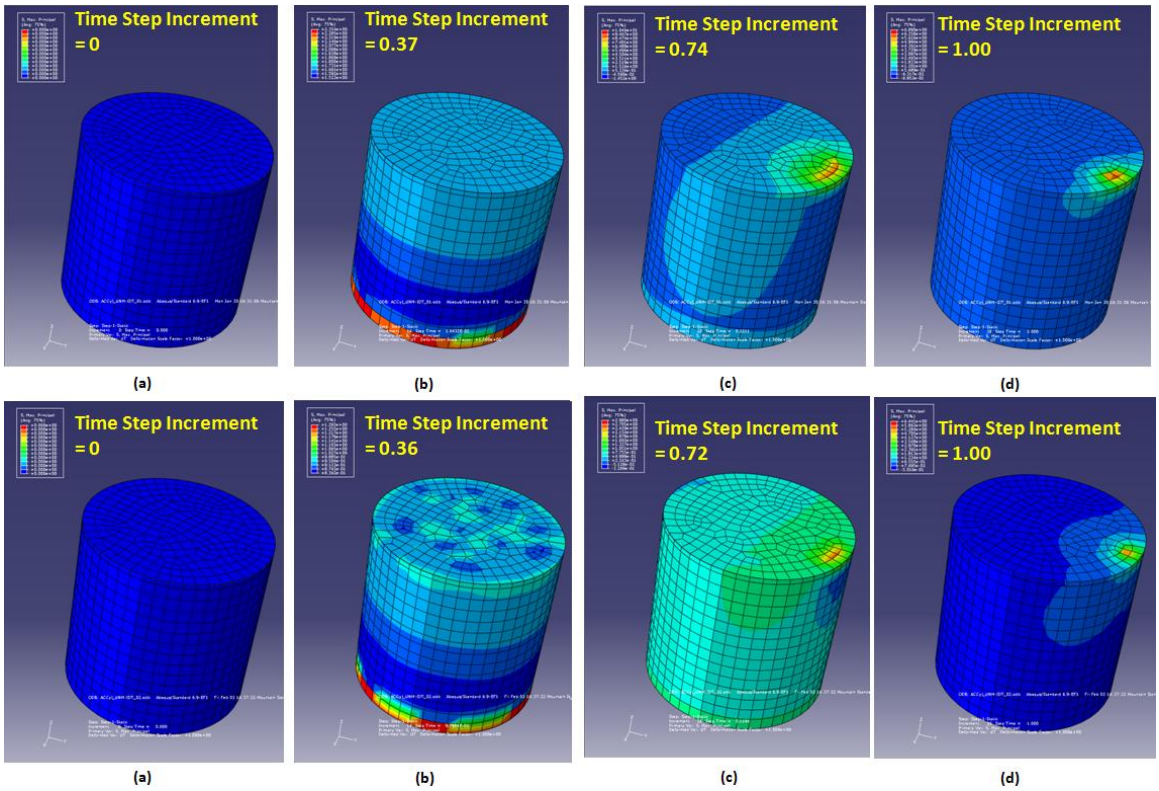

Figure 4.14. Contour Plot of Maximum Principal Stress for Various Time Step Increments for the Asphalt Cylinder with Undamaged Material Properties (top row) and Damaged Material Properties (bottom row)

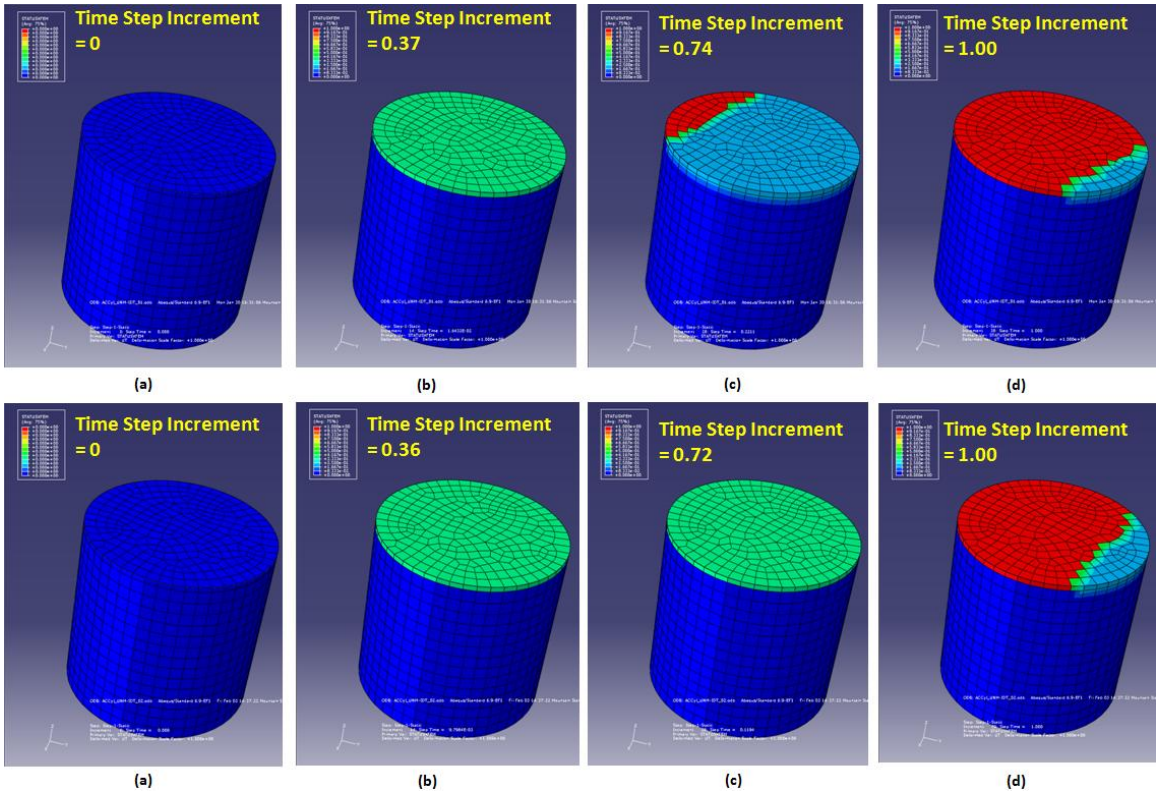

Figure 4.15. Damage Variable D_{XFEM} Contour Plots for Various Time-Step Increments for the Asphalt Cylinder with Undamaged Material Properties (top row) and Damaged Material Properties (bottom row)

4.6 SUMMARY OF MATERIAL PROPERTIES

The material properties for asphalt pavement determined from referenced studies, IDT testing, and direct tensile testing finite element modeling are summarized in the following sections.

4.6.1 Elastic Behavior

The elastic material properties of the pavement system are summarized in Table 4.4. The elastic properties of the subgrade and base course material were obtained from Desai (2007). The Poisson's ratio of the undamaged asphalt and damaged asphalt were obtained from Chen (2010) using a rule of mixtures approach for a composite material

composed of asphalt aggregate and binder. The elastic modulus of asphalt was based on a study on SP-III asphalt mixtures (Tarefder et al., 2010).

Table 4.4. Elastic Material Properties used in Finite Element Analysis

	Undamaged Asphalt	Damaged Asphalt	Base Course	Subgrade
Elastic Modulus, E (MPa):	7000	7000	390	69
Elastic Modulus, E (ksi):	1015	1015	56.5	10
Poisson's Ratio, ν:	0.35	0.35	0.33	0.24

4.6.2 Damage Initiation and Evolution

The cohesive zone strength (t^0_{max}) damage initiation parameter for undamaged asphalt and damaged asphalt were obtained from the IDT testing performed in this study as shown in Table 4.3 and described in Section 4.5.2. The cohesive fracture energy (G_C) damage evolution parameter was obtained from finite element modeling of an asphalt cylinder in direct tension as described in Section 4.5.3. Damage evolution parameters are summarized in Table 4.5.

Table 4.5. Damage Material Properties used in Finite Element Analysis

	Undamaged Asphalt	Damaged Asphalt
Peak traction stress, t^0_{max} (MPa):	1.67	0.93
Peak traction stress, t^0_{max} (psi):	242	135
Cohesive fracture energy, G_C (mJ/mm^2)	0.65	0.45
Cohesive fracture energy, G_C (lb-in/in^2)	3.71	2.57

4.7 PAVEMENT SYSTEM FINITE ELEMENT MODELING

The asphalt material properties described in Section 3.7 were applied to a simulated pavement system consisting of an existing asphalt layer with an HMA overlay. The properties of undamaged asphalt shown in Table 4.5 were used for the HMA overlay, while the properties of damaged asphalt shown in Table 4.5 were used for the existing asphalt layer. The asphalt layers were underlain by base course and subgrade layers. The pavement system finite element model was two-dimensional symmetric.

Two models of the pavement system were created. The first model assumed that no cracks were present in the existing asphalt, while the second model assumed that the asphalt layer had preexisting cracks. Both models were subjected to a static displacement applied to the corner of the asphalt system. A static displacement was applied because only a static stress XFEM analysis procedure is available for the version of ABAQUS used in the present study (Dassault Systemes, 2009). The elements within 150 mm (6 in)

of the applied displacement location had a tie constraint to the applied displacement to simulate the displacement of a wheel load with a 6-inch radius. The tie constraint tied the motion of the nodes of the nearby elements to the node with the applied displacement. The tie constraint caused the applied displacement to be a maximum value at the point of application and to decrease toward the terminating edge of the tie constraint.

A schematic of the pavement geometry without preexisting cracks is shown in Figure 4.16(a) and consisted of an 80 mm (3 in) HMA overlay above an 80 mm (3 in) thick existing asphalt layer. A 150 mm (6 in) base course layer, and 1.5 m (5 ft) of subgrade soil were located below the asphalt layers. All layers were 4.300 m (14 ft) wide. The asphalt model with pre-existing cracks is shown in Figure 4.16(b). The existing asphalt layer contained two linear cracks that were 40 mm (1.5 in) deep and spaced approximately 100 mm (4 in) apart and were located 387.5 mm (15.25 in) and 487.5 mm (19.2 in) from the left edge of the pavement system. The initial crack locations were selected such that crack geometries did not interfere, as ABAQUS XFEM analysis currently cannot analyze intersecting cracks (Dassault Systemes, 2009). The cracks were located beyond the wheel load lateral tie constraint and extended halfway into the existing asphalt layer.

The ABAQUS pavement system models with associated finite element mesh and boundary conditions for the pavement system without preexisting cracks and the pavement system with preexisting cracks are shown in Figure 4.17 and Figure 4.18, respectively. An enlarged view of the finite element model mesh is also presented in

these figures. Pinned boundary conditions at the subgrade layer base were used which constrained displacement in the x and y directions. A symmetric boundary condition was applied to the left side of the pavement system and constrained displacement in the x direction and rotation in the y direction. The pavement systems had a general mesh size of 25 mm with a 5 mm mesh spacing within the asphalt near the top-left corner of the system. The HMA overlay and existing asphalt layers were composed of free quadratic elements. The base course material was composed free quadratic-dominated elements, while the subgrade material was composed of structured quadratic-dominated elements.

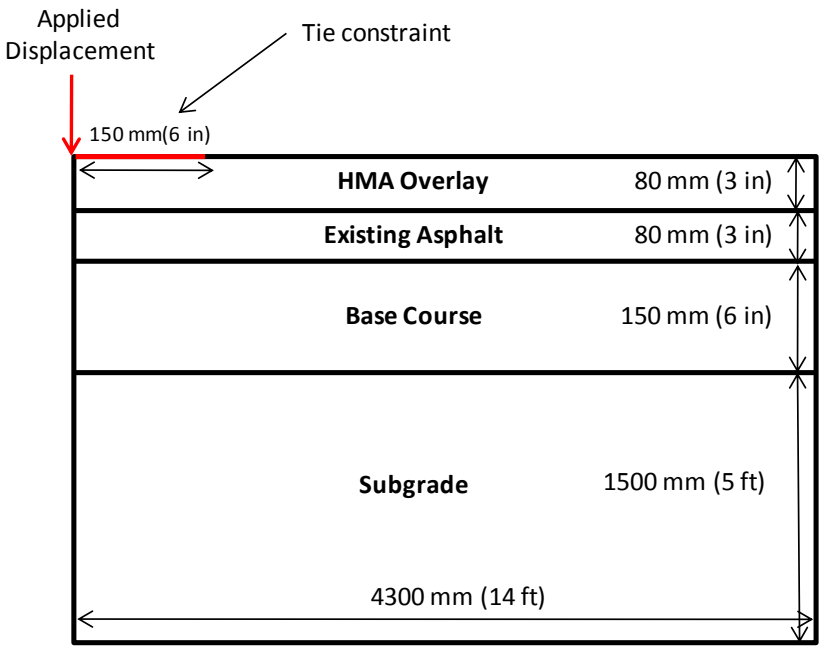

(a) Without Preexisting Cracks

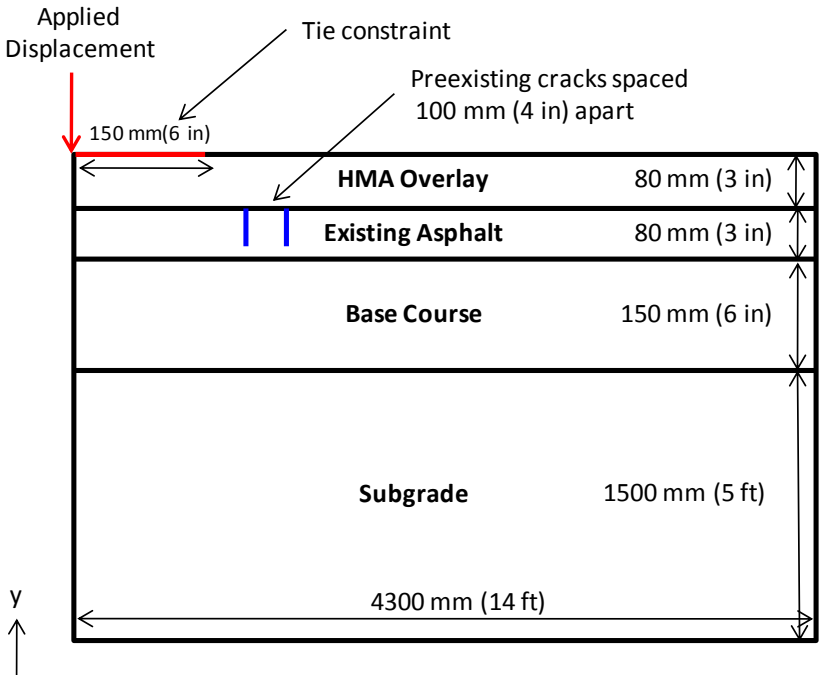

(b) With Preexisting Cracks

Figure 4.16. Geometry of Pavement System used in Finite Element Analysis

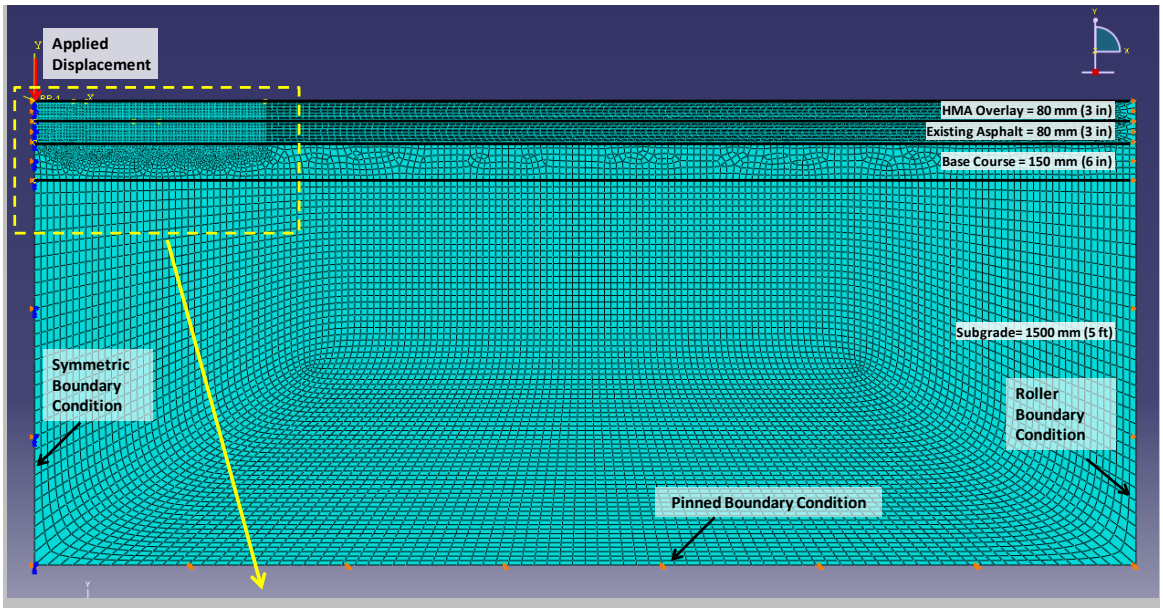

(a) Mesh and Boundary Conditions

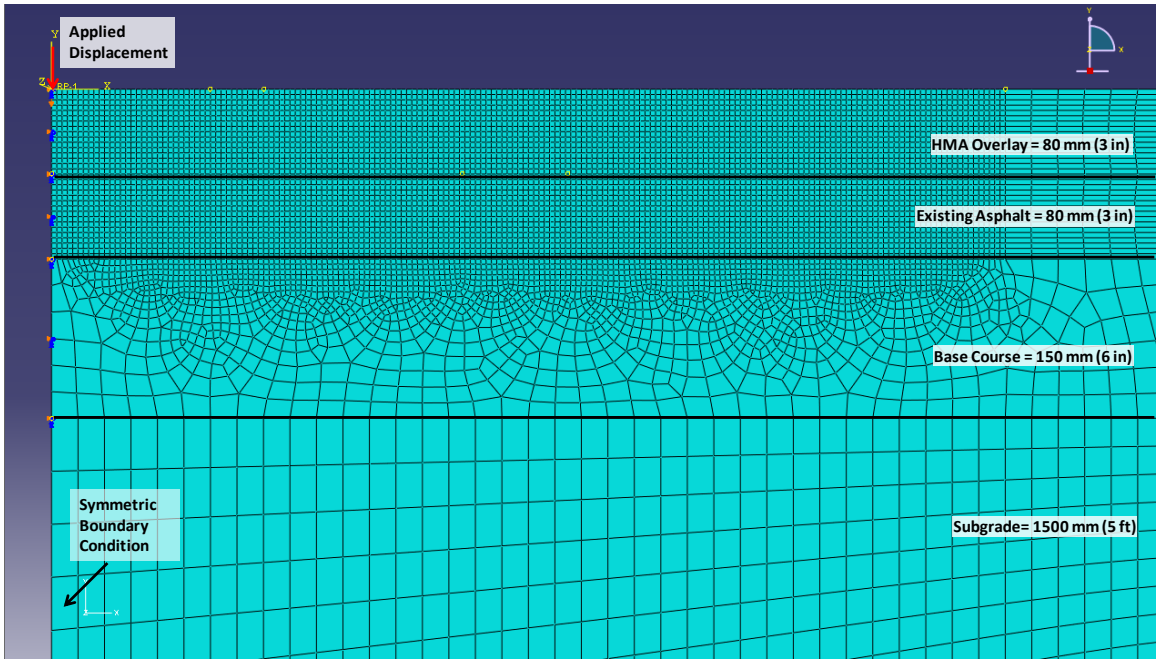

(b) Enlarged Mesh View

Figure 4.17. ABAQUS Pavement System Model without Preexisting Cracks

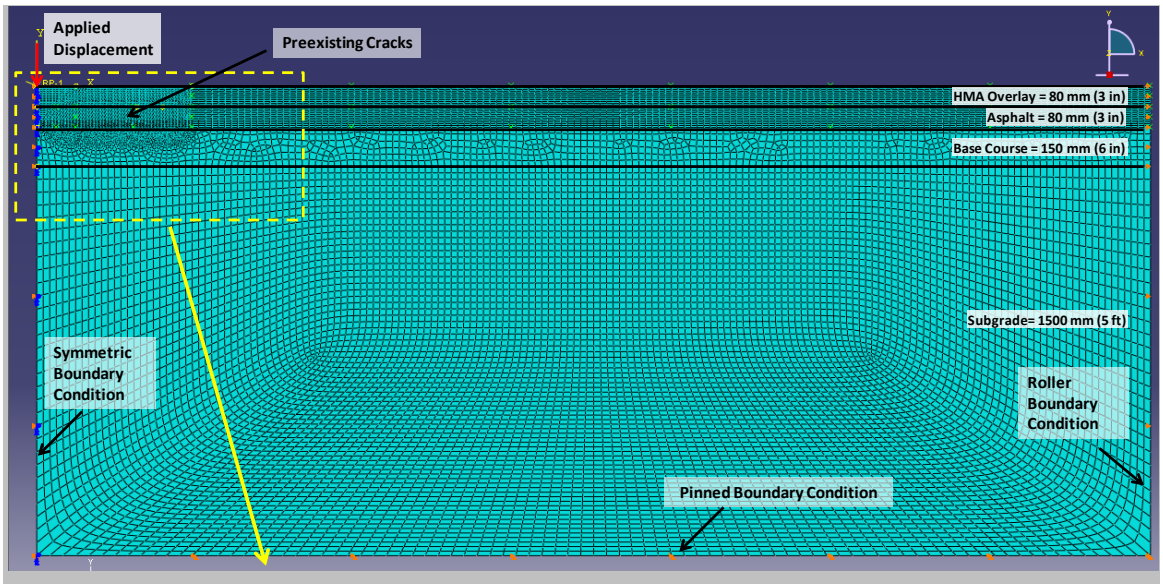

(a) Mesh and Boundary Conditions

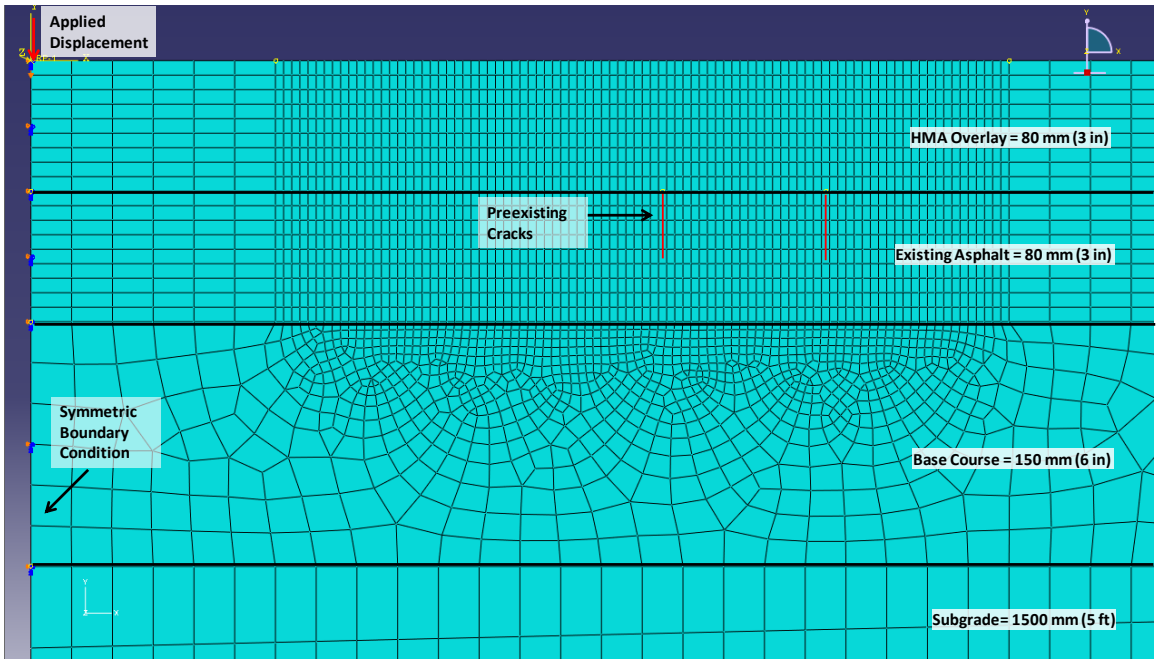

(b) Enlarged Mesh View

Figure 4.18. ABAQUS Pavement System Model with Preexisting Cracks

4.7.1 Element Type and Time Step

Four-noded, bilinear, plane strain quadrilateral elements were used to model the HMA overlay, existing asphalt, base course, and subgrade layers. The mesh nodes were spaced 25 mm apart in the majority of the model, while the mesh near the applied displacement was refined to a 5 mm node spacing. A single time step (time period equal to one) was used in the analysis with the time step increments (fractions of a step) shown in Table 4.6. These time step increments were chosen based on recommendations provided in an ABAQUS damage-based fracture and failure workshop for modeling systems with large displacements (Dassault Systemes, 2009b). The step time incrementation was also adjusted to account for non-linear effects ("Nlgeom" setting on). An automatic stabilization damping factor of 1×10^{-5} was also used. The time incrementation was adjusted for a discontinuous analysis ($I_0 = 8$, $I_R = 10$). A maximum number of iterations (I_A) value of 15 was used in this analysis.

Table 4.6. Time Step Increments Used in ABAQUS Finite Element Model

Maximum Number of Increments	500
Initial Increment Size	1×10^{-4}
Minimum Increment Size	1×10^{-50}
Maximum Increment Size	0.1

4.8 RESULTS AND DISCUSSION

4.8.1 Pavement System Modeling Results

The damage initiation and evolution material properties determined through IDT laboratory testing and ABAQUS finite element modeling of asphalt cylinders in indirect and direct tension were applied to a pavement system consisting of an HMA overlay, an existing asphalt layer, a layer of base course material, and a layer of subgrade. An enlarged view of the pavement system corner where displacement was applied is shown in Figure 4.19 through Figure 4.22 to emphasize the damage that developed.

Finite element models were generated for two scenarios. The first model had no preexisting cracks in the asphalt material and cracking was allowed to generate anywhere within the asphalt layers. The second model had two pre-existing cracks located in the surface of the existing asphalt layer below the HMA overlay. When finite element modeling was performed on the pavement system without preexisting cracks, a stress concentration immediately developed at the bottom of the existing asphalt layer directly beneath the wheel load and on the surface of the HMA layer near the edge of the wheel load. For the pavement system with preexisting cracks in the existing asphalt layer, cracking was confined to an area a short distance away from the applied displacement and axis symmetric boundary conditions in order to reduce damage associated with the boundary conditions.

Contour plots from the ABAQUS modeling on the pavement systems are presented in Figure 4.19 through Figure 4.22. The contours in the following figures have been

exaggerated for ease of visibility. Displacement contour plots for pavement systems both with and without initial cracks in the existing asphalt layer are shown in Figure 4.19. The pavement system without initial cracks in the existing asphalt layer experienced a downward displacement of 0.14 mm (0.006 in) before cracking intersected the edge of the pavement system and the model terminated. The pavement system with initial cracks in the existing asphalt experienced a downward displacement of 12 mm (0.5 inches) before the cracks in the existing asphalt material reached the surface of the new HMA layer and the model terminated.

The maximum principal stress for the pavement system without preexisting cracks is shown in Figure 4.20. Stress concentrations for the pavement system with no preexisting cracks first occurred at the bottom of the existing asphalt layer directly beneath the wheel load followed by a stress concentration at the surface of the new HMA layer. Stress concentrations for the pavement system with preexisting cracks developed immediately above and below the cracks and moved toward the surface of the new HMA as cracking initiated. A contour plot showing only tensile maximum principal stress was created for the pavement system with preexisting cracks. This plot is shown as Figure 4.21. Only contours for tensile maximum principal stress values are shown in this figure to emphasize the tensile stresses that develop in the model. Compressive maximum principal stress values in Figure 4.21 are shown in gray. This figure shows the development of high tensile maximum principal stresses near the bottom of the existing asphalt layer and how the tensile stresses change as cracking initiates and evolves in the pavement system.

A contour plot of the damage variable D_{XFEM} within the pavement system is shown in Figure 4.22. The contours associated with a non-zero value indicate that the maximum principal stress values for damage initiation as shown in Table 4.5 have been reached and damage initiated. The red contours associated with a D_{XFEM} value of one indicate that damage within the element completely evolved. For the pavement system without preexisting cracks in the existing asphalt layer, the damage variable did not reach a value of one and the cracks did not evolve. This was due to the fact that cracking had initiated in elements at the model boundary, which caused the model to terminate. For the pavement system with preexisting cracks in the existing asphalt layer, cracking first traveled down from the preexisting cracks until the bottom of the existing asphalt layer was cracked. Cracking then propagated up toward the surface of the new HMA layer.

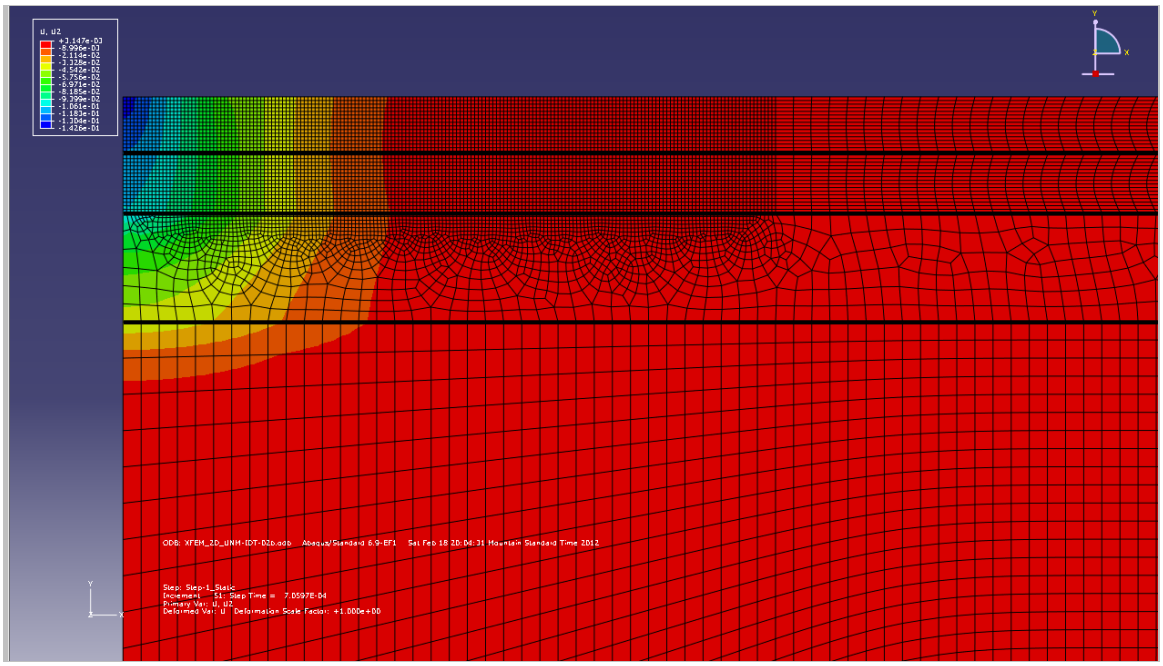

(a) No Preexisting Cracks

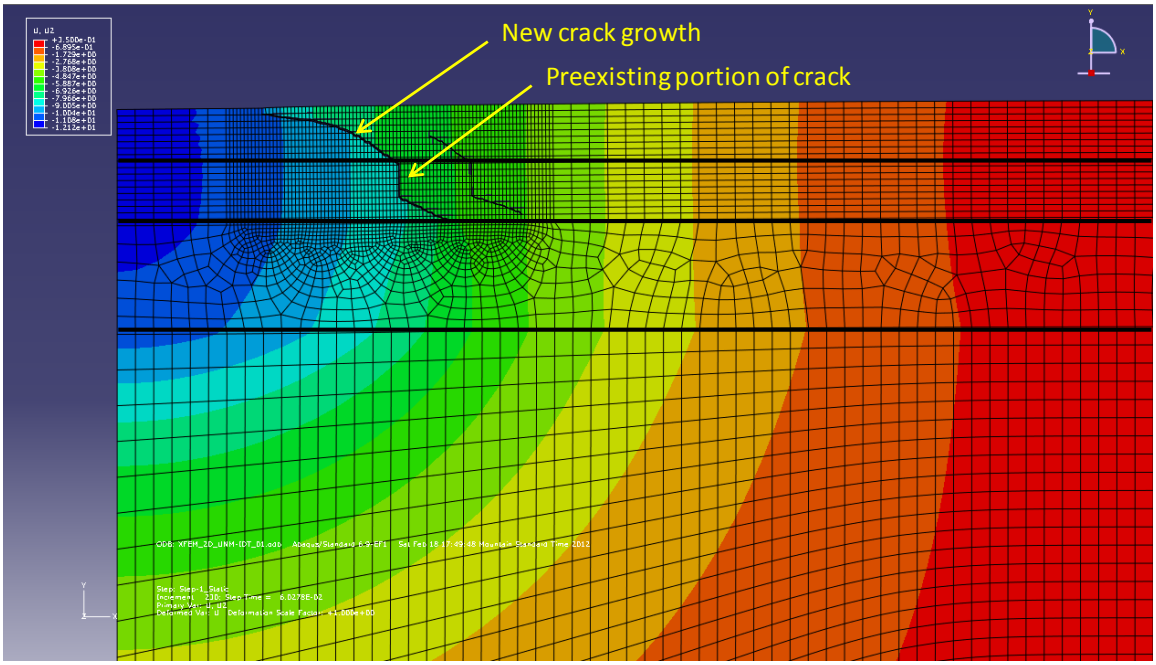

(b) With Preexisting Cracks

Figure 4.19. Contour Plot of Displacement of the Pavement System

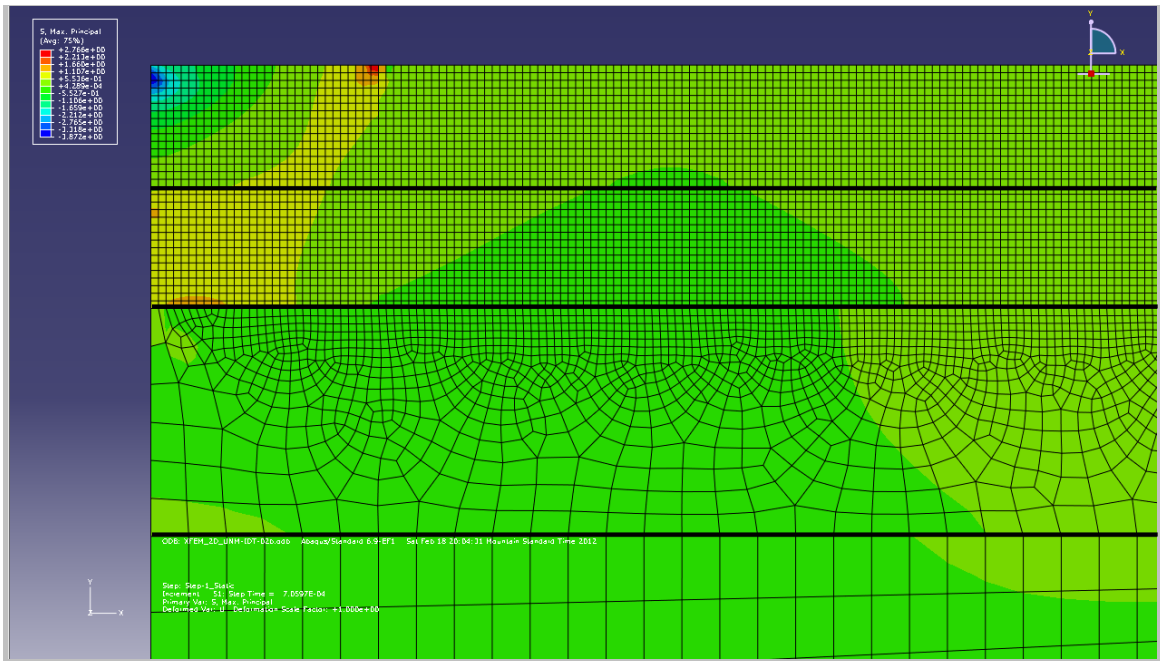

(a) No Preexisting Cracks

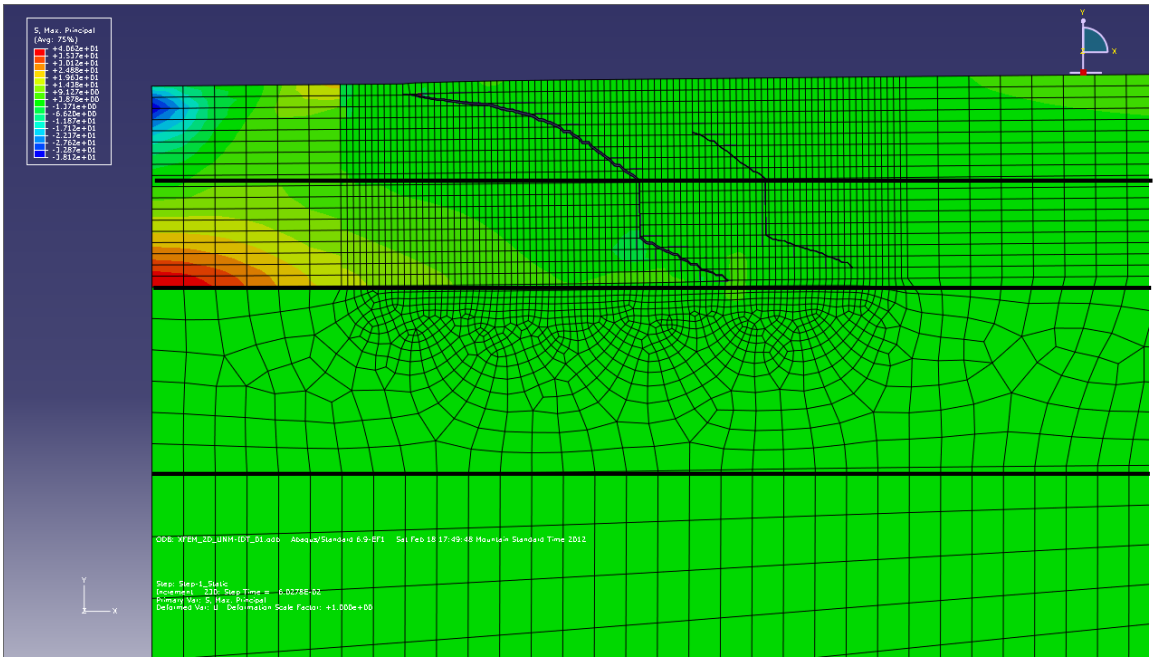

(b) With Preexisting Cracks

Figure 4.20. Contour Plot of Maximum Principal Stress in the Pavement System

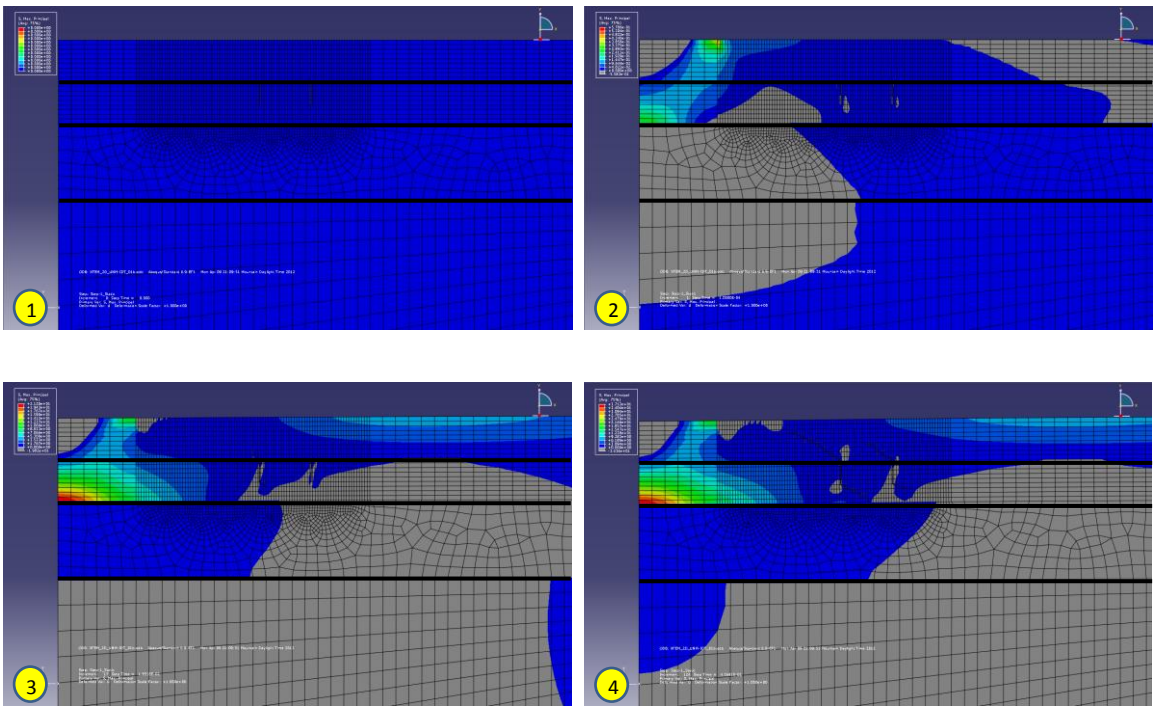

Figure 4.21. Contour Plot of Maximum Principal Stress in the Pavement System with Preexisting Cracks (Two Contour Intervals)

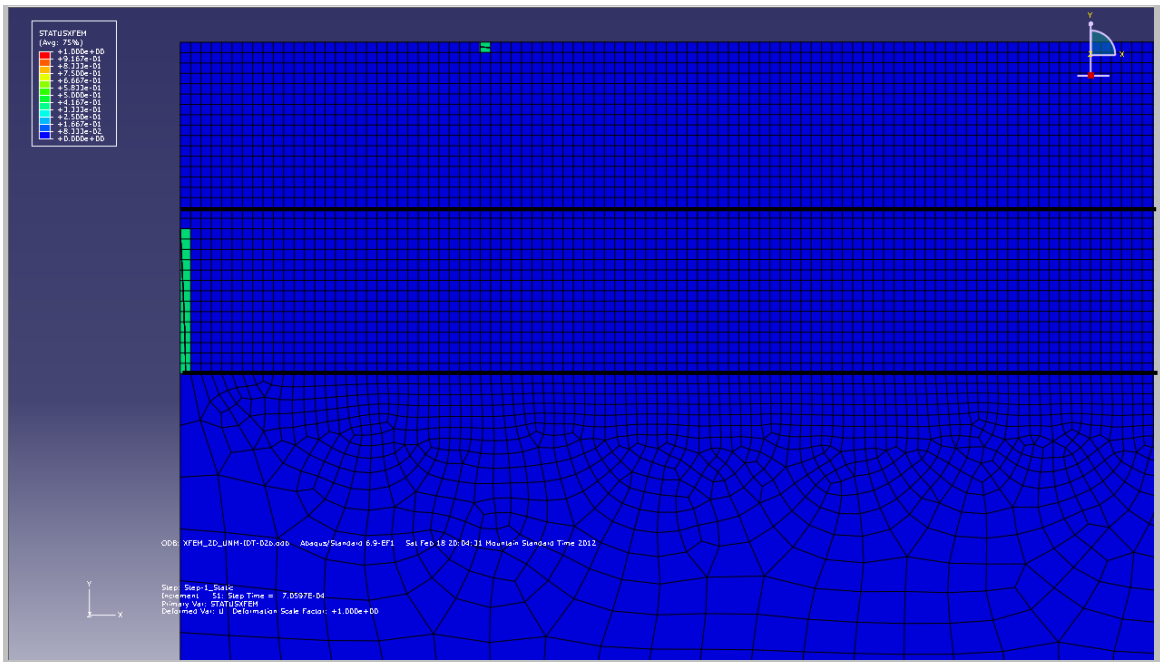

(a) No Preexisting Cracks

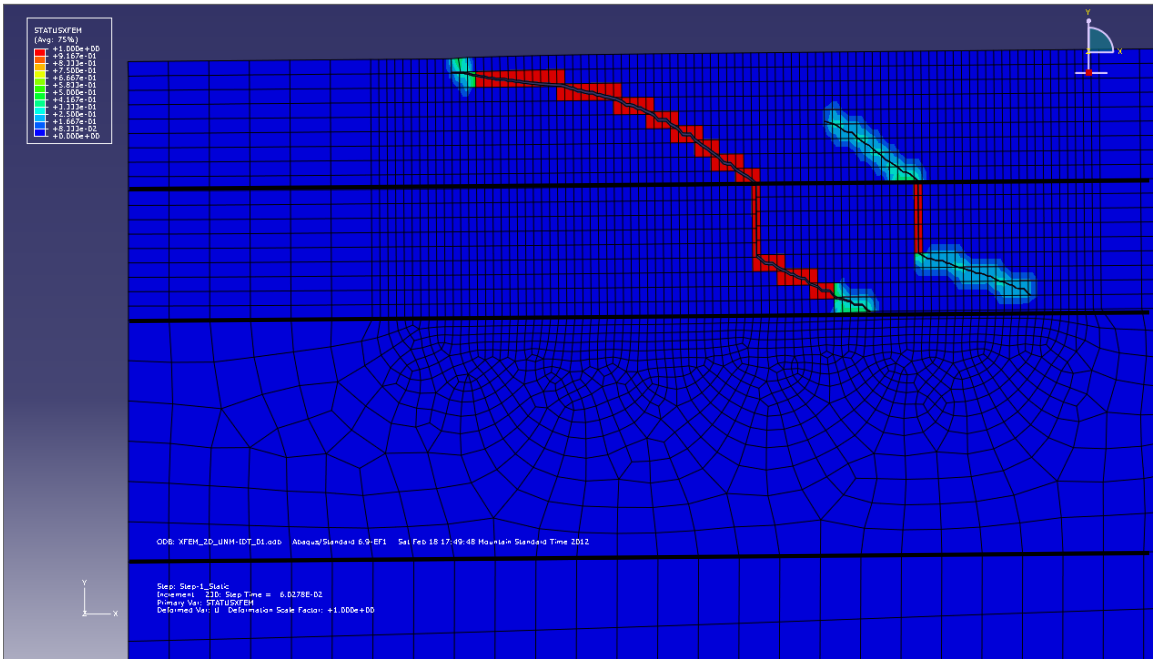

(b) With Preexisting Cracks

Figure 4.22. Damage Variable D_{XFEM} Contour Plots of the Pavement System

4.8.2 Correlations for Pavement System without Preexisting Cracks

Relationships between maximum principal stress versus displacement, maximum principal stress versus the damage variable D_{XFEM}, and maximum principal stress versus principal strain were developed for the pavement system with no preexisting cracks in the existing asphalt layer at the data locations show in Figure 4.23. These relationships are shown in Figure 4.24 through Figure 4.25. Damage initiated within the asphalt layers after the maximum principal stress values shown in Table 4.5 were reached.

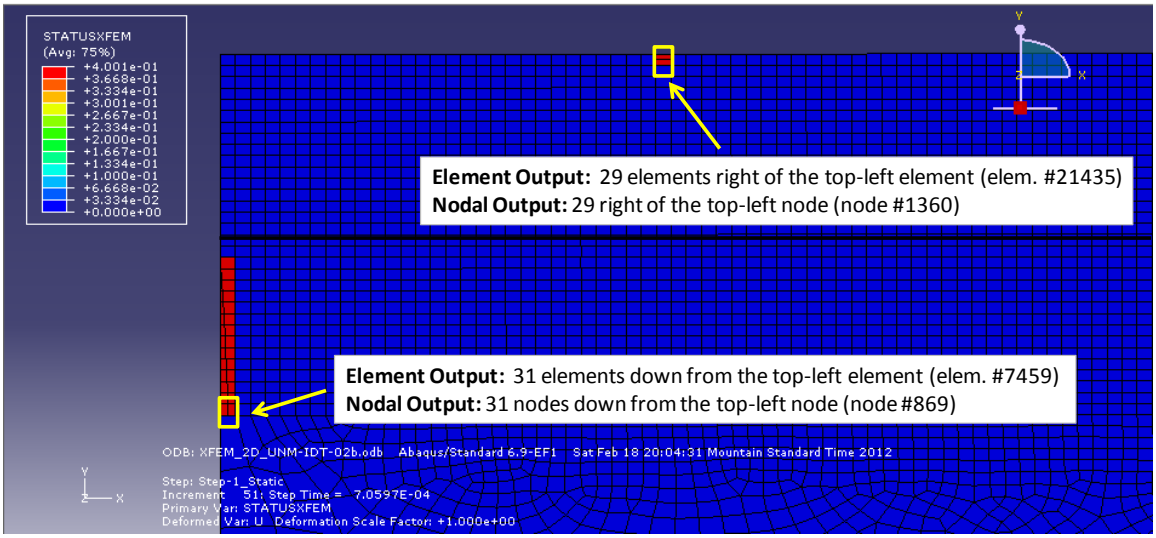

Figure 4.23. Data Locations for Results Presented in Figure 4.24 through Figure 4.26

Figure 4.25 shows the relationship between the maximum principal stress and the damage variable D_{XFEM}. The D_{XFEM} value remained at zero until damage was initiated, after which the D_{XFEM} value was greater than zero. D_{XFEM} was equal to one when damage has completely evolved. As shown in Figure 4.25, damage within both the HMA layer and the existing asphalt layer initiated but did not evolve (D_{XFEM} did not reach a value of

one). This was due to cracks intersecting the model boundaries, which caused difficulties in model convergence.

Figure 4.26 shows the relationship between maximum principal stress and associated strain for elements within the HMA layer and the existing asphalt layer. After the damage initiation strain was achieved, the stress should have decreases to a zero value, and the portions of the element on either side of the crack recover elastically. Because the model did not converge however, damage did not evolve and the strain within the pavement system did not return to zero. The model was still able to capture a realistic failure behavior for the asphalt without solution convergence as crack initiation occurred in realistic locations within the pavement as shown in Figure 4.22.

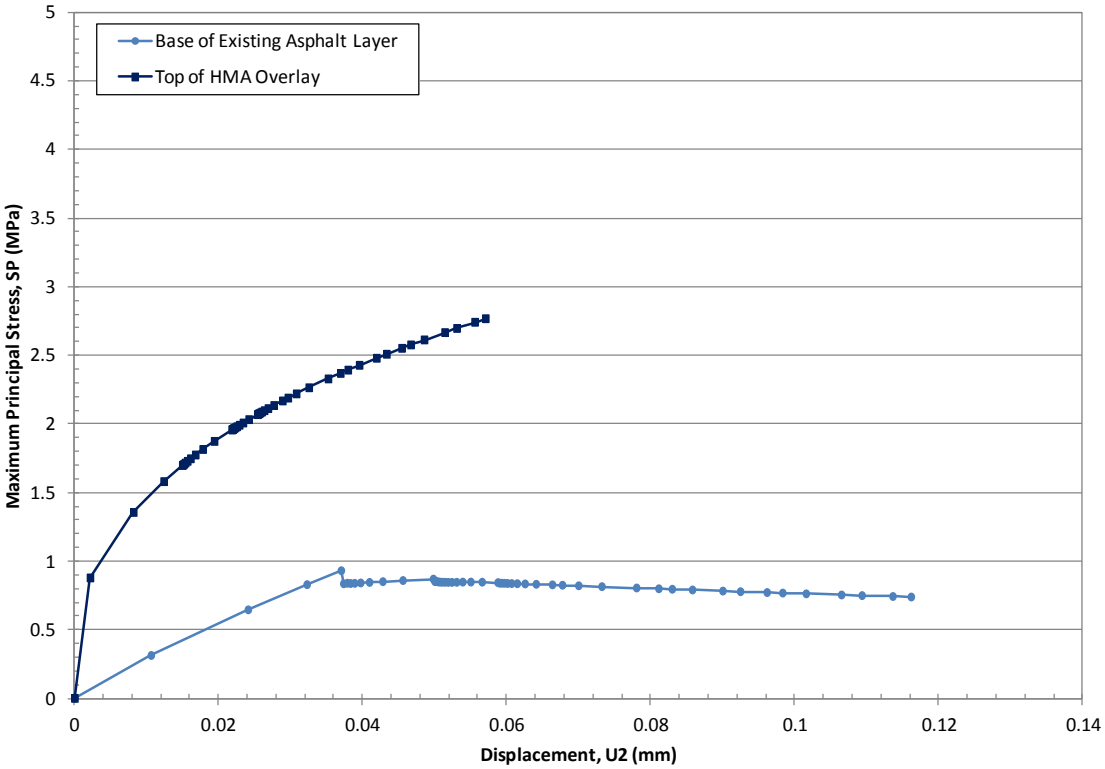

Figure 4.24. Maximum Principal Stress vs. Displacement for Pavement System with no Preexisting Cracks

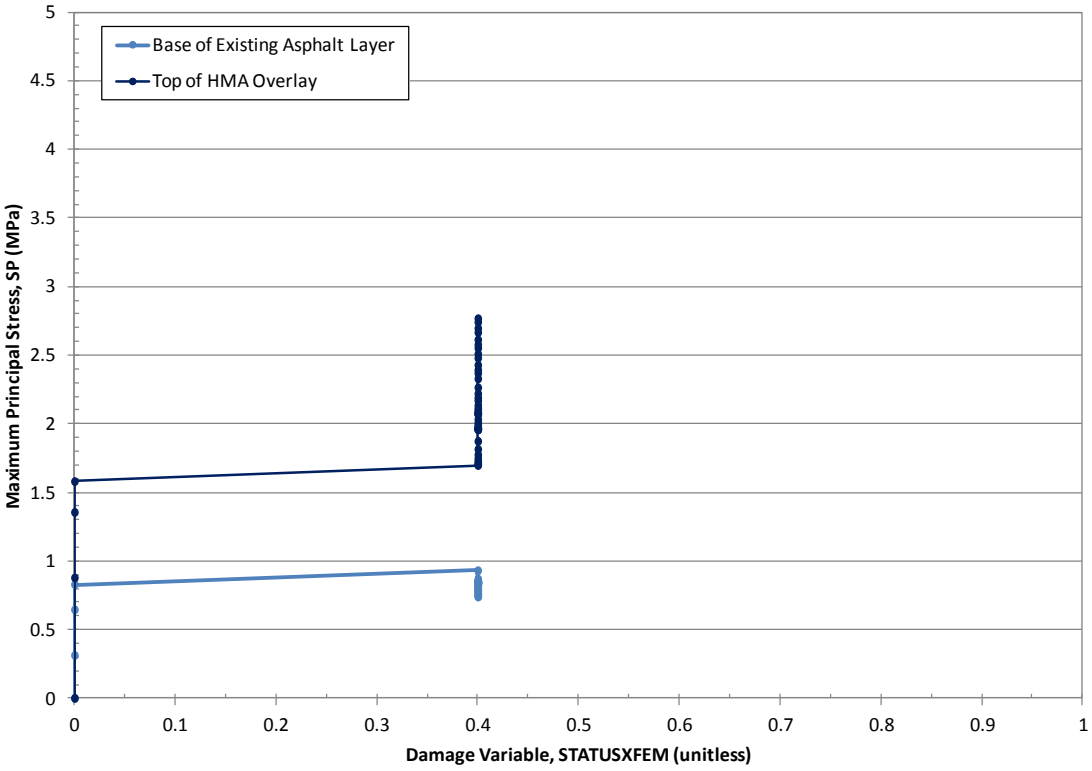

Figure 4.25. Maximum Principal Stress vs. Damage Variable D_{XFEM} for Pavement System with no Preexisting Cracks

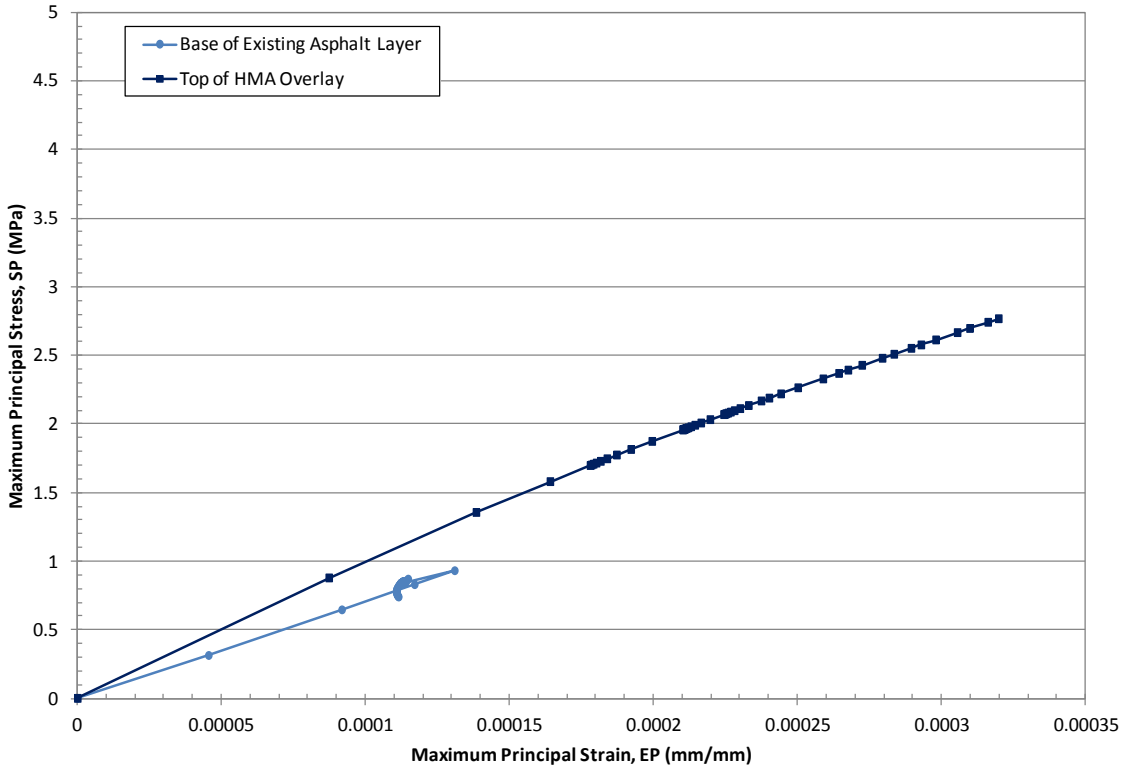

Figure 4.26. Maximum Principal Stress vs. Strain for Pavement System with no Preexisting Cracks

4.8.3 Correlations for Pavement System with Preexisting Cracks

Relationships between maximum principal stress versus displacement, maximum principal stress versus the damage variable D_{XFEM}, and maximum principal stress versus strain were developed for the finite element analysis of the pavement system with preexisting cracks in the existing asphalt layer at the data locations show in Figure 4.27. These relationships are shown in Figure 4.28 through Figure 4.30. Relationships are shown for an element at the bottom of the existing asphalt layer, at the bottom of the HMA layer, and at the surface of the HMA layer.

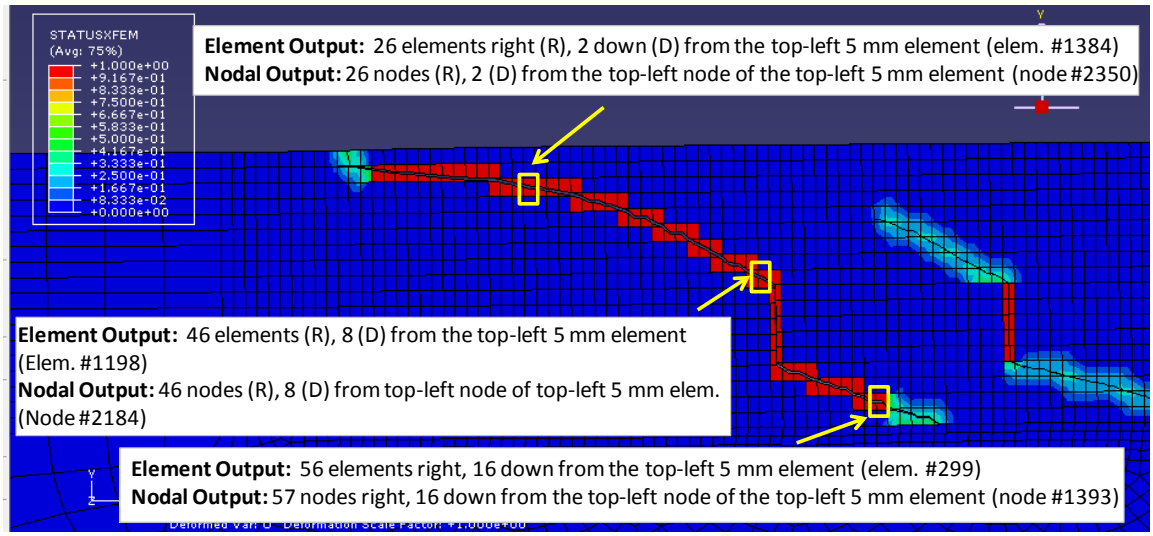

Figure 4.27. Data Locations for Results Presented in Figure 4.28 through Figure 4.30

Figure 4.28 shows the relationship between maximum principal stress and displacement for the pavement system. The base of the existing asphalt layer initially experienced a compression stress. After cracks propagated downward into the layer however, the base of the layer experienced tensile stress until cracking was complete. The HMA layer

experienced tensile stresses during the applied displacement which increased until the crack front reaches the layer; tensile stresses then decreased until a zero value was reached.

Figure 4.29 shows the relationship between the maximum principal stress and the damage variable D_{XFEM}. The value of D_{XFEM} remained at zero until damage was initiated, after which the value of D_{XFEM} was greater than zero. D_{XFEM} was equal to one when damage completely evolved. Even though complete damage evolution in the material was achieved as cracks developed, the elements at the top of the HMA layer and the bottom of the existing asphalt layer exhibited a non-zero stress value when D_{XFEM} was equal to one. This was caused by solution convergence difficulties because the crack had reached the edge of the model at the top of the HMA layer and the base course material at the bottom of the existing asphalt layer, which was prohibited from cracking. However, the model still captured a realistic cracking pattern within the asphalt as shown in Figure 4.22.

Figure 4.30 shows the relationship between maximum principal stress and associated strain for an element within pavement system. The stress decreased to nearly zero after the damage initiation strain was achieved. Although damage did occur in the asphalt materials, the shape of the stress-strain curves indicated difficulties with solution convergence due to crack intersection with the model boundaries.

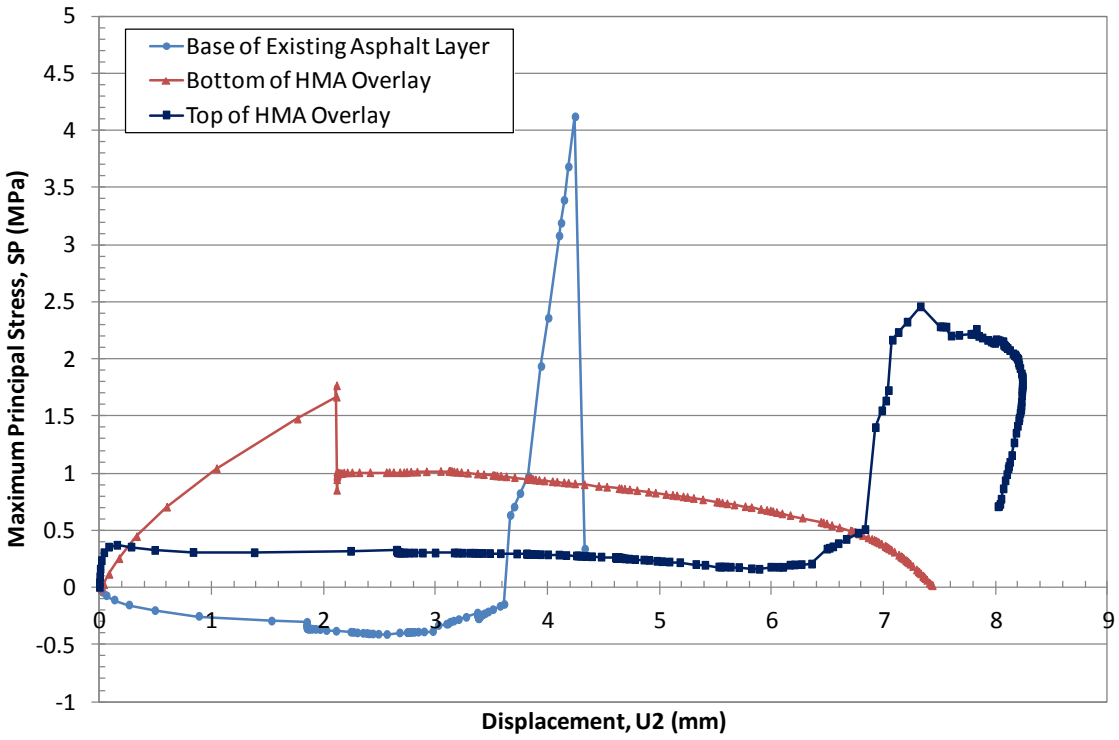

Figure 4.28. Maximum Principal Stress vs. Displacement for Pavement System with Preexisting Cracks

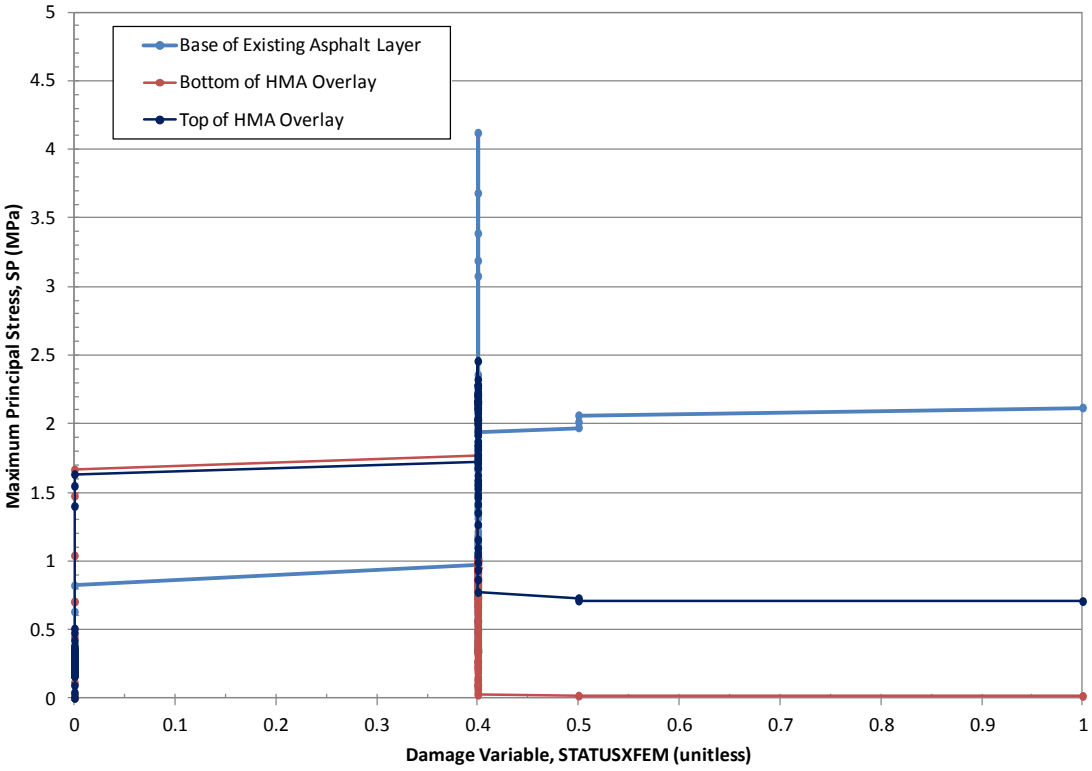

Figure 4.29. Maximum Principal Stress vs. Damage Variable D_{XFEM} for Pavement System with Preexisting Cracks

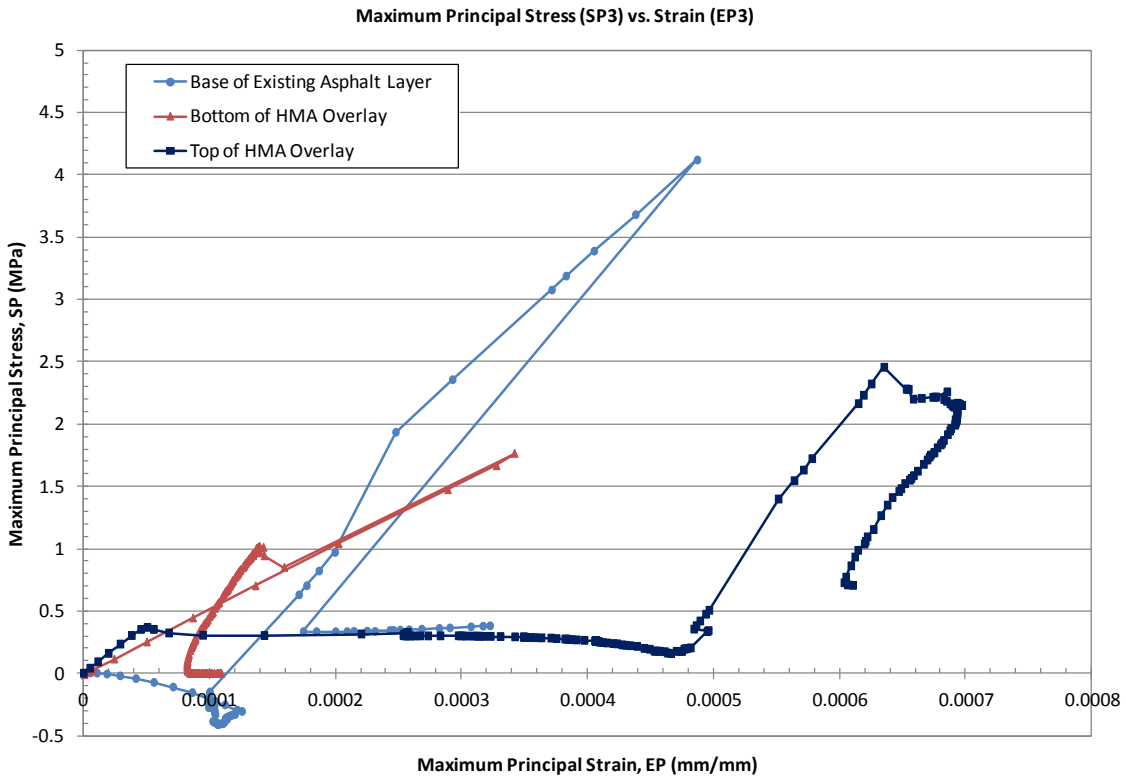

Figure 4.30. Maximum Principal Stress vs. Strain for Pavement System with Preexisting Cracks

4.8.4 Crack Pattern Dependency on Mesh Size

The dependency of the crack pattern on the mesh size was investigated for the pavement system configuration with preexisting cracks shown in Figure 4.16 (b). The mesh around the preexisting cracks was refined from a 5 mm mesh size to a 3 mm and 1.5 mm mesh size. The cracking pattern as well as the Damage Variable D_{XFEM} for each of these mesh sizes is shown in Figure 4.31.

Figure 4.31 shows a similar cracking pattern exists for all three mesh sizes with similar crack angles ranging from approximately 32 to 38 degrees from horizontal. The preexisting crack furthest from the wheel displacement advanced further with a 3 mm mesh size compared to the model with a 5 mm mesh size and migrated down toward the crack closest to the applied displacement. Crack damage initiated and evolved for the 5 mm and 3 mm models and is indicated by the red-colored contours in Figure 4.31. However, damage initiated but did not evolve for the model with a 1.5 mm mesh size before the model terminated. This comparison shows that the cracking pattern in slightly dependent on mesh size and that damage evolution is dependent on mesh size for the XFEM method.

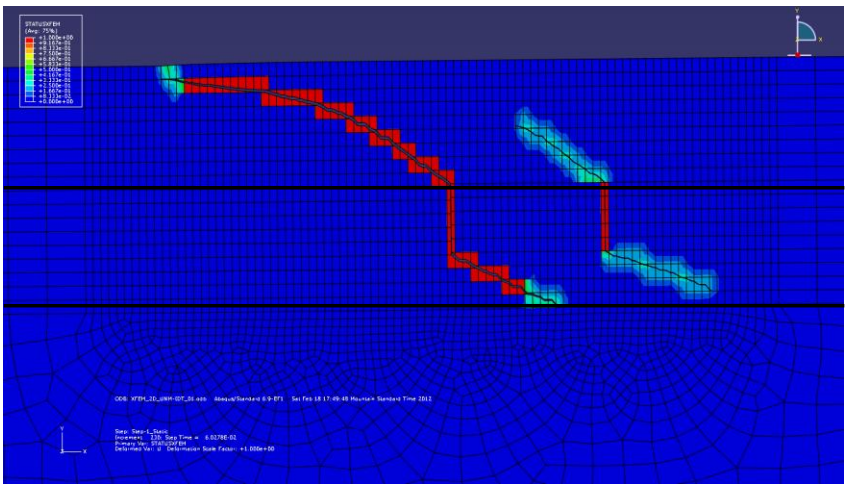

(a) 5 mm Mesh Size

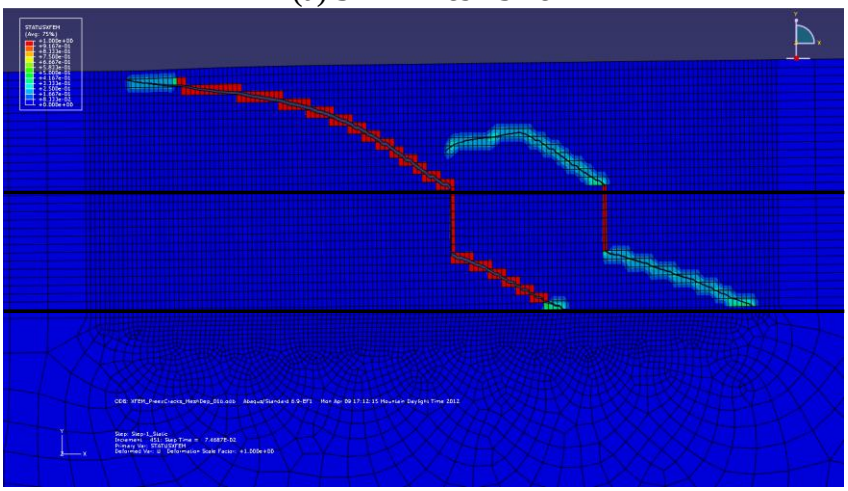

(b) 3 mm Mesh Size

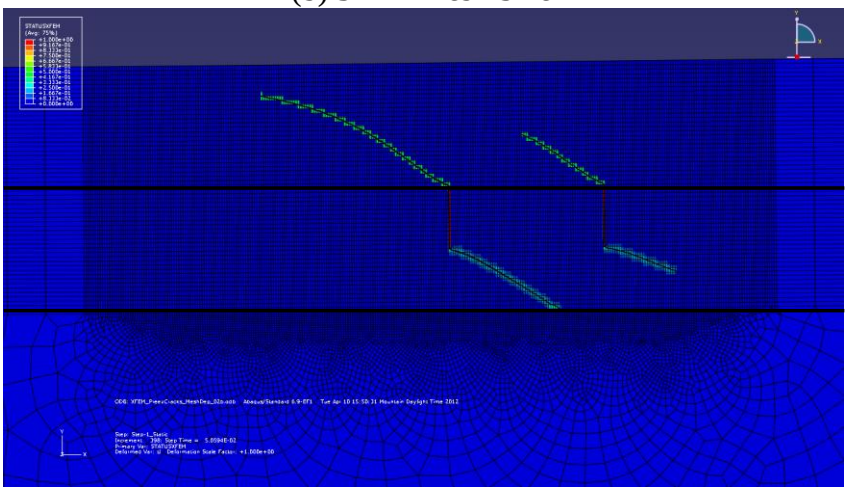

(c) 1.5 mm Mesh Size

Figure 4.31. Crack Pattern and Damage Variable D_{XFEM} Contour Plots for Pavement System with Preexisting Cracks with various Mesh Sizes

Plots of maximum principal stress versus displacement were created for elements located at the bottom of the existing asphalt layer, at the bottom of the HMA layer, and at the top of the HMA layer for the 5 mm, 3 mm, and 1.5 mm mesh sizes investigated. These plots are shown in Figure 4.33. The maximum principal stress versus displacement plots have similar shapes for elements at the bottom of the existing asphalt layer, at the bottom of the HMA layer, and at the top of the HMA layer for all three mesh sizes. However, there are differences in the maximum principal stress values achieved within each system before cracking occurred, as well as differences in displacement before cracking was completed in the elements.

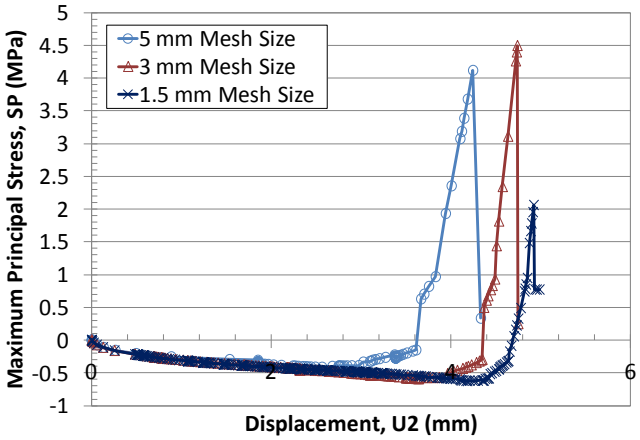

(a) Bottom of Existing Asphalt Layer

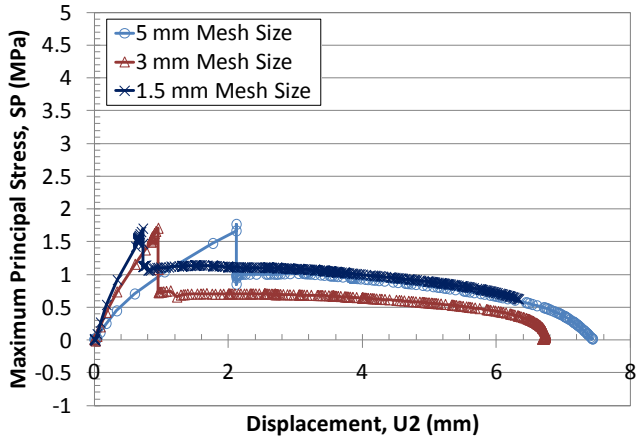

(b) Bottom of HMA Layer

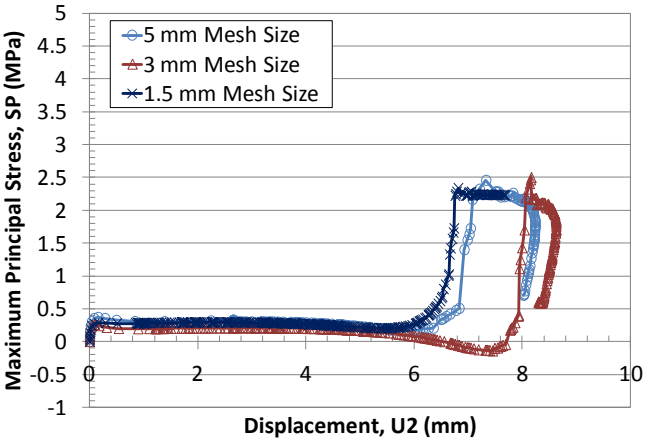

(c) Top of HMA Layer

Figure 4.32. Maximum Principal Stress vs. Displacement for Pavement System with Preexisting Cracks for various Mesh Sizes

4.8.5 Crack Pattern Dependency on Preexisting Crack Location

The dependency of the crack pattern on the location of the preexisting cracks was investigated for the pavement system configuration with preexisting cracks shown in Figure 4.16 (b). Two scenarios were investigated. The two cracks were located under the applied wheel displacement in the first scenario and were 37.5 mm (1.5 in) and 137.5 mm (5.4 in) from the left edge of the model. The cracks were then moved further away from the wheel displacement for the second scenario and were 737.5 mm (29.0 in) and 837.5 mm (33.0 in) from the left edge of the model. The depth, length, and spacing of the two preexisting cracks described in Section 4.7 were kept constant for the analysis. The pavement mesh size on both models was adjusted to ensure that the areas containing cracks had a 5 mm mesh size. The cracking patterns from these two scenarios were then compared to the cracking pattern described in 4.7 where the preexisting cracks were located 387.5 mm (15.25 in) and 487.5 mm (19.2 in). The cracking pattern comparison is shown in Figure 4.33.

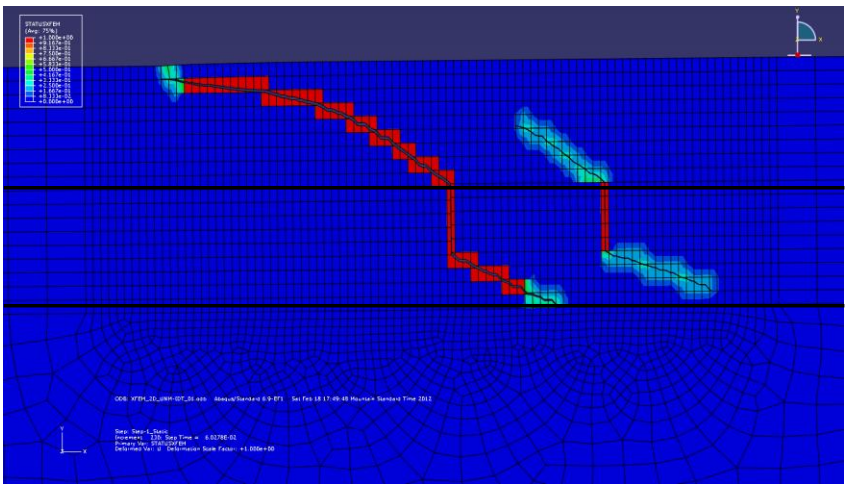

(a) 387.5 mm and 487.5 mm from Left Edge

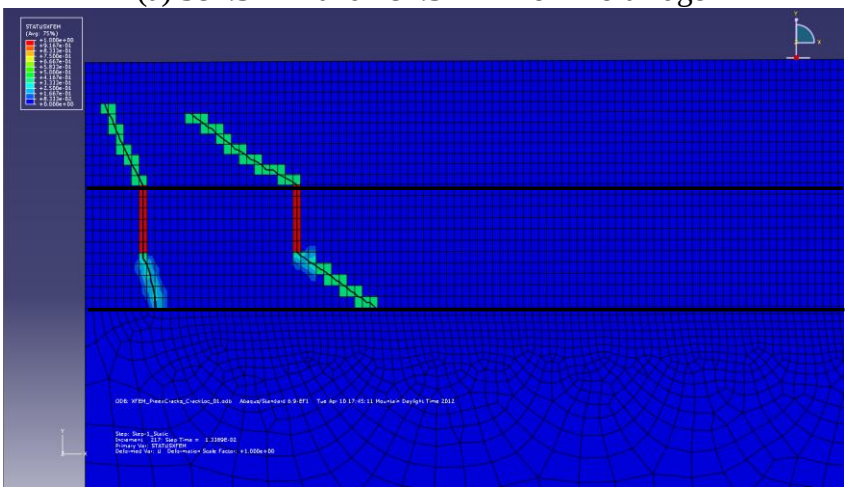

(b) 37.5 mm and 137.5 mm from Left Edge

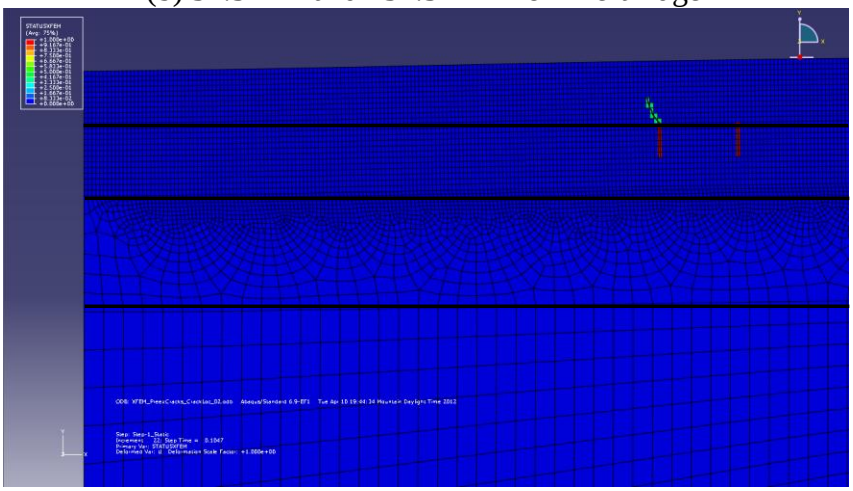

(c) 737.5 mm and 837.5 mm from Left Edge

Figure 4.33. Crack Pattern and Damage Variable D_{XFEM} Contour Plots for Pavement System with Preexisting Cracks with Cracks Located at Various Distances from the Applied Wheel Displacement

The angle of cracking (approximately 33 degrees from horizontal) for the crack farthest from the applied displacement was similar between the model with the preexisting cracks located under the applied displacement shown in Figure 4.33(b) and the model with the preexisting cracks 387.5 mm (15.25 in) from the left edge shown in Figure 4.33(a). The crack closest to the applied displacement in the model shown in Figure 4.33(b) grew at a steeper angle (approximately 65 degrees from horizontal) than the crack shown in Figure 4.33(a). Damage initiated in this crack but did not evolve. When the preexisting cracks were located a far distance (737.5 mm, 29.0 in) from the left model edge, cracking initiated but did not evolve, and the crack closest to the applied displacement migrated only a short distance into the HMA layer. This comparison shows preexisting cracks will migrate at a steeper angle toward the top of the HMA when the preexisting cracks are located below the applied displacement as shown in Figure 4.33(b). Preexisting cracks will migrate toward the top of the HMA layer at a shallower angle when the cracks are located a moderate distance from the wheel load as shown in Figure 4.33(a). Crack growth will be minimal when the preexisting cracks are located farther from the wheel load as shown in Figure 4.33(c).

The difference in maximum principal stress values was examined for all three preexisting crack location scenarios. This comparison is shown in the maximum principal stress contour plots created at the end of the finite element model time step shown in Figure 4.34. Only contours for tensile maximum principal stress values are shown in Figure 4.34 to emphasize the tensile stresses that develop in each model. Compressive maximum principal stress values in Figure 4.34 are shown in gray. Both tensile and

compressive stresses developed in the model with the preexisting cracks 387.5 mm (15.25 in) from the left edge shown in Figure 4.34(a). The maximum principal stress damage initiation criteria was met and cracking initiated in this model. Cracking also evolved in this model since the maximum traction-separation crack-opening displacement was met, and damage with the cracks evolved. The maximum principal stress contour plots for the models with the preexisting cracks 387.5 mm (15.25 in) and (737.5 mm, 29.0 in) from the left edge are shown in Figure 4.34(b) and Figure 4.34(c), respectively. Although the tensile maximum principal stress values created in these models was enough to initiate damage, the crack-opening displacement required for crack growth was not achieved, and damage did not evolve in these systems.

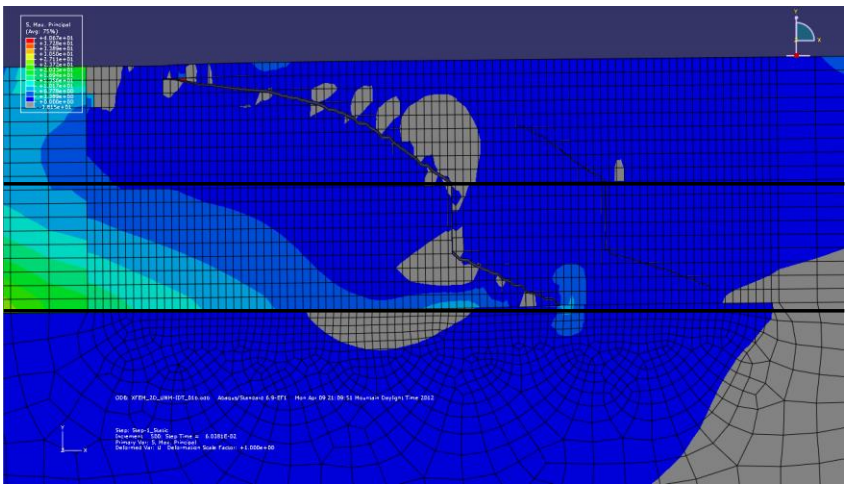

(a) 387.5 mm and 487.5 mm from Left Edge

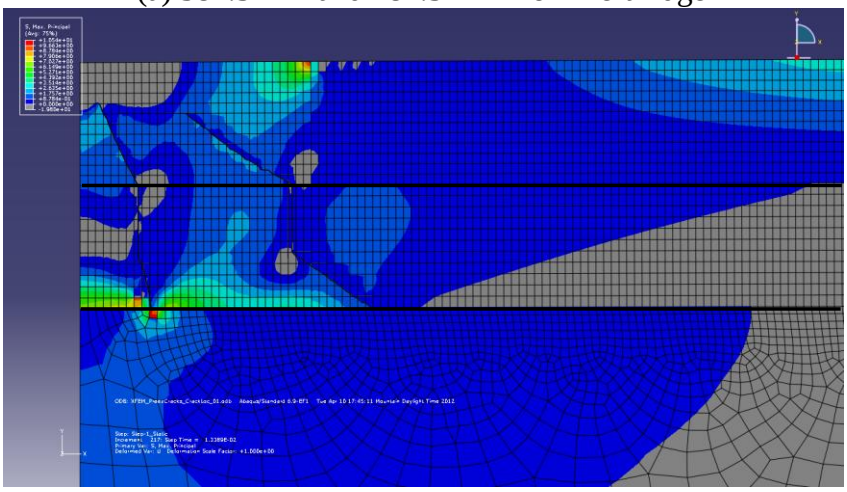

(b) 37.5 mm and 137.5 mm from Left Edge

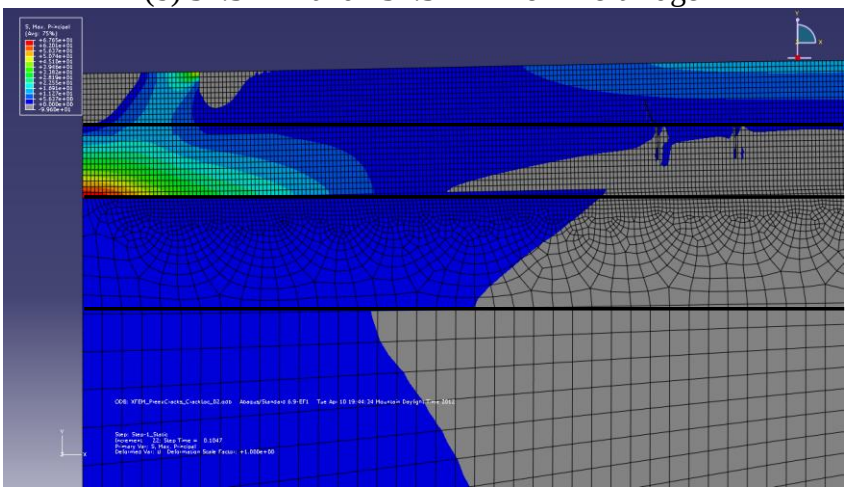

(c) 737.5 mm and 837.5 mm from Left Edge

Figure 4.34. Crack Pattern and Maximum Principal Stress Contour Plots for Pavement System with Preexisting Cracks with Cracks Located at Various Distances from the Applied Wheel Displacement

4.8.6 Tension in Base Course Material

Figure 4.21 shows that tensile maximum principal stress developed within the base course material for the pavement system with preexisting cracks. This is not a realistic scenario for base course material since base course is generally composed of cohesionless aggregate and sand and cannot sustain a tensile load. The effect of the base course layer thickness on tensile principal stress was investigated. Two scenarios were modeled. The first scenario had a base course thickness of 75 mm (3 in) which is half of the base course thickness described in Section 4.7 of 150 mm (6 in). The second scenario had a base course thickness of 300 mm (12 in) which is twice the base course thickness described in Section 4.7. In both cases, the subgrade material was either increased or reduced by the height difference taken from the base course material. Contour plots of the damage variable D_{XFEM} for all three scenarios are shown in Figure 4.35. Contour plots of the maximum principal stress for each scenario are shown in Figure 4.36. Only contours for tensile maximum principal stress values are shown in Figure 4.36 to emphasize the tensile stresses that develop in each model depending on the base course layer thickness. Compressive maximum principal stress values in Figure 4.36 are shown in gray.

Figure 4.36 shows that tensile maximum principal stresses are present in the base course layer for all three layer thicknesses modeled. This tensile stress extends further laterally as the base course layers get thicker. Tensile maximum principal stresses also develop in the subgrade material as the base course layer thickness increases.

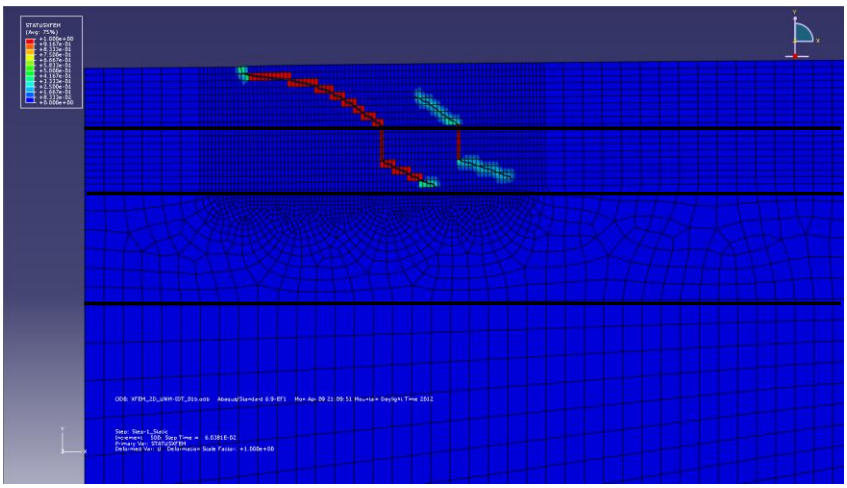

(a) Base Course Thickness of 150 mm (6 in)

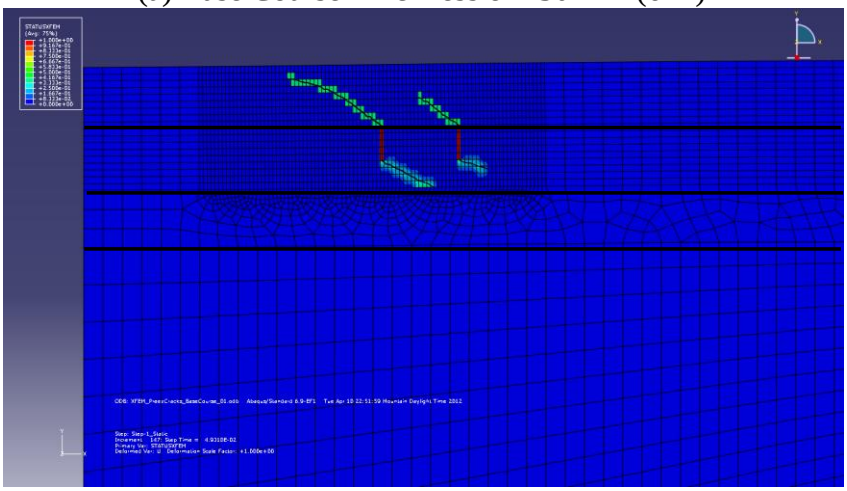

(b) Base Course Thickness of 75 mm (3 in)

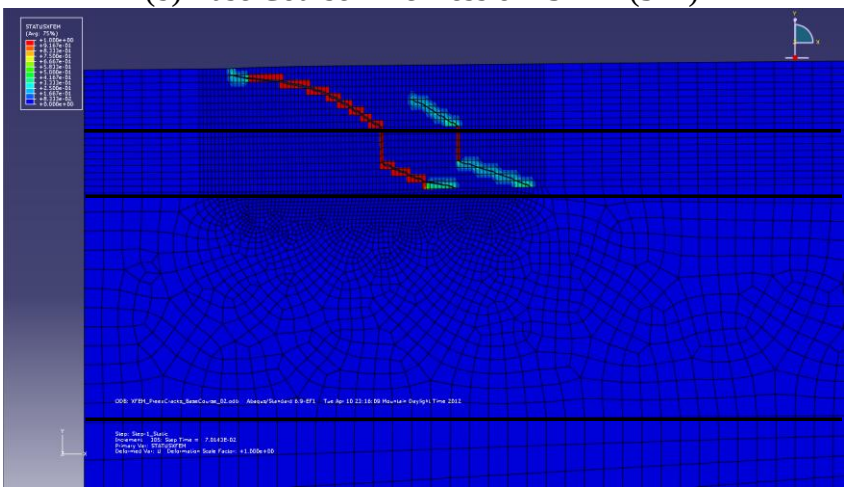

(c) Base Course Thickness of 300 mm (12 in)

Figure 4.35. Crack Pattern and Damage Variable D_{XFEM} Contour Plots for Pavement System with Preexisting Cracks and Various Base Course Layer Thicknesses

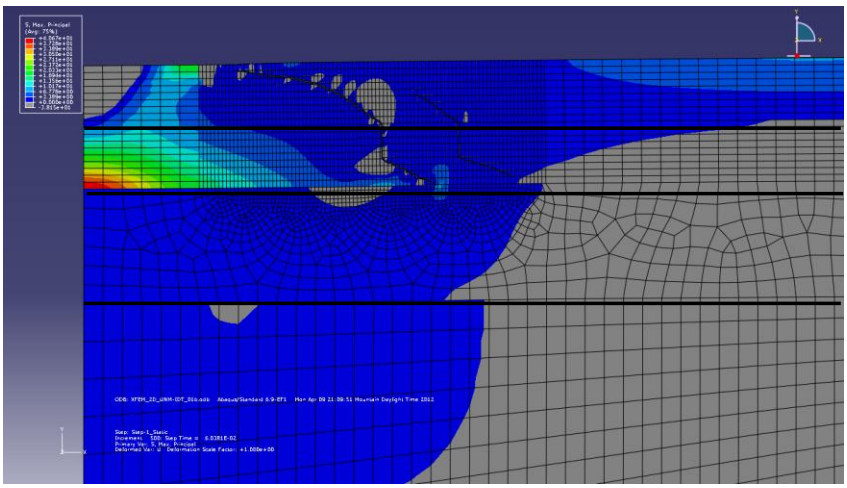

(a) Base Course Thickness of 150 mm (6 in)

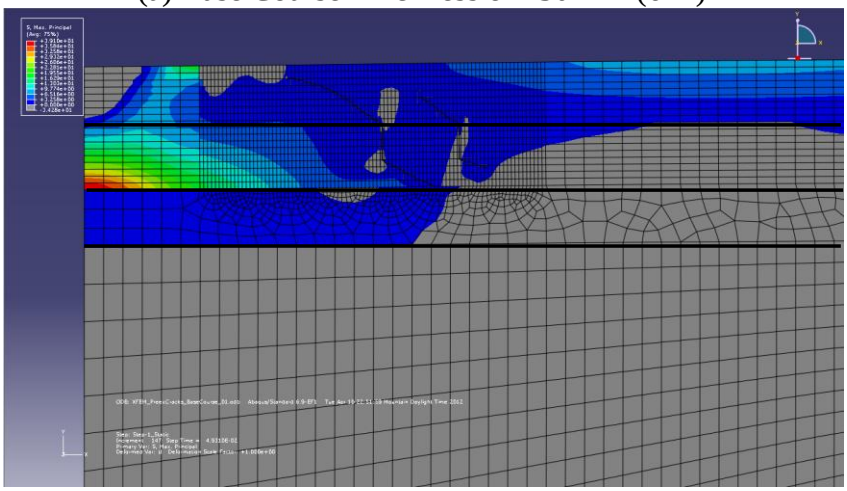

(b) Base Course Thickness of 75 mm (3 in)

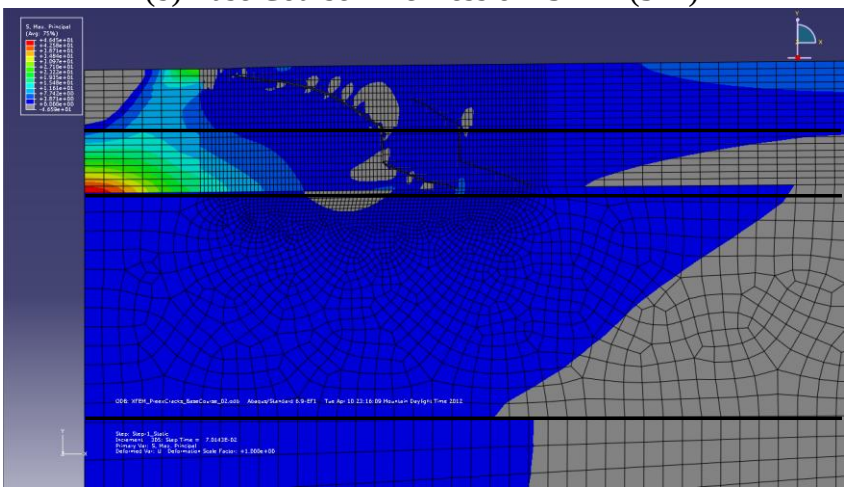

(c) Base Course Thickness of 300 mm (12 in)

Figure 4.36. Maximum Principal Stress Contour Plots for Pavement System with Preexisting Cracks and Various Base Course Layer Thicknesses

A plot of tensile maximum principal stress versus time step for an element located at the bottom left-hand corner of the base course layer for each of the scenarios is shown in Figure 4.37. Figure 4.37 shows that the tensile maximum principal stress decreases as the base course layer increases. All three base course thickness models converged to the same tensile maximum principal stress however as time progressed regardless of the layer thickness. This shows that tensile maximum principal stress will be present in the base course material for the pavement system models used in this study regardless of the base course layer thickness. This means that the base course material modeled in this study would need to be represented by a material which could sustain a tensile maximum principal stress in the field, such as base course reinforced with geosynthetic material or a base course material stabilized with cement.

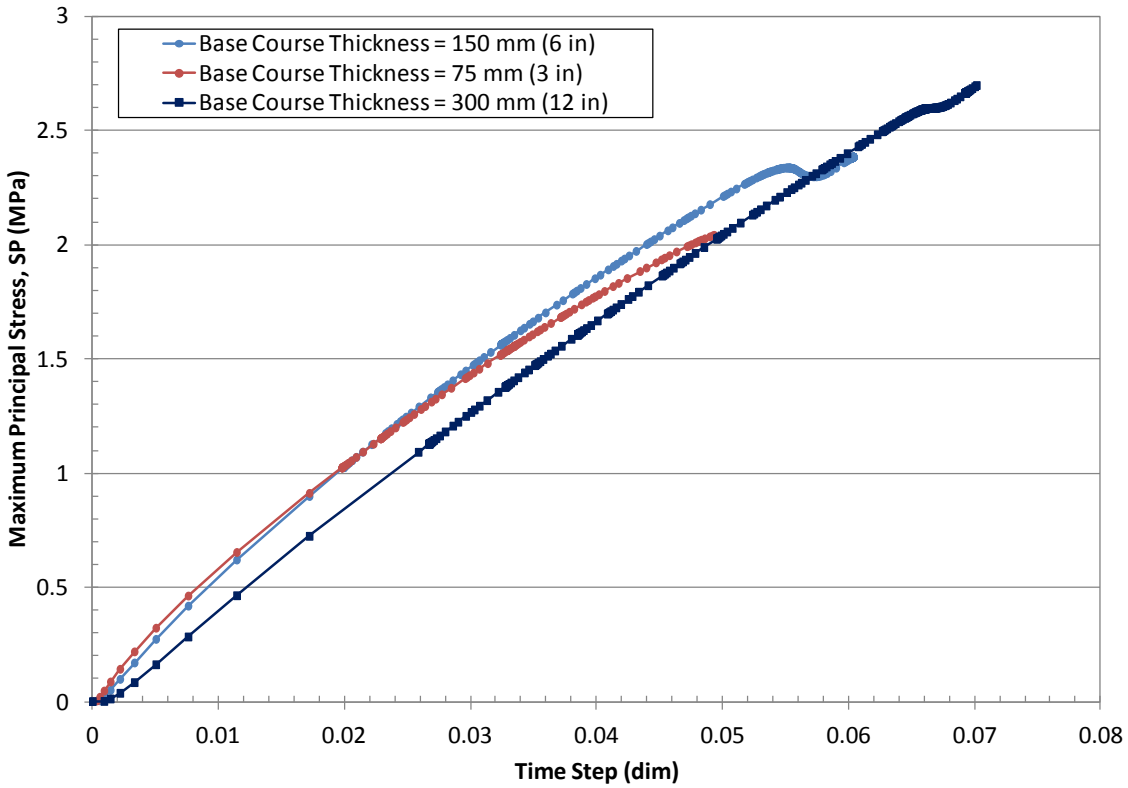

Figure 4.37. Maximum Principal Stress in Base Course Layer versus Time Step for Various Layer Thicknesses

4.9 CHAPTER CONCLUSIONS

Pavement systems with an HMA overlay on top of an existing asphalt layer were successfully modeled in ABAQUS as described in this chapter. Chapter conclusions include:

- The models developed in this study provided realistic cracking patterns for asphalt systems with preexisting cracks in the existing asphalt layer and without preexisting cracks in the existing asphalt layer.
- Peak traction stress at failure (t^0_{max}) values of 1.67 MPa and 0.93 MPa were determined for undamaged and damaged asphalt, respectively, through indirect tensile testing of asphalt cores.
- Cohesive fracture energy (G_C) values of 0.65 mJ/mm^2 and 0.45 mJ/mm^2 were determined for undamaged and damaged asphalt, respectively, through direct tensile test finite element modeling of asphalt cores.
- The cracking pattern within the asphalt system with preexisting cracks in the existing asphalt layer is not dependent on mesh size. However, the amount of tensile stress and displacement associated with cracking is slightly dependent on mesh size.
- Cracks migrated at a steeper angle toward the top of the HMA layer when the preexisting cracks were located below the applied wheel displacement. Preexisting cracks migrated toward the top of the HMA layer at a shallower angle when the cracks were located a moderate distance from the wheel displacement, and crack growth was minimal when the preexisting cracks were located farther from the wheel displacement.

5 CONCLUSIONS

5.1.1 Polymeric Composites

A double cantilever beam composed of IM7/977-2 composite material subjected to Mode I loading was successfully modeled in ABAQUS. The finite element model developed in this study predicted the interlaminar strength of the IM7/977-2 composite with reasonable accuracy as compared to laboratory data obtained from Johnson et. al. (2005). According to the results of the finite element model, damage within the interlaminar material of an 8-ply, IM7/977-2 composite panel at room temperature will occur at an applied Mode I "peeling" force of 35.5 N with an associated displacement of 21.9 mm. Damage evolution was then described according to a traction-separation law as shown in Figure 3.13. All input parameters required for damage modeling with ABAQUS were defined in this study.

Damage within the composite material was simulated in a way that did not require a pre-defined cracked zone. Damage was described according to a damage variable, *D* according to principles of the disturbed state concept. The stiffness and load-carrying capability of the interface material was systematically reduced according to a traction separation law until the interface material could not sustain a load and completely failed.

5.1.2 Asphalt Pavement Composites

Pavement systems with an HMA overlay on top of an existing asphalt layer were successfully modeled in ABAQUS. This included modeling a system without preexisting cracks in the existing asphalt layer as well as a system with preexisting cracks. The finite

element models developed in this study predicted the maximum principal stresses within various points of the pavement system under an applied static displacement. The developed models provided realistic cracking patterns for asphalt systems and specifically described bottom-up cracking for a pavement system with and HMA overlay on top of an existing asphalt layer with preexisting cracks. Peak traction stress at failure (t^0_{max}) values of 1.67 MPa and 0.93 MPa were determined for undamaged and damaged asphalt, respectively, through indirect tensile testing of asphalt cores. Cohesive fracture energy (G_C) values of 0.65 mJ/mm^2 and 0.45 mJ/mm^2 were determined for undamaged and damaged asphalt, respectively, through direct tensile test finite element modeling of asphalt cores.

Damage within the asphalt material was described using a traction-separation law where damage initiation and evolution was described according to a damage variable, *D* according to the disturbed state concept. A pre-cracked zone was not required to model cracking within the asphalt. Rather, cracks were allowed to develop based on the state of the maximum principal stress within the materials. Even though a pre-cracked zone was not required, the case where preexisting cracks were present within the asphalt was considered, as this is a common scenario in HMA overlays for a pavement system.

The damage initiation versus maximum principal stress and maximum principal stress versus displacement curves developed in this study can be used to predict the stress and displacement values at which damage will occur within new HMA and existing asphalt

materials. These curves can also be used to predict the stress or displacement at which damage has completely evolved and the material can no longer sustain stress.

This study is unique in that it allows for damage modeling where discrete cracks can form within the finite elements without the need for preexisting cracks utilizing the ABAQUS XFEM method. This method also allows cracks to develop independently of the mesh geometry. When cracks develop, the finite elements physically split according to the stress state within the element.

This ABAQUS XFEM method used in this study has several drawbacks. Most importantly, the XFEM method in the current version of ABAQUS can only be used for static loading conditions. Dynamic loading conditions are preferable when modeling asphalts that experience cyclic dynamic loads from wheel loads. The author recommends that further asphalt damage analysis studies be performed in future versions of the ABAQUS software where dynamic loading may be allowed for XFEM analysis.

The XFEM tool also cannot presently model crack interactions and elements cannot be intersected by more than one crack (Dassault Systemes, 2009). This does not allow modeling of multiple cracks developing in a single small location. The software is also very sensitive to boundary condition stress concentrations, and solutions will not converge when cracks intersect each other or the edge of the finite element model. The author recommends that the finite element analyses performed in this study be

reevaluated in future versions of the ABAQUS software when the problems encountered in this study have been addressed.

Even though convergence difficulties were encountered, the pavement system models developed in this study accurately predicted a realistic cracking pattern within the asphalt materials. Cracks propagated toward the bottom of the existing asphalt layer and toward the surface of the HMA overlay in the finite element model that had cracks within the existing asphalt. Cracking initiated below the wheel load in the existing asphalt layer and on the surface of the HMA overlay in the model that had no preexisting cracks in the existing asphalt layer. Both of these damage scenarios are realistic mechanisms for failure for pavement systems and have been documented in many pavement damage assessment studies (Huang, 2003). This study therefore provides input parameters validated through laboratory testing to accurately predict failure behavior is asphalt.

6 REFERENCES

ASTM D5528-01 (2007). "Standard Test Method for Mode I Interlaminar Fracture Toughness of Unidirectional Fiber-Reinforced Polymer Matrix Composites". American Society for Testing and Materials (ASTM).

ASTM D6931-07 (2007). "Standard Test Method for Indirect Tensile (IDT) Strength of Bituminous Mixtures". American Society for Testing and Materials (ASTM).

Aragão, F.T.S., Kim, Y.R., Lee, J., and Allen, D.H. (2011). "Micromechanical Model for Heterogeneous Asphalt Concrete Mixtures Subjected to Fracture Failure." *Journal of Materials in Civil Engineering*, Vol. 23, Iss. 1, pp. 30-38.

Belytschko, T., Black, T. (199). "Elastic Crack Growth in Finite Elements with Minimal Remeshing." *International Journal for Numerical Methods in Engineering*, Vol. 45, Iss. 5, pp. 601-620.

Chen, Y.K., Yu, J.M., and Zhang, X.N. (2010). "Micromechanical Analysis of Damage Evolution in Splitting Test of Asphalt Mixtures." *Journal of Central South University of Technology (English Edition)*, Vol. 17, Iss. 3, pp. 628-634.

Cycom® 977-2 Toughened Epoxy Resin Data Sheet, http://www.cytec.com/engineered-materials/products/Cycom977-2.htm (February 11, 2010).

Dassault Systemes (2007). ABAQUS Analysis Users Manual, v.6.7

Dassault Systemes (2009). ABAQUS Analysis User's Manual, v. 6.9

Dassault Systemes (2009b). "Damage Based Fracture and Failure with Abaqus", Workshop Material.

Desai, C.S. (2001). "Mechanics of Materials and Interfaces: The Disturbed State Concept." CRC Press LLC.

Desai, C.S. (2007). “Unified DSC Constitutive Model for Pavement Materials with Numerical Implementation.” *International Journal of Geomechanics*, Vol. 7, No. 2, pp. 83-101.

Diehl, T. (2008). “On Using a Penalty-Based Cohesive-Zone Finite Element Approach, Part I: Elastic Solution Benchmarks.” *International Journal of Adhesion and Adhesives*, Vol. 28, Iss. 4-5, pp. 237-255.

Feng, D.C., Lin, T., and Cao, P. (2011). "Study on Longitudinal Cracking During Settlement of Soil Based on Extended Finite Element Method". Engineering Mechanics (Gong Cheng Li Xue), Vol. 28, Iss. 5, pp. 149-154.

Garzon, J., Duarte, C., and Buttlar, W. (2010). "Analysis of Reflective Cracks in Airfield Pavements using a 3-D Generalized Finite Element Method". Road Materials and Pavement Design, Vol. 11, Iss. 2, pp. 459-477.

Giner, E., Sukumar, N., Tarancon, J.E., Fuenmayor, F.J. (2009). "An ABAQUS Implementation of the Extended Finite Element Method". Engineering Fracture Mechanics, Vol. 76, Iss. 3, pp. 347-368.

Hexcel® HexTow® IM7 Carbon Fiber Product Data Sheet, accessed on 2/11/2010. http://www.hexcel.com/NR/rdonlyres/BD219725-D46D-4884-A3B3-AFC86020EFDA/0/HexTow_IM7_5000.pdf

Huang, Y.H. (2003). “Pavement Analysis and Design.” Second Edition, Prentice Hall, Upper Saddle River, NJ.

Hyer, M.W. (2008). "Stress Analysis of Fiber-Reinforced Composite Materials." Second Edition, DEStech Publishers Inc., Lancaster, PA.

Johnson, W.S., Pavlick, M.M., and Oliver, M.S. (2005). “Determination of Interlaminar Toughness of IM7/977-2 Composites at Temperature Extremes and Different Thicknesses.” Final Report, NASA Grant Number NAG-1-02003.

Melenk, J. and Babuska, I. (1996). "The Partition of Unity Finite Element Method: Basic Theory and Applications". Computer Methods in Applied Mechanics and Engineering, Vol. 39, pp. 289-314.

Moes, N., Dolbow, J., Belytschko, T. (1999). "A Finite Element Method for Crack Growth without Remeshing". International Journal for Numerical Methods in Engineering, Vol. 46, Iss. 1, pp. 131-150.

Parry D.J. and Al-Hazmi, F.S. (2003). “Stress-Strain Behavior of IM7/977-2 and IM7/APC2 Carbon Fibre Composites at Low and High Strain Rates”. Journal de Physique, Vol. 110, pp. 57-62.

Sane, S.M, Desai, C.S., Jenson, J.W., et. al., 2008. "Disturbed State Constitutive Modeling of Two Pleistocene Tills". Quaternary Science Reviews, Vol. 27, pp. 267-283.

Shi, J., Chopp, D., Lua, J., Sukumar, N., and Belytschko, T. (2010). "ABAQUS Implementation of Extended Finite Element Method using a Level Set Representation for Three-Dimensional Fatigue Crack Growth and Life Predictions". Engineering Fracture Mechanics, Vol. 77, Iss. 14, pp. 2840-2863.

Song, J.H., Areias, P.M., and Belytschko, T. (2006). "A Method for Dynamic Crack and Shear Band Propagation with Phantom Nodes". International Journal for Numerical Methods in Engineering, Vol. 67, Iss. 6, pp. 868-893.

Zaniewski, J.P. and Srinivasan, G. (2004). "Evaluation of Indirect Tensile Strength to Identify Asphalt Concrete Rutting Potential". Asphalt Technology Program, Department of Civil and Environmental Engineering, West Virginia Univ., W.Va.

Tarefder, R.A., Zaman, A.M., and Uddin, W. (2010). "Determining Hardness and Elastic Modulus of Asphalt by Nanoindentation". International Journal of Geomechanics, Vol.10, No. 3, pp. 106-116.

Zhao, Y. and Wang, J. (2002). "The Influence of Low Temperature on the Fatigue Damage Process of Cracked Asphalt Pavement". 15th ASCE Engineering Mechanics Conference, June 2-5, 2002, Columbia University, New York, NY.